Università degli Studi di Napoli "Federico II"

Dottorato di Ricerca in Ingegneria dei Materiali e delle Strutture

XX Ciclo

TIN OXIDE THIN FILMS IN OPTO-CHEMICAL SENSING: PREPARATION, SURFACE MORPHOLOGY, NEAR FIELD OPTICAL PROPERTIES AND TESTING.

Dott.ssa Antonietta Buosciolo

Ph.D. Dissertation

TUTOR

Dr. Michele Giordano

COORDINATOR

Prof. Domenico Acierno

December 2007

Alla mia Famiglia

L'intelletto non è una lampada
che brucia senza olio,
ma viene alimentato
dalla passione e dalla volontà.
(Seneca)

Table of Contents

Chapter 5

Morphological and near field optical properties

Chapter 6

Sensing performance testing

Acknowledgments

The present work has been carried out at the SNOMLAB of the Institute of Composite and Biomedical Materials (IMCB-CNR) of Naples, under the precious guide of Dr. Michele Giordano. I deeply thank him for intense discussions, stimulation, constant encouragements, enriching travels and opportunities.

I am also very grateful to Dr. Andrea Cusano, who guided me through this project and represented a tremendous source of inspiration for my work. The present work would have been impossible without a fruitful collaboration with his scientific group, which provided me with materials, ideas and experience. My sincere thanks goes particularly to Eng. Pierluigi Pilla.

During the period of my PhD, I was surrounded by an amazing group of people in Portici: the SMARTLAB-SNOMLAB team. The special atmosphere in this group helped me greatly to achieve my goals. I would like to express my gratitude to all of them. It was a pleasure to share with them most days of the last three years. I hope to keep having coffee breaks together!

I must thanks two special persons, Angela Longo and Raffaele Sista: their friendship was really important for me in these years, so there is a bit of them in this work.

Finally and above all, I will be eternally grateful to my boyfriend Paolo, my parents, my brother Carlo and his family: things change with time, but their presence is still fundamental in my life. Without them, I would never be arrived at this moment.

CHAPTER 1

Introduction

The development of the Information Society, as last step of the Electronics revolution, requires the development and improvement of devices (sensors) able to transform physical or chemical phenomena into electrical or optical signal for further treatment using transducer systems. Thus, our society requires chemical sensors for domestic, automotive and industrial applications due to the implication of gases in environmental control or dangerous emissions. There is a continuing need for the development of rugged and reliable chemical sensors capable of making measurements in harsh industrial environments as well as for public health and security [1, 2]. The use of chemical sensors covers a wide range of industries such as steelmaking, heat treating, metal casting, glass, ceramic, pulp and paper, automotive, aerospace, utility and power. Emissions monitoring sensors for these applications include those for CO, NO_x, O_2, CO_2, hydrocarbons (HCs) and volatile organic compounds (VOCs). The application of sensor and measurement technology has resulted in many benefits including improved energy efficiency in combustion and chemical processes, better quality and lower scrap or off-specification products, and reduced emissions. Chemical sensors are also being applied in domestic appliances and air quality monitoring. Lately, chemical sensors are attracting attention for applications such as early detection of smoke/fire as well as hazardous chemical agents to provide safety and security in public places and mass transportation systems. According to a recent market report, US demand alone for chemical sensors (gas sensors and biosensors) was projected to reach $2.7 billion by 2006 [3]. For commercial success, major advances in these sensors are required in terms of simple structure, lower cost, selectivity, durability and reliability.

Many types of chemical sensors have been developed in the last decades. To this aim, a common approach involves the integration of a sensitive part which, interacting with the surrounding environment, collects and concentrate molecules at or within the surface undergoing physical changes, and of an opportune transducer that converts into an interpretable and quantifiable term such modification of the sensing part. The heart of the chemical sensor is thus the sensitive element which is the interface between the transducer and external environment so that the nature, the selectivity and sensitivity of the sensor depends upon these interactive materials.

Our attention has been focused on tin dioxide (SnO_2) as sensitive material.

SnO_2 belongs to the important family of metal oxides (MOXs) that combines high electrical conductivity with optical transparency and thus constitutes an important component for optoelectronic applications [4]. A field in which MOXs play a dominant role is in solid state gas sensors. Although a huge number of MOXs exhibits a response towards oxidizing and reducing gases by a variation of their electrical properties, tin oxide was one of the first considered and is still the most frequently used material for these applications.

Structural, electrical, and optical properties of tin oxide have been investigated by many authors [5]. Tin oxide films have polycrystalline structure with particular crystalline size and surface morphology. In addition, after its deposition, the structure of tin oxide films is stable in a wide range of temperatures 25 °C - 500 °C [6]. A lot of different types of resistive tin-dioxide sensors were performed for detecting hydrogen, carbon monoxide, methane, ammonia, nitrogen oxides, and different organic solvents [7, 8]. The sensing mechanism of all these SnO_2-based sensors is founded on electrical conductance caused by gas adsorption on their surfaces. Since only the surface layer is affected by the reaction, the sensitivity increases for a decreasing thickness, thus motivating the development of thin film metal oxide sensors.

The main disadvantage of resistive SnO_2-based sensors is that they require a very high operating temperature (250-450 °C) to enhance redox reactions so as to achieve the optimum sensitivity. Adding catalytic dopants (Pt, Pd,

Au, and Ag) makes it possible to decrease the operating temperature but it cannot decrease down to the room temperature .

In summary, their principle of operation and the high operating temperature, lead in any case to high power consumptions and to the impossibility to be exploited in liquid environment.

On the contrary, the investigation of the optical properties of SnO_2 layers, with particular interest to chemical sensing, could enable to overcome the aforementioned drawbacks and to exploit the excellent sensing performances of such material for the chemical detection in liquid and gas environments at room temperature.

Some recent works [9, 10] demonstrated the possibility to use SnO_2 as sensitive layer for fibre optic chemical sensors. These last ones are able to work at room temperature and in liquid environment exploiting all the advantages of an optical transducing technique.

The main advantages are related to the use of optoelectronic sensing devices that are resistant to electromagnetic interference and possess dual functionalities due to their capability to serve as transducers and sensing data communication systems.

Taking this line, the present work has been aimed to integrate SnO_2 thin film with fibre optic technology and to optimize the deposition technique in order to develop a new class of opto-chemical sensors suitable to be used for ppm chemical detection in water and air environments at room temperature.

In particular, interest has been focused on issues like investigation of the surface morphology and of the near field optical properties in relation to the processing and post-processing conditions; correlation of the surface layer morphology and the emerging near field intensity distribution with the sensing performances.

This thesis has been thus organized according to the following structure:

1. The first chapter provides an overview of the state of the art on chemical sensors. The last section introduces some basic concepts on fibre optic chemical sensors.

2. The second chapter is divided into two main sections. The first one describes the main bulk and surface properties of tin oxide; while the second one concerns a description of the ESP (Electrostatic Spray Pyrolysis): this very simple and inexpensive deposition technique allows to change the process parameters (like the metal chloride concentration, the solution volume, and the substrate temperature), in order to tailor the structural properties of the film such as crystalline size, thickness, porosity and surface morphology.

3. The third chapter concerns the theory of opto-chemical sensors based on SnO_2 thin films. It provides the mathematical model to analyze data obtained from experimental measurements. The last section provides a detailed description of the sample preparation.

4. The forth chapter explains how surface morphology and near field optical behaviour can be correlated by means of a powerful scanning probe system able to perform simultaneously normal force AFM (Atomic Force Microscopy) imaging and collection mode SNOM (Scanning Near Field Optical Microscopy) imaging. In particular, it is highlighted how AFM and SNOM techniques are emerging as powerful analytical tools, capable of sub-wavelength spatial resolution, enabling insights in the meso-scale optical properties and structures which in most cases could not be possible with any other technique.

5. The fifth chapter is a detailed discussion on the characterization measurements carried out on the prepared SnO_2 films varying the tin chloride concentration, by mean of the scanning probe system. In particular, it deals with the observation of a new phenomenon that takes places when the surface layers is characterized by the presence of isolated structures whose spatial dimensions are comparable or smaller than the used radiation wavelength. Moreover it concerns the observation of the effects of the annealing on the films surface morphology and on the near field behaviour, by mean of the aforementioned complex experimental set-up that allows to investigate almost the same spatial region (with good approximation) before and after the thermal treatment. Finally, it deals with some preliminary results about the real possibility to locally modify the surface morphology of

an SnO_2 film by mean of UV irradiation performed through the AFM-SNOM system.

6. Finally, the sixth chapter deals with the special features of the realized and characterized opto-chemical sensors. Series of measurements highlight how SnO_2 coated sensors, exhibiting a strong modification of the collected optical near field, are capable to detect ppm concentration of chemical pollutants in water and air environments, at room temperature.

1.1 The state of the art on chemical sensors

Sensor technology is a rapidly growing field that has significant potential to improve the operation, reliability, serviceability and utility of many engineering system. Advances in materials science and engineering have paved the way for the development of new and more capable sensors. In the field of sensor technology, the field of chemical sensors is the major research area. In fact there is a continuing need for the development of rugged and reliable chemical sensors capable of making measurements in harsh industrial environments as well as for public health and security [11-17]. The use of chemical sensors covers a wide range of industries such as steelmaking, heat treating, metal casting, glass, ceramic, pulp and paper, automotive, aerospace, utility and power. Emissions monitoring sensors for these applications include those for CO, NO_x, O_2, CO_2, hydrocarbons (HCs) and volatile organic compounds (VOCs). The application of sensor and measurement technology has resulted in many benefits including improved energy efficiency in combustion and chemical processes, better quality and lower scrap or off-specification products, and reduced emissions. Chemical sensors are also being applied in domestic appliances and air quality monitoring. In particular, nowadays, the presence of VOCs has become a serious concern due to tightened environmental regulation on VOCs all over the world. Their speedy evaporation and toxic or carcinogenic nature can make high concentrations in air dangerous to human beings. The VOCs are also recognized as the main cause of sick house syndrome, which is a product of poor indoor air quality. This can cause or aggravate certain conditions, including allergies, asthma, cancer, and emphysema [18]. Hence it is straightforward the necessity of high performance chemical sensors for continuous and in-situ VOCs detection.

Lately, chemical sensors are attracting attention for applications such as early detection of smoke-fire as well as hazardous chemical agents to provide safety and security in public places and mass transportation systems.

According to a recent market report, US demand alone for chemical sensors (gas sensors and biosensors) is projected to reach $2.7 billion by 2006 [19].

For commercial success, major advances in these sensors are required in terms of simple structure, lower cost, selectivity, durability and reliability. Chemical sensors can be schematically described as composed of a sensitive part which, interacting with the surrounding environment, collects and concentrate molecules at or within the surface undergoing physical changes, and of an opportune transducer that converts into an interpretable and quantifiable term such modification of the sensing part (see figure1.1).

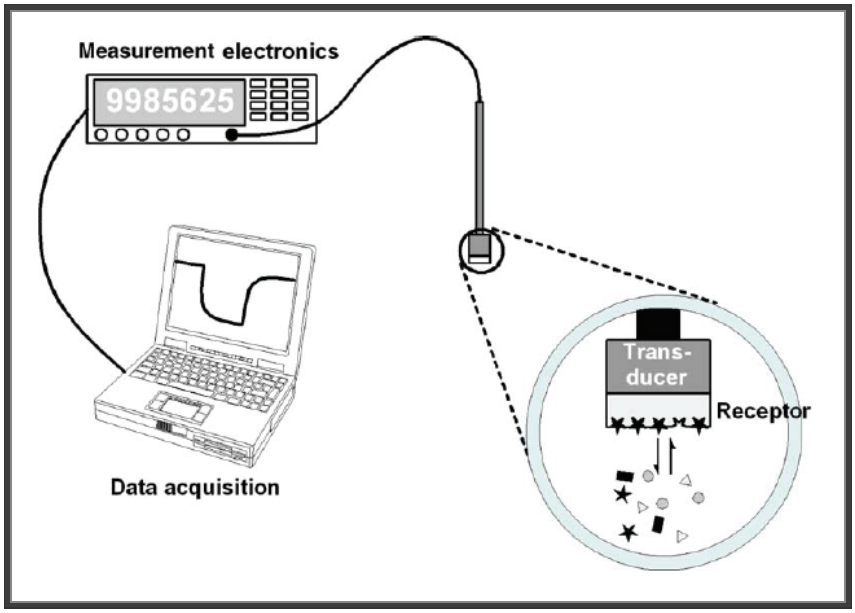

Figure 1.1 Typical arrangement of a chemical sensor.

The heart of the chemical sensor is the sensitive element which is the interface between the transducer and external environment so that the nature, the selectivity and sensitivity of the sensor depends upon these interactive materials. Arguably the most severe limitation on current chemical sensors technology is the inability to obtain a selective response to a target analyte, given the millions of known molecular species, the variations in environmental conditions (presence of water, etc.) and the variations in analyte amount or concentration by factors of 10^{23} or greater. For this reason, good materials to use as sensing part should optimize specific interactions with target analyte or narrow class of analytes, should

provide a fast and reversible diffusion of the penetrants, small recovery times and should maintain the physical state so as the geometry over several cycles of use, in order to avoid hysteresis effects, and thus to ensure the reproducibility [20].

In summer, ideal chemical sensors should present: - high sensitivity towards chemical compounds; - high selectivity (low cross sensitivity); - high stability; - low sensitivity to humidity and temperature; - high reproducibility and reliability; - short reaction and recovery time; - be robust and durable; - easy calibration; - small dimensions (portability). Most of these properties are dependent not only on the used material, but also on the method used for its synthesis, and specially on the additives present on the material surface and the method used for their addition.

Chemical sensors are generally categorized according to the principal physics and operating mechanisms of the sensor into four main groups [21]: (1) chromatography and spectrometry; (2) electrochemical sensors; (3) mass sensors; and (4) optical sensors. Chromatography relies on separation of complex mixtures by percolation through a selectively adsorbing medium, with subsequent detection of compounds of interest. Electro-chemical sensors include sensors that detect signal changes (e.g. resistance) caused by an electrical current being passed through electrodes that interact with chemicals. Mass sensors rely on disturbances and changes to the mass of the surface of the sensor during interaction with chemicals. Optical sensors detect changes in visible light or other electromagnetic waves during interactions with chemicals.

Polymers are among the most useful and used materials for chemical sensing since they comply to many of the requirements for a sensitive layer. In particular, they are able to collect and concentrate vapour molecules on sensor surfaces by reversible sorption; they can be deposited on several substrates as thin adherent films with easy processing techniques, and they are low cost. Polymers are available in many kinds having different chemical and sorption properties. The main approach for tuning sensitivity and selectivity is a chemical modification of side groups attached to the polymer backbone. More advanced strategies include the modification of

polymers to create syntethic cavities with cyclodextrins, cavitands, and calixarenes [22] or the use of molecularly imprinted polymers [23, 24]. The size exclusion principle of analyte molecules and specific interactions are in those cases the main reason for a selectivity towards certain analytes.

The versatility of polymers makes them usable in many sensor types based on different transduction principles, among which the most commonly exploited is the change in sensitive layer mass after exposure and consequent sorption of the target analyte. In opto-chemical sensors polymers are mainly used as a matrix to immobilize an indicator which can change its absorbance or its fluorescence emission in response to the analyte presence [25]. The unusual electronic and optical properties of conducting polymers have made them very attractive as transducer active materials in various sensing devices [26, 27].

Metal Oxides (MOX) are another interesting class of materials widely exploited in gas sensing applications using the change in their electrical conductivity due to the interaction process between the surface complexes such as O^-, O^{2-}, H^+ and OH^- reactive chemical species and gas molecules to be detected [28-30]. Thin film of MOX have been extensively used for the formation of highly sensitive, fast responding, micromachined and cheap gas sensors [31-33]. Most of the MOX-based chemical sensors are devices that translate the changes in the concentration of gaseous chemical species into electrical signals, generally changes of resistivity/conductivity [34]. However, the advantages of such metal oxide-based sensors have to be offset against certain disadvantages which, in some cases, limit their use in practice. In particular, their principle of operation and the high operating temperature at which they typically have to work to obtain the best sensitivity lead to an high power consumption and to the impossibility to be exploited in aqueous environments for example for water quality monitoring applications.

The natural step following the selective recognition of an analyte from the sensitive layer is the signal transduction, and thus the choice of an opportune technique to read the physical or chemical changes occurring at the sensing part. Widely exploited transduction principles in chemical

sensing are the mass change and the resistivity/conductivity change of the sensitive layer upon exposure to and consequent sorption of analytes. The first physical parameter is in many cases measured by the shift in the resonant frequency of an oscillating piezoelectric crystal. Depending on the kind of the vibrational wave propagated in the crystal, those sensors are classified as Quartz Crystal Microbalance (QCM) or Surface Acoustic Wave (SAW) sensors. They typically use a thin polymeric film as sensitive layer [35], however SAW and QCM-based chemical sensors using other sensitive coatings have been proposed [36-37]. Instead, changes in the resistivity/conductivity of sensitive layers are typically detected by conductometric measurement carried out on sensitive materials (mainly semiconducting metal oxides and conjugated polymers) deposited between two electrodes. That sensor technology carries the name of Metal Oxide Semiconductors (MOS) and Conductive Organic Polymer (COP) sensors [38].
Optical transduction techniques based on the use of optical fibres are also very attractive in chemical sensing applications due to some unique characteristics such as immunity to electromagnetic interference, small size, light weight, easy multiplexability, possibility of use in harsh environments, double function of probe and data communication channel [39]. In addition, optical sensing is very versatile as it can allow simultaneous collection of intensity and wavelength information, and encompass a wide range of techniques (absorbance, reflectance, fluorescence, surface plasmon resonance, refractive index and colorimetry) [40-46].
A detailed description of fibre optic chemical sensors will be given in the next section.
However it is worth noting that a well designed, high performance, robust chemical sensor is not just a matter of sensitive material and sensing platform choice, but also of their effective integration which implies an appropriate deposition technique [47].

1.2 Fibre optic chemical sensors.

Fibre optic chemical sensors are a class of sensors that use optical fibres to detect chemical contaminants. Light is generated by a light source and is sent through an optical fibre. The light then returns through the optical fibre and is captured by a photodetector. Some optical fibre sensors use a single optical fibre while others use separate optical fibres for the light source and for the detector. There are three general classes of fibre optic sensors (see Figure 1.2). The first type is completely passive. A spectroscopic method can be used to detect individual types of contaminants. This method involves sending a light source directly through the optical fibre and analyzing the light that is reflected or emitted by the contaminant. The refractive index of the material at the tip of the optical fibre can be used to determine what phases (vapor, water) are present. It's worth noting, however, that even if chemical sensors have been defined as composed of a chemo-sensitive layer and a physical transducer, an exception is made for the aforementioned direct fibre optic chemical sensors which probe directly without an intermediate layer the presence of analytes, for example exploiting the intrinsic absorption spectrum of a pollutant in a medium [48]. Hence these techniques are more similar to the conventional analytical chemistry laboratory techniques and exploits the fibre optic just as a channel to gather or collect the light from the sample.

A second class of fibre optic sensors consist of a fibre optic sensor with a chemically interacting thin film deposited onto the tip [49]. This type of sensors, also called indirect fibre optic chemical sensors, belongs to the general definition of chemical sensors given at the beginning and this chapter.

The sensitive film is formulated to bind with certain types of chemicals. Contaminant concentration can be found by measuring the color of the thin film, the change in refractive index, or by measuring the flourescing of the film.

The third type of fibre optic sensors involves injecting a reagent near the sensor. This reagent reacts either chemically or biologically with the

contaminant. The reaction products are detected to give an estimate of the contaminant concentration.

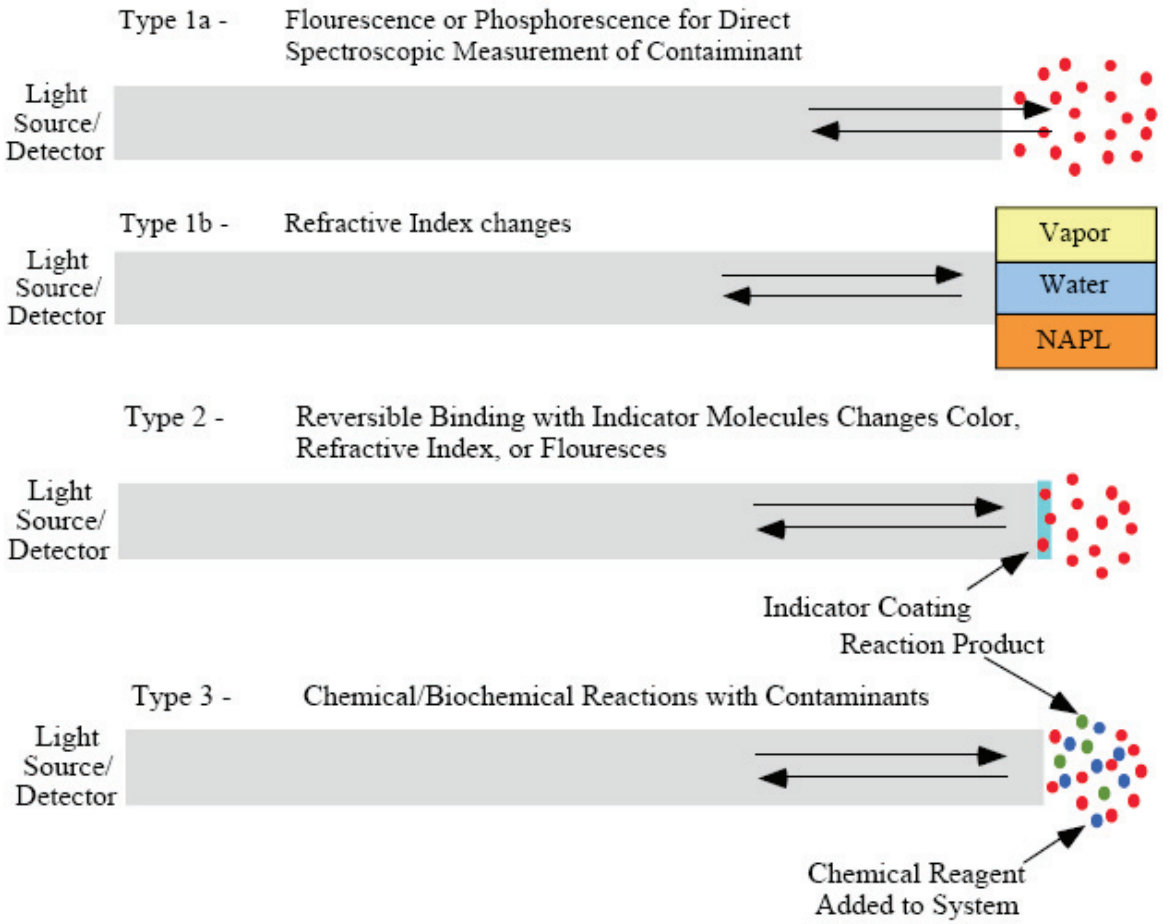

Figure 1.2. Three types of fibre optic chemical sensors.

Compared with other types of sensors, fibre optic sensors offer many benefits as following:

1. Sensed signal is immune to electromagnetic interference (EMI) and radio frequency interference (RFI);
2. Intrinsically safe in explosive environments;
3. Highly reliable and secure with no risk of fire/sparks;
4. High voltage insulation and absence of ground loops and hence obviate any necessity of isolation devices like optocouplers;

5. Low volume and weight, e.g., one kilometer of 200um silica fibre weighs only 70 gm and occupies a volume of about 30 cm^3;
6. As a point sensor, they can be used to sense normally inaccessible regions without perturbation of the transmitted signals;
7. Potentially resistant to nuclear or ionizing radiation;
8. Can be easily interfaced with low-loss optical fibre telemetry and hence affords remote sensing by locating the control electronics for LEDs/lasers and detectors far away from the sensor head;
9. Large bandwidth and hence offers possibility of multiplexing a large number of individually addressed point sensors in a fibre network or distributed sensing i.e. continuous sensing along the fibre length;
10. Chemically inert and they can be readily employed in chemical, process and
biomedical instrumentation due to their small size and mechanical flexibility;
11. High sensitivity, high accuracy and cost-effectiveness.

These advantages give the opportunity to develop fibre optic sensors for accurate sensing and measurement not only of chemicals but also of physical parameters and fields, e.g., pressure, temperature, liquid level, electric current, rotation, displacement, acceleration, acoustic, electric and magnetic fields and so on. These benefits have promoted a worldwide research activity in optical fibre sensing.
The major drawback of fibre optic chemical sensors concerns the selectivity; in fact it is a great challenge of the worldwide ongoing research to obtain a selective response to a target analyte.

References

[1] N. Fukatsu, N. Kurita, K. Kiode and T. Ohashi, Solid State Ionics 113-115, 219-227 (1998).

[2] S.A. Akbar and P.K. Dutta, "Ceramic Sensors for Industrial Applications," in Encyclopedia of Materials: Science and Technology, Elsevier 1080-1086, (2001).

[3] K. Swift, Industrial Sensor Technologies and Market, BCC, Inc. Report, GB-200R, (2002).

[4] M. Batzill and U. Diebold, "The surface and materials science of tin oxide," Prog. Surf. Sci. 79, 47-154 (2005).

[5] P. Gorley, V. Khomyak, S. Bilichuk, I. Orletsky, P. Horley, and V. Grechko, "SnO_2 films: Formation, electrical and optical properties," Mater. Sci. Eng., B, 118, 160–163 (2005).

[5] O. Scarlat, S. Mihaiu, G. Aldica, J. Groza, and M. Zaharescu, "Semiconducting densified SnO_2-ceramics by a novel sintering technique," J. Eur. Ceram. Soc. 24, 1049-1052 (2004).

[7] S. G. Sazhin, E. I. Soborover, and S. V. Tokarev, "Sensor methods of ammonia inspection," Russ. J. Nondestruct. Test. 39, 791-806 (2003).

[8] B. Timmer, W. Olthuis, and A. van den Berg, "Ammonia sensors and their applications-A review," Sens. Actuators B 107, 666-677 (2005).

[9] M. Pisco, M. Consales, R. Viter, V. Smyntyna, S. Campopiano, M. Giordano, A. Cusano, A. Cutolo, "Novel SnO_2 based optical sensor for detection of low ammonia concentrations in water at room temperatures," Semiconductors Physics, Quantum Electronics and Optoelectronics 8, 95-99 (2005).

[10] M. Pisco, M. Consales, S. Campopiano, R. Viter, V. Smyntyna, , M. Giordano and A. Cusano, "A novel optochemical sensor based on SnO_2 sensitive thin film for ppm ammonia detection in liquid environment," Journal of Lightwave Technology 24, 5000-5007 (2006).

[11] E. M. Logothetis "Automotive oxygen sensors", Chemical Sensor Technology 3, 89-104 (1991).

[12] A. M. Azad, S. A. Akbar, S. G. Mhaisalkar, L. D. Birkefeld and K. S. Goto, J. Electrochem. Soc. 139, 3690-3704 (1992).

[13] N. Yamazoe and N. Miura, Sensors and Actuators B 20, 5-102 (1994).
[14] S. Viswanathan , R. G. Reddy and J. C. Malas, “Sensors and Modeling in Materials Processing: Techniques and Applications,” The Minerals, Metals and Materials Society, Warrendale PA (1997).
[15] N. Fukatsu, N. Kurita, K. Kiode and T. Ohashi, Solid State Ionics, 113-115 219-27 (1998).
[16] S.A. Akbar and P.K. Dutta, "Ceramic Sensors for Industrial Applications," in Encyclopedia of Materials: Science and Technology, Elsevier, 1080-1086, (2001)
[17] O.W. Bynum, D.R. Sheridan and J.A. White, GRI Report 92/0373, (1992).
[18] H. T. Nagle., S. S. Schiffman and R. Gutierrez-Osuna, “The How and Why of Electronic Noses,” IEEE Spectrum 35, 22-34 (1998).
[19] K. Swift, Industrial Sensor Technologies and Market, BCC, Inc. Report, GB-200R, (2002).
[20] J. W. Grate, M. H. Abraham, “Solubility interaction and design of chemically selective sorbent coatings for chemical sensor and arrays,” Sensors and Actuators B 3, 85-111(1991).
[21] J. Jannata, Principles of chemical sensors, New York Press: Plenum (1989).
[22] W. Gopel, “Supramolecular and polymeric structures for gas sensors,” Sensors and Actuators B 24/25, 17-32 (1995).
[23] S. Wei, M. Jakusch, B. Mizaikoff, “Capturing molecules with templated materials-Analysis and rational design of molecularly imprinted polymers,” Analytica Chimica Acta 578, 50-58 (2006).
[24] M.C. Moreno-Bondi et al., “Molecularly imprinted polymers as selective recognition elements for optical sensors based on fluorescent measurements,” 12th International Conference on Transducers, Solid-State Sensors, Actuators and Microsystems, Volume 2, 975-978 (2003).
[25] L. L. Blyler Jr, R. A. Lieberman, L. G. Cohen, J. A. Ferrara, J. B. Macchesney, “Optical fibre chemical sensors utilizing dye-doped silicone polymer claddings,” Polymer Engineering and Science 29, Issue 17, 1215-1218.

[26] Marek Trojanowicz, "Application of Conducting Polymers in Chemical Analysis," Microchim. Acta 143, 75-91 (2003).
[27] Liming Dai, Prabhu Soundarrajan, and Taehyung Kim, "Sensors and sensor arrays based on conjugated polymers and carbon nanotubes," Pure Appl. Chem.74, No. 9, 1753-1772 (2002).
[28] G. Sberveglieri, "Recent developments in semiconducting thin-film gas sensors," Sens. Act. B 23, 103-109 (1995).
[29] V. Guidi, G. C. Cardinali, L. Dori, G. Faglia, M. Ferroni, G. Martinelli, P. Nelli, G. Sberveglieri, "Thin-film gas sensor implemented on a low-power-consumption micromachined silicon structure," Sensors and Actuators B, 49 88-92 (1998).
[30] C. Baratto, E. Comini, G. Faglia, G. Sberveglieri, M. Zha, A. Zappettini, "Metal oxide nanocrystals for gas sensing," Sensors and Actuators B 109, 2-6 (2005).
[31] W. Gopel, "Chemical imaging: I. Concepts and visions for electronic and bioelectronic noses," Sens. Actuators B 52, 125-142 (1998).
[32] U. Weimar, W. Gopel, "Chemical imaging: Trends in practical multiparameter sensor systems," Sens. Actuators B 52, 143-161 (1998).
[33] I. Simon, N. Barsan, M. Bauer, U. Weimar, "Micromachined metal oxide gas sensors: opportunities to improve sensor performance," Sens. Actuators B 73, 1-26 (2001).
[34] N. Barsan, U. Weimar, "Conduction Model of Metal Oxide Gas Sensors", J. of Electroceramics 7, 143-167 (2001).
[35] J. W. Grate, "Acoustic Wave Microsensor Arrays for Vapor Sensing," Chemical Society Reviews 100, 2627-2647 (2000).
[36] M. Penza, G. Cassano, P. Aversa, F. Antolini, A. Cusano, M. Consales, M. Giordano, L. Nicolais, "Carbon nanotubes coated multi-transducing sensors for VOCs detection," Sensors and Actuators B 111-112, 171-180 (2005).
[37] J. Zhang, J. Hu, Z. Q. Zhu, H. Gong, S. J. O'Shea, "Quartz crystal microbalance coated with sol–gel-derived indium–tin oxide thin films as gas sensor for NO detection," Colloids and Surfaces A: Physicochemical and Engineering Aspects Volume: 236, Issue: 1-3, 23-30 (2004).

[38] D. James, S. M. Scott, Z. Ali, and W. T. O'Hare, "Chemical Sensors for Electronic Nose Systems," Microchim. Acta 149, 1-17 (2005).
[39] G. Boisdè and A. Harmer, "Chemical and Biochemical Sensing With Optical Fibers and Waveguides", Artech House Boston-London (1996).
[40] I. M. Steinberg, A. Lobnik, O. S. Wolfbeis, "Characterisation of an optical sensor membrane based on the metal ion indicator Pyrocatechol Violet," Sensors and Actuators B 90, 230-235 (2003).
[41] Guillermo Orellana, "Luminescent optical sensors," Analytical and Bioanalytical Chemistry 379, N. 3 (2004).
[42] J. Homola, S. S. Yee, G. Gauglitz, "Surface plasmon resonance sensors: review," Sensors and Actuators B 54, 3-15 (1999).
[43] A. G. Mignani, L. Ciaccheri, A. Cimato, C. Attilio, P. R. Smith, "Spectral nephelometry for the geographical classification of Italian extra virgin olive oils," Sensors and Actuators B 111–112, 363–369 (2005).
[44] A. G. Mignani, Andrea A. Mencaglia, Leonardo Fiaccheri, "Fiber optic systems for colorimetry and scattered colorimetry," Optical Fibers: Technology. Edited by J. Rayss, B. Culshaw, A. G. Mignani, Proceedings of the SPIE, Volume 5952, 89-99 (2005).
[45] F. J. Arregui, I. R. Matias, R. O. Claus, "Optical Fiber Gas Sensors Based on Hydrophobic Alumina Thin Films Formed by the electrostatic Self-Assembly Monolayer Process," IEEE Sensors Journal, Vol.3, No.1, (2003).
[46] R. Falciai, A. G Mignani., A. Vannini, "Long period gratings as solution concentration sensors," Sensors and Actuators B 74, 74-77 (2001).
[47] S. W. James, R. P. Tatam, "Fibre Optic sensors with nano-structured coatings," J. Opt. A 8, S430-S444.A. G. Mignani, A. A. Mencaglia, "Direct and
[48] Chemically mediated absorption spectroscopy using optical fiber instrumentation," IEEE Sensors Journal, Vol. 2, No.1 (2002).
[49] D. R. Walt, "Fiber optic sensors for continuous clinical monitoring," Proceedings of the IEEE 80, (1992).

CHAPTER 2

Material and deposition technique

2.1 Tin oxide

Tin oxide has recently received a great scientific interest because of its wide range of applications. Thus, looking only at the most recently reported applications, it has been studied as overcoat for thin film magnetic recording media [1], as electrode material in solar cells, light emitting diodes, flat panel displays, and other optoelectronic devices where an electric contact needs to be made without obstructing photons from either entering or escaping the optical active area [2, 6]. Efficiency in some applications is usually improved by suitably doping the tin oxide with selected element; for example Sb doped tin oxide deposited on titanium presents high overpotentials for the oxygen generation reaction, thereby giving good anodes for the electrochemical oxidation of both organic pollutants and cyanide [7]. It is also investigated as material for Li-ion batteries [8-10]. Moreover in recent time, the development of tin oxide thin films as gas sensors has attracted considerable interest [11].

Among the large variety of materials used in gas sensors, the market is dominated by metal oxide semiconductors, usually known simply as semiconductor gas sensors (SGS). As mentioned into the previous chapter, SGS detection signal is based on the change of material resistivity after gas exposure, being usually maximum at temperatures ranging from 200 to 800 ^{0}C, always depending on tested gas, the own sensor material and its doping. Thus, after Brattain and Bardeen demonstrated already in 1953 [12] that gas adsorption at the surface of Ge lead to a significant variation of the conductance, the first built structure to be used as gas sensor, making use of this phenomena, has been attributed to Seiyama (ZnO sensor) and Taguchi in 1962 [13, 14], while the first SGS based on SnO_2 were developed later in 1970 by Taguchi [15]. Initially they were known as Taguchi or Figaro

sensors (the inventor and the name of the company that commercialised the sensors, respectively). Since that moment SnO_2 has become the most investigated material for SGS.

The study of SnO_2 as gas sensing material is due to its suitable physicochemical properties as, for example, it has a high reactivity to reducing gases at relatively low operating temperatures thanks to the easy adsorption of oxygen at its surface because of the natural non-stoichiometry of SnO_2. Moreover, SnO_2 has a lower cost when compared to actual available materials for similar applications. Nowadays, the research on this material is focused to increase its sensitivity, selectivity and stability, and one of the main issue to accomplish these issues is the presence of metals at low concentrations. Thus, the presence of a certain metal on the SnO_2 surface improves the properties of the material with respect to certain gases, which are different depending on the added metal.

2.1.1 Intrinsic behaviour of tin oxide

Commonly, a material is selected for a defined application on the base of its intrinsic properties and, dealing with chemical processes, the materials properties can be divided into bulk properties and surface properties. Within the subject of this work, the most important properties are those concerning the surface of the material, although we cannot forget the influence of the bulk properties. Thus, we will begin this section briefly describing the bulk properties of tin oxide. Afterwards, we will introduce the influence of the surface of the material in the resistive gas-sensing mechanism, while the sensing mechanics of the proposed SnO_2 based optical sensors will be reported in the chapter 3. Nevertheless, it must be stated that the current status of physics and chemistry are not developed enough to know clearly the effects of surface properties on gas sensitivity, and here we refer to the most accepted theories at the current development of the field.

There are two main oxides of tin: stannic oxide (SnO_2) and stannous oxide (SnO). The existence of these two oxides reflects the dual valency of tin, with oxidation states of 2+ and 4+. Stannous oxide is less well characterized than SnO_2. For example, its electronic band gap is not accurately known but lies

somewhere in the range of 2.5–3 eV. Thus SnO exhibits a smaller band gap than SnO_2 , which is commonly quoted to be 3.6 eV. Also, there are no single crystals available that would facilitate more detailed studies of stannous oxide.

Stannic oxide possesses the rutile structure and stannous oxide has the less common litharge structure. Stannic oxide is the more abundant and the thermodynamically most stable form of tin oxide; moreover it is the one of technological significance in gas sensing applications and oxidation catalysts because of its high chemical and mechanical stability [16].

In addition to the common rutile (tetragonal) structured SnO_2 phase there also exists a slightly more dense orthorhombic high pressure phase.

As a mineral SnO_2 is also called Cassiterite. As said above it possesses the same rutile structure as many other metal oxides, e.g. TiO_2, RuO_2, GeO_2, MnO_2, VO_2, IrO_2, and CrO_2. The rutile structure has a tetragonal unit cell with a space-group symmetry of $P4_2/mnm$ (see figure 1.2). The lattice parameters are a = b = 4.7374 A ˚ and c = 3.1864A ˚. The atomic position at 300 K in the unit cell is (0,0,0) and (1/2, ½, ½) for the metal and ±(u, u, 0) and (½+u, ½-u, ½), being u=0.387, for the oxygen. The rest of the atoms of the unit cell can be obtained applying the rutile symmetry D^{14}_{4h} [16-18]. The corresponding heat of formation is $\Delta H = 1.9\ 10^3$ J mol^{-1}, the heat capacity of the material is $C_p = 52.59$ J mol^{-1} K^{-1}, the density at 300 K is 6.95 g cm^{-3} and the melting point is 1630 ^{0}C.

All over this work we will always deal with stanninc dioxide.

Pure tin oxide is an n-type semiconductor due to the presence of oxygen vacancies, which electronically act as electron donors. In fact, surface sheet conductance measurements have shown how oxygen vacancies in (110) surfaces can increase the surface conductivity by more than two orders of magnitude with respect to the bulk conductivity [19]. In the same way, it is unambiguously agreed that the conductance change on exposure to gases arises mainly through a surface phenomenon on the SnO_2 grains.

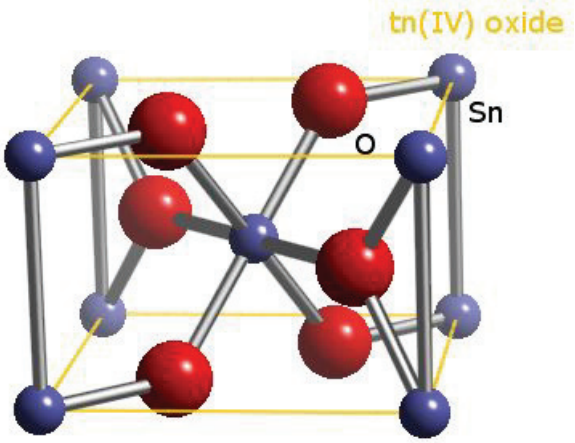

Figure1.2. Unit cell of the crystalline structure of SnO_2.

As has been commented above, tin oxide is an n-type semiconductor due to the existence of the native donor levels. These levels have energies of 0.03-0.034eV and 0.14-0.15eV below the conduction band edge, and are generally attributed to single and double ionisation of oxygen vacancies [20, 21], as unrelaxed vacancies are above, i.e., within the conduction band. The position of the Fermi level is fixed and would be between the conduction band edge and the intrinsic Fermi level position (that is very close to the mid of the band gap), because SnO_2 presents a negligible concentration of electronic band-gap states at their geometrically ideal surfaces.

Nevertheless, the above discussion is not valid for a polycrystalline material formed by crystallites, mainly due to two effects: the presence of grain boundaries and the own crystallite size. Thus, the areas of grain interphasing, i.e. grain boundaries, are formed by several layers of atoms displaced from their original positions, thereby allowing the coupling between the crystalline lattices of both crystals. The natural disorder of grain boundaries results in the modification of the local band structure of the material due to the appearance of interfacial energetic levels within the band gap. The origin of these levels is conditioning the behaviour as acceptor or donor levels. With respect to the influence of crystal size, it is mainly due to the fact that as grain size is reduced, the number of ideal surfaces (i.e., those with negligible band gap states) reduces as well and in

the case of nanoparticles, these ideal surfaces do not exist, thereby increasing the number of unreconstructed surfaces, dangling bonds, and surface vacancies, that induce acceptor or donor levels at the grain surface.
The existence of surface or interface traps acting as acceptors or donors, each of them having a certain density of states and certain parameters of emission and capture, makes that in the thermodynamic equilibrium at each temperature, the Fermi level position is determined by this region. The charge trapped at grain boundaries or surfaces is compensated by opposite charged depletion regions surrounding them. However, a direct association between the created states, their activity, their location in the band gap and the type of defects from where they are caused cannot be predicted a priori. Nevertheless, for an n-type semiconductor, in the case of grain boundaries the position of the Fermi level in the grain boundary has to be lower than the corresponding position in the bulk material just to generate the band bending of the surface (for more details see ref. 22).

2.1.2 Effect of gases in contact with the surface

When SnO_2 is exposed to an atmosphere at moderate temperatures, two things can occur, namely, gas adsorption due to the high reactivity of the SnO_2 surface or reaction of interaction of the gas molecules with the molecules chemisorbed at the SnO2 surface. Gas adsorption, understood as a direct chemical interaction between the gas molecules and the semiconductor surface is accompanied by charge exchange. Such interchange is interpreted from the electronic point of view as the creation of an inter-band-gap level whose occupation probability is given by the Fermi-Dirac distribution function when equilibrium is achieved. Its behaviour as acceptor or donor will depend on the type of molecule adsorbed. Thus, gases that capture electrons from the bulk of SnO_2 when they are adsorbed create acceptor levels, while gases that give electrons to the SnO2 through the creation of an oxygen vacancy introduce donor levels. On the other hand, reaction of molecules in the gas phase with those existing already on the semiconductor surface is interpreted as the annihilation of the previously created forbidden band-gap states. Nevertheless in most

cases there is not a direct relationship between the presence of a certain gas in the ambient and the type of level created or annihilated because some intermediate reactions can occur [23]. Moreover, for a single gas molecule impinging on a modified oxide sensing surface, whether the molecule is "detected" or not depends on whether its interaction with the active sensor element is sufficiently strong and of significant duration, and it is through a statistically large number of such local events, on the atomic and molecular scale, that a collective response (macroscopic signal) is produced.

There are two types of adsorption: physisorption and chemisorption, depending on the strength of the binding. Physisorption is considered when the energy of the bond is of the order of 0.01-0.1eV, while chemical adsorption is considered when the adsorbed molecules are bound to the semiconductor with bonding energy as large as 1eV. Such difference is due to the underlying adsorptive forces, as physisorption is caused by dispersion forces, forces of electrostatic nature and electrical image forces, whereas chemisorption is based on the stronger covalent forces (overlapping between the adsorbate and adsorbent wave functions) and, hence, is connected with a partial electron transfer between adsorbent and adsorbate [24].

Thus, it is only after chemisorption that the charge displacement occurs between the gas and the semiconductor surface and, as it has been explained, this interchange of charge gives rise to a band bending in the surface region, to a change of the surface conductivity and to a change in the electron affinity, due to the creation of dipoles at the surface [25].

Chemisorption may also produce changes in the surface mobility, as ionosorbed molecules play an important role in electronic conduction as charged scattering centres at the surface [26].

Once the surface of the semiconductor is occupied by adsorbed molecules, new molecules trying to adsorb experience a new environment in such a way that the amount of total ions adsorbed is limited to a coverage of $\approx 10^{-2}$-10^{-3} monolayers for electrostatic reasons (Weisz limitation) [27]. For example, in the case of oxygen chemisorption, the positive charge appearing in the semiconductor surface as a consequence of adsorption causes a band bending of up to about 1eV and a thickness of the depletion layer of about 1

to 10 μm [23]. With growing surface density of chemisorbed oxygen, the band bending of the depletion layer increases, shifting the level of surface acceptors above the Fermi level, thus limiting the adsorption of new arriving oxygen molecules. This limitation could be overcome if acceptor levels are introduced by other gases but, because of the existence of interface traps, the Fermi level can be pinned, making the material insensitive to the adsorption of certain ions.

Temperature has pronounced effects on the sensitivity of SnO_2 resistive gas sensors, as it influences the physical properties of semiconductors (change of the free carrier concentration, Debye length,…), but also because every reaction taking place at the surface of the semiconductor, as well as the most probable species adsorbed and, hence, the reaction sites, are temperature dependent. So, temperature specially affects those properties related to the processes occurring at the surface of the sensor. For example, adsorption and desorption processes are temperature activated processes, as well as surface coverage by molecular and ionic species, chemical decomposition and reactive sites. In this way, dynamic properties of the sensors such as response and recovery time and the static characteristics of the sensor depend on the temperature of operation [28], and a temperature for which the sensitivity of a semiconductor gas sensor is maximum is always observed.

2.2 Electrostatic spray pyrolysis technique

The chemical spray pyrolysis technique has been, during last three decades, one of the major techniques to deposit a wide variety of materials in thin film form. Many studies have been done, since the pioneering work by Chamberlin and Skarman [29] in 1966 on cadmium sulphide (CdS) films for solar cells.

Thereafter, due to the simplicity of the apparatus and good productivity of this technique on a large scale it offered a most attractive way for the formation of thin films of noble metals, metal oxides, spinel oxides, chalcogenides and superconducting compounds [30]. Despite its simplicity, spray pyrolysis (SP) has a number of advantages. (1) Unlike closed vapour deposition methods SP does not require high quality targets and-or substrates nor does it require vacuum at any stage, which is a great advantage if the technique is to be scaled up for industrial applications. (2) The deposition rate and the thickness of the films can be easily controlled over a wide range by changing the spray parameters, thus eliminating the major drawbacks of chemical methods such as sol-gel which produces films of limited thickness. (3) Operating at moderate temperatures (100 - 500 °C), SP can produce films on less robust materials. (4) Unlike high-power methods such as radio frequency magnetron sputtering (RFMS), it does not cause local overheating that can be detrimental for materials to be deposited. There are virtually no restrictions on substrate material, dimension or its surface profile. (5) By changing composition of the spray solution during the spray process, it can be used to make layered films and films having composition gradients throughout the thickness. (6) It offers an extremely easy way to dope films with virtually any element in any proportion by merely adding it in some form to the spray solution. (7) It is believed that reliable fundamental kinetic data are more likely to be obtained on particularly well characterized film surfaces, provided the films are quite compact, uniform and that no side effects from the substrate occur. SP offers such an opportunity.

The prime requisite for obtaining good quality thin film is the optimisation of preparative conditions versus substrate temperature, spray rate

concentration of solution etc. However, in recent years an emphasis has been given to a variety of atomization techniques such as ultrasonic nebulisation, improved spray hydrolysis, corona spray pyrolysis, microprocessor based spray pyrolysis and electrostatic spray pyrolysis. This is the most critical parameter as it enables control over the size of the droplets and their distribution over the preheated substrates.

Among the reported atomization technique we selected the newly developed electrostatic spray pyrolysis (ESP), because of its facility to produce the uniform particles, simplicity of ambient atmospheric apparatuses, and selectivity of inexpensive and harmless solvents such as water or ethanol [31- 44].

The main principle of the method is the phenomenon of polarization of electrolyte (usually ethanol or water solutions of metal chlorides) on charged droplets by electrostatic field, applied between a vessel provided with a metal capillary and a heated substrate. The polarized droplets separate one from each other by means of repulsive forces and are carried by electrostatic field along its force lines [45]. The moving droplets form a cone in the space, called Tailor's cone [44]. The coverage of the substrate by droplets is quasi uniform in terms of amount of drops per square unit. When droplets of solution reach the heated substrate (the temperature of the substrate is usually in the range 300-450°C), chemical reaction of metal chloride with water vapor of solution, stimulated by the temperature, takes place with formation of the oxide film [46]:

$$MCl_x + \frac{x}{2} H_2O \rightarrow MO_{\frac{x}{2}} + xHCl$$

Thereby, MOX layer grows due to the thermal transformation of metal chloride to metal oxide as a consequence of the interaction with water vapor. In other words, the pyrolytic reaction leads to the deposition of a film of the desired compound while all the unreacted specie and other reaction products leave the system as volatile components. All the deposition cycle usually is carried out in atmosphere with air pressures close to 10^5 Pa.

The most important deposition parameters of the ESP are the metal chloride concentration, the precursor solution volume and the substrate

temperature [44]. It was shown that the concentration of the sprayed solution plays an important role in the morphology of the film. In particular, the higher concentration of the precursor the higher the roughness of the film surface [44]. The substrate temperature during the deposition procedure determines structural properties of the layers like crystalline size and surface morphology and electrical properties like resistivity and charge carrier mobility. For the samples deposited at higher temperatures, low resistivity and higher roughness were observed whereas for films deposited at temperatures less than 340°C high resistivity, lower crystalline size and less ratio of polycrystalline phase were found [47]. In light of this consideration it's evident that the films properties can be tailored by varying the deposition parameters.

References

[1] V. J. Novotny, A. S. Kao, "Tin oxide overcoats for thin film magnetic recording media," Magnetics, IEEE Transactions 26, 2499-2501 (1990).

[2] R. E. Presley, C. L. Munsee, C. H. Park, D. Hong, J. F. Wager, D. A. Keszler, "Tin oxide transparent thin-film transistors," J. Phys. D 37 2810 (2004).

[3] M. Iwamoto, K. Shimono, M. Sumi, K. Koyama, N. Kamo, J. Phys. Chem. B, *103*, 10311 (1999).

[4] E. Ando, S. Suzuki, J. Shimizu, Y. Hayashi, Thin Solid Films, 351, 301 (1999).

[5] C. Nasr, S. Hotchandani, P.V. Kamat, J. Phys. Chem. B 102, 4944 (1998).

[6] A.K. Jana, J. Photochem. Photobiol. A: Chemistry 132, 1 (2000).

[7] W. Liu, X. Huang, Z. Wang, H. Li, L. Chen, J. Electrochem. Soc. 145(1), 59 (1998).

[8] A.M. Polcaro, S. Palmas, F. Renoldi, M. Mascia, J. Appl. Echem. 29, 147 (1999).

[9] R. Retoux, T. Brousse, D.M. Schleich, J. Electrochem. Soc. 146 (7), 2472 (1999).

[10] J. Morales, L. Sánchez, J. Electrochem. Soc. 146(5), 1640 (1999).

[11] P. Siciliano, "Preparation, characterization and applications of thin films as gas sensors by cheap chemical method,"Sens. Actuators B 70, 153-164 (2000).

[12] W.H. Brattain, J. Bardeen, Bell Systems Tech. J. 1953, 32, 1.

[13] T. Seiyama, A. Kato, K. Fujiishi, M. Nagatani, Anal. Chem. 34, 1502. (1962).

[14] N. Taguchi, Jpn. Patent 45-38200, (1962).

[15] N. Taguchi, UK Patent 1280809, (1970) and K. Taguchi, US Patent 3631436 (1970).

[16] A. Nanthakumar and N.R. Armstrong, in "Semiconductor Electrodes", ed. by H.O. Finklea, Studies in Physical and Theoretical Chemistry 55, Elsevier, Amsterdam (1988).

[17] C. Klein, C.S. Hurlbut, Jr., Manual of Mineralogy, J. Wiley & Sons, Inc. 21st Ed., (1997).

[18] S. Munnix, M. Schmeits, Phys. Rev. B, 27(12), 7624 (1983).
[19] J. Robertson, Phys. Rev. B 30, 3520 (1984).
[20] S. Samson, and C.G. Fonstad, J. Appl. Phys. 44, 4618 (1973).
[21] C.G. Fonstad and R.H. Rediker, J. Appl. Phys. 42, 2911 (1971).
[22]A. Diéguez, Ph. D. Thesis, Universitat de Barcelona, (1999) Available on line at: http://nun97.el.ub.es/~dieguez/tesis/initesis.html
[23] D. Kohl, Sens. Act., 18, 71 (1989).
[24] H. Geistlinger, Sens. Act. B 17, 47 (1993).
[25] W. Göpel, Sens. Act. 16, 167 (1989).
[26] M. Kanamori, K. Suzuki, Y. Ohya, and Y. Takahashi, Jpn.J. Appl. Phys. 33, 6680 (1994).
[27] P.B. Weisz, J. Chem. Phys. 21, 1531 (1953).
[28] J. Mizsei, Sens. Act. B 23, 173 (1995).
[29] R.R. Chamberlin, J.S. Skarman, J. Electrochem. Soc. 113, 86 (1966).
[30] Pramod S. Patil, "Versatility of chemical spray pyrolysis technique," Materials Chemistry and Physics 59, 185-198 (1999).
[31] E.M. Kelder, O.C.J. Nijs, J. Schoonman, Low-temperature synthesis of thin films of YSZ and BaCeO3 using electrostatic spray pyrolysis (ESP), Solid State Ionics 68, 5–7 (1994).
[32] A.A. van Zomeren, E.M. Kelder, J.C.M. Marijnissen, J. Schoonman, "The production of thin films of LiMn2O4 by electrospraying," J. Aerosol Sci. 25, 1229–1235 (1994).
[33] C.H. Chen, A.A.J. Buysman, E.M. Kelder, J. Schoonman, "Fabrication of LiCoO2 thin film cathodes for rechargeable lithium battery by electrostatic spray pyrolysis," Solid State Ionics 80, 1–4 (1995).
[34] C. Chen, E.M. Kelder, P.J.J.M. van der Put, J. Schoonman, "Morphology control of thin LiCoO2 films fabricated using the electrostatic spray deposition (ESD) technique, " J. Mater. Chem. 6, 765–771 (1996).
[35] N.H.J. Stelzer, J. Schoonman, "Synthesis of terbia-doped yttria stabilized zirconia thin films by electrostatic spray deposition (ESD)," J. Mater. Synth. Process. 4, 429–438 (1996).
[36] C.H. Chen, K. Nord-Varhaug, J. Schoonman, "Coating of yttria stabilized zirconia (YSZ) thin films on gadolinia-doped ceria (GCO) by the

electrostatic spray deposition (ESD) technique," J. Mater. Synth. Process. 4, 189–194(1996).

[37] C.H. Chen, E.M. Kelder, M.J.G. Jak, J. Schoonman, "Electrostatic spray deposition of thin layers of cathode materials for lithium battery," Solid State Ionics 86–88, 1301–1306 (1996).

[38] C.H. Chen, E.M. Kelder, J. Schoonman, "Unique porous LiCoO2 thin layers prepared by electrostatic spray deposition," J. Mater. Sci. 31 5437–5442, (1996).

[39] C.H. Chen, E.M. Kelder, J. Schoonman, "Electrode and solid electrolyte thin films for secondary lithium-ion batteries," J. Power Sources 68, 377–380 (1997).

[40] H. Gourari, M. Lumbreras, R.V. Landschoot, J. Schoonman, "Elaboration and characterization of SnO_2–Mn2O3 thin layers prepared by electrostatic spray deposition," Sens. Actuators B 47, 189–193 (1998).

[41] C.H. Chen, E.M. Kelder, J. Schoonman, "Electrostatic sol-spray deposition (ESSD) and characterisation of nanostructured TiO2 thin films, Thin Solid Films 342, 35–41 (1999).

[42] D. Zaouk, Y. Zaatar, A. Khoury, C. Llinares, J.-P. Charles, J. Bechara, "Electrical and optical properties of pyrolytically electrostatic sprayed fluorine-doped tin-oxide: dependence on substrate-temperature and substrate-nozzle distance," J. Appl. Phys. 87, 7539–7543 (2000).

[43] D. Zaouk, Y. Zaatar, A. Khoury, C. Llinares, J.-P. Charles, J. Bechara, "Fabrication on tin oxide (SnO_2) thin film by electrostatic spray pyrolysis," Microelectron. Eng. 51–52, 627–631 (2000).

[44] Y. Matsushima, Y. Nemoto, T. Yamazaki, K. Maeda, T. Suzuki, "Fabrication of SnO_2 particle-layer on the glass substrate using electrospray pyrolysis method and the gas sensitivity for H2," Sensors and Actuators B 96, 133–138 (2003).

[45] Y. Higashiyama, S. Tanaka, T. Sugimoto, K. Asano, "Size distribution of the charged droplets in an axisymmetric shower," Journal of Electrostatics 47, 183-195 (1999).

[46] Y. Matsui, M. Mitsuhashi , Y. Goto, “Early stage of tin oxide film growth in chemical vapor deposition,” Surface and Coatings Technology 169, 549-552 (2003).

[47] P. S. Patil, R. K. Kawar, T. Seth, D. P. Amalnerkar and P.S. Chigare, “Effect of substrate temperature on structural, electrical and optical properties of sprayed tin dioxide (SnO_2) thin films,” Ceram. Int. 20, 725–734 (2003).

CHAPTER 3

Opto-chemical sensors based on tin oxide thin films

3.1 An optical model for the proposed sensors

The realized sensors belong to the second class of fibre optic sensors mentioned in the chapter 1. The proposed configuration relies on an extrinsic Fabry–Perót interferometer. The principle of operation of the refractometric chemical sensor is based on the fact that the refractive index discontinuity at the fibre-film interface produces a reflection of the incident power whose intensity strongly depends on the radiation wavelength (λ), on the optical fibre effective refractive index (n_{eff}), on the film refractive index (n_d) and thickness (d), and on the refractive index of the external medium (n_{ext}) (see figure 3.1).

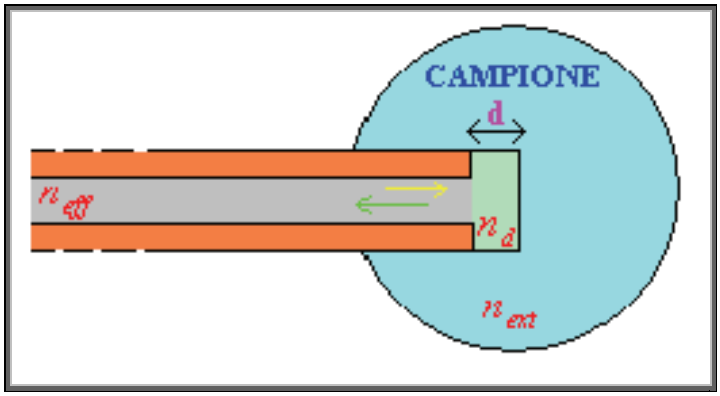

Figure 3.1. Scheme of the proposed opto-chemical sensors.

In order to evaluate the reflected power at the fibre-film interface we will use the so called three layer model [1].

The reflectivity R_{123} can be evaluated as the square modulus of the reflection coefficient which in turn is defined as the ratio between the reflected (E_r) and the incident (E_i) electric field:

$$R_{123} = \left| r_{123} \right|^2 = \left| \frac{E_r}{E_i} \right|^2 \tag{3.1}$$

So we start to evaluate the reflected electric field at the fibre-film interface. In figure 3.2 are illustrated the infinite reflections that occur when radiation, coming from the fibre, encounters first the film and then the external medium in the simplest case of planar and parallel faces.

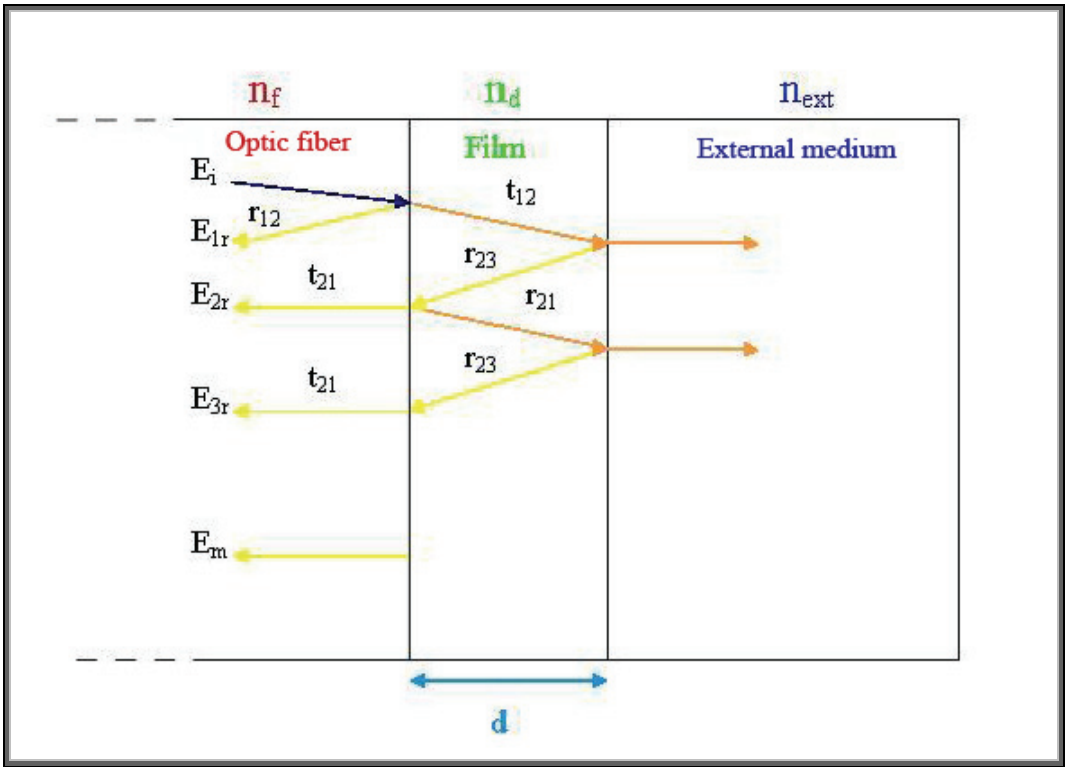

Figure 3.2. Propagation of radiation at the fibre-film interface according to the ray optics and to the parallel and plane faces three layer model.

When a light ray impinges at the fibre-film interface a part is transmitted and a part is reflected and in particular:

- The transmitted one continues to propagate into the film till to encounter the other interface film-external medium. Again at the last interface a part will be reflected and a part will be transmitted.

- The reflected part, while coming back, will encounter the film-fibre interface where it will happen again that a part will be transmitted and a part will be reflected.

The behaviour described above will finish when the ray that propagates forward and backward into the film will be completely extinguished. It follows that the reflected electric field can be determined as the sum of the infinite reflected components, which in turn can be expressed as follows:

$$
\begin{aligned}
&E_{1r} = E_i \cdot r_{12} \\
&E_{2r} = E_i \cdot t_{12} \cdot r_{23} \cdot t_{21} \cdot e^{j\beta} = E_i \cdot (t_{12} \cdot t_{21}) \cdot r_{23} \cdot e^{j\beta} \\
&E_{3r} = E_i \cdot t_{12} \cdot r_{23} \cdot r_{21} \cdot r_{23} \cdot t_{21} \cdot e^{j2\beta} = E_i \cdot (t_{12} \cdot t_{21}) \cdot r_{21} \cdot (r_{23} \cdot e^{j\beta})^2 \\
&E_{4r} = E_i \cdot t_{12} \cdot r_{23} \cdot r_{21} \cdot r_{23} \cdot r_{21} \cdot r_{23} \cdot t_{21} \cdot e^{j3\beta} = E_i \cdot (t_{12} \cdot t_{21}) \cdot r_{21}^2 \cdot (r_{23} \cdot e^{j\beta})^3 \\
&\cdot \\
&\cdot \\
&E_{mr} = E_i \cdot (t_{12} \cdot t_{21}) \cdot r_{21}^{m-2} \cdot (r_{23} \cdot e^{j\beta})^{m-1} = E_i \cdot (t_{12} \cdot t_{21}) \cdot (r_{23} \cdot e^{j\beta}) \cdot (r_{21} \cdot r_{23} \cdot e^{j\beta})^{m-2}
\end{aligned}
\tag{3.2}
$$

Where $e^{j\beta}$ is the delay experienced by the light beam while travelling into the film and β is twice the optical path of the wave into the film:

$$
\beta = 2 \cdot \left[\left(\frac{2 \cdot \pi}{\lambda} \right) \cdot n_d \cdot d \right] = 2 \cdot \delta \tag{3.3}
$$

So the reflected field will be:

$$E_r = E_i \cdot r_{12} + E_i \cdot (t_{12} \cdot t_{21}) \cdot (r_{23} \cdot e^{j\beta}) \cdot \sum_{m=2}^{\infty} (r_{21} \cdot r_{23} \cdot e^{j\beta})^{m-2} =$$

$$= E_i \cdot \left[r_{12} + \frac{(t_{12} \cdot t_{21}) \cdot r_{23} \cdot e^{j\beta}}{1 - r_{21} \cdot r_{23} \cdot e^{j\beta}} \right] \tag{3.4}$$

Where:

- r_{ik} represents the reflection coefficient between the media i and k:

$$r_{ik} = \frac{n_i - n_k}{n_i + n_k}$$

- t_{ik} represents the transmission coefficient between the media i and k:

$$t_{ik} = \frac{2 \cdot n_i}{n_i + n_k}$$

Therefore it is possible to obtain the reflectivity R_{ik} and the transmittivity T_{ik} between the media i and k:

$$R_{ik} = r_{ik} \cdot r_{ki} = -\left(\frac{n_i - n_k}{n_i + n_k} \right)^2 \qquad T_{ik} = t_{ik} \cdot t_{ki} = \frac{4 \cdot n_i \cdot n_k}{(n_i + n_k)^2} \tag{3.5}$$

By dividing the reflected field with the incident one we will obtain the reflection coefficient:

$$r_{123} = \frac{E_r}{E_i} = r_{12} + \frac{(t_{12} \cdot t_{21}) \cdot r_{23} \cdot e^{j\beta}}{1 - r_{21} \cdot r_{23} \cdot e^{j\beta}} = \frac{r_{12} - r_{12} \cdot r_{21} \cdot r_{23} \cdot e^{j\beta} + r_{23} \cdot (t_{12} \cdot t_{21}) \cdot e^{j\beta}}{1 - r_{21} * r_{23} * e^{j\beta}} =$$

$$= \frac{r_{12} + r_{23} \cdot e^{j\beta} \cdot (t_{12} \cdot t_{21} - r_{12} \cdot r_{21})}{1 - r_{21} \cdot r_{23} \cdot e^{j\beta}} = \frac{r_{12} + r_{23} \cdot e^{j\beta} \cdot (T_{12} + R_{12})}{1 - r_{21} \cdot r_{23} \cdot e^{j\beta}} = \tag{3.6}$$

$$= \frac{r_{12} + r_{23} \cdot e^{j\beta}}{1 - r_{21} \cdot r_{23} \cdot e^{j\beta}}$$

At this point it is possible to obtain the reflectivity:

$$R_{123} = \left| r_{123} \right|^2 = r_{123} \cdot r_{123}^* = \frac{r_{12} + r_{23} \cdot e^{j\beta}}{1 - r_{21} \cdot r_{23} \cdot e^{j\beta}} \cdot \left(\frac{r_{12} + r_{23} \cdot e^{j\beta}}{1 - r_{21} \cdot r_{23} \cdot e^{j\beta}} \right)^* =$$
$$= \frac{r_{12} + r_{23} \cdot e^{j\beta}}{1 - r_{21} \cdot r_{23} \cdot e^{j\beta}} \cdot \frac{r_{12}^* + r_{23}^* \cdot e^{-j\beta^*}}{1 - r_{12}^* \cdot r_{23}^* \cdot e^{-j\beta^*}} = \tag{3.7}$$
$$= \frac{r_{12}^2 + r_{23}^2 \cdot e^{j(\beta - \beta^*)} + r_{12}^* \cdot r_{23} \cdot e^{j\beta} + r_{12} \cdot r_{23}^* \cdot e^{-j\beta^*}}{1 + r_{12}^2 \cdot r_{23}^2 \cdot e^{j(\beta - \beta^*)} + r_{12} \cdot r_{23} \cdot e^{j\beta} + r_{12}^* \cdot r_{23}^* \cdot e^{-j\beta^*}}$$

The refractive index n_d has to be assumed real because the sensitive film exploited in this work is transparent in the considered wavelength range. As a matter of the fact, studies carried out in the past about the optical properties of tin dioxide showed that absorption region of SnO_2 films lies in the wavelength range as low as 250 – 300 nm, while in the VIS and NIR wavelength range it results to be transparent [2].

Now, as a consequence also the reflection coefficients are real; this means that:

$$\begin{aligned} r_{ik} &= r_{ik}^* \\ \beta &= \beta^* \end{aligned} \tag{3.8}$$

In conclusion, the reflectivity of transparent media is:

$$R_{123} = \frac{r_{12}^2 + r_{23}^2 + r_{12} \cdot r_{23} \cdot \left(e^{j\beta} + e^{-j\beta^*} \right)}{1 + r_{12}^2 \cdot r_{23}^2 + r_{12} \cdot r_{23} \cdot \left(e^{j\beta} + e^{-j\beta^*} \right)} = \frac{r_{12}^2 + r_{23}^2 + 2 \cdot r_{12} \cdot r_{23} \cdot \cos(\beta)}{1 + r_{12}^2 \cdot r_{23}^2 + 2 \cdot r_{12} \cdot r_{23} \cdot \cos(\beta)} =$$
$$= \frac{r_{12}^2 + r_{23}^2 + 2 \cdot r_{12} \cdot r_{23} \cdot \left(1 - 2 \cdot \sin^2(\delta) \right)}{1 + r_{12}^2 \cdot r_{23}^2 + 2 \cdot r_{12} \cdot r_{23} \cdot \left(1 - 2 \cdot \sin^2(\delta) \right)} = \frac{r_{12}^2 + r_{23}^2 + 2 \cdot r_{12} \cdot r_{23} - 4 \cdot r_{12} \cdot r_{23} \cdot \sin^2(\delta)}{1 + r_{12}^2 \cdot r_{23}^2 + 2 \cdot r_{12} \cdot r_{23} - 4 \cdot r_{12} \cdot r_{23} \cdot \sin^2(\delta)} = \tag{3.9}$$
$$= \frac{(r_{12} + r_{23})^2 - 4 \cdot r_{12} \cdot r_{23} \cdot \sin^2(\delta)}{(1 + r_{12} \cdot r_{23})^2 - 4 \cdot r_{12} \cdot r_{23} \cdot \sin^2(\delta)}$$

As said before the reflectivity is a function of several parameters:

$$R_{123} = f\left(\lambda, n_{eff}, n_d, d, n_{ext} \right) \tag{3.10}$$

Assuming that the radiation source is so stable that the wavelength variation are negligible, it is possible to write the reflectivity differential as follows:

$$\Delta R_{123} = \left(\frac{\partial R_{123}}{\partial n_d} \right) \cdot \Delta n_d + \left(\frac{\partial R_{123}}{\partial d} \right) \cdot \Delta d + \left(\frac{\partial R_{123}}{\partial n_{ext}} \right) \cdot \Delta n_{ext}$$

$$\Rightarrow \Delta R_{123} = S_{n_d} \cdot \Delta n_d + S_d \cdot \Delta d + S_{n_{ext}} \cdot \Delta n_{ext} \tag{3.11}$$

Where S_{n_d}, S_d and S_{next} are the sensitivity to the film refractive index, the sensitivity to the film thickness and the sensitivity to the external medium refractive index respectively.

In the proposed sensor configuration, any effect able to modify the refractive index or the thickness of the sensing layer, or also the refractive index of the external medium would modify the fibre-film interface reflectance R_{123}, and thus the power level coming back from the fibre end [3].

Nevertheless, the change in the fibre-film reflectance caused by changes of the external medium refractive index and of the sensitive layer thickness, can be assumed to be not relevant with respect to the whole sensor response because of the very low analyte concentrations considered all over this work. For this reason when the target analyte is injected in the test ambient, the interaction between its molecules and the sensitive material leads to a reflectance change at the fibre-film interface and thus in the sensor output that can be attributed only to a significant changes in the sensitive film refractive index.

3.2 Samples preparation

The first attempts to prepare SnO_2 layers using the ESP were carried out by Zaouk et al. [4, 5] and Gourari et al. [6]. Although conductive substrates were conventionally used in ESP, Zaouk et al. [4, 5] revealed the availability of ESP for the insulator substrate. ESP method has been almost always used for the deposition of metal oxide (MOX) coatings on planar substrates [7-9].

In this work, SnO_2 thin films have been deposited upon the distal end of a standard single mode optical fibre for telecommunication (SMF-28) by means of an optimization and customization of the standard ESP deposition technique.

The SMF-28 have an outer diameter of 125 µm and 9.0 µm core diameter, see figure 3.3. The core-cladding structure is then covered by several protective coatings in order to give it resistance and flexibility (in figure 3.3 is reported only the inner coating).

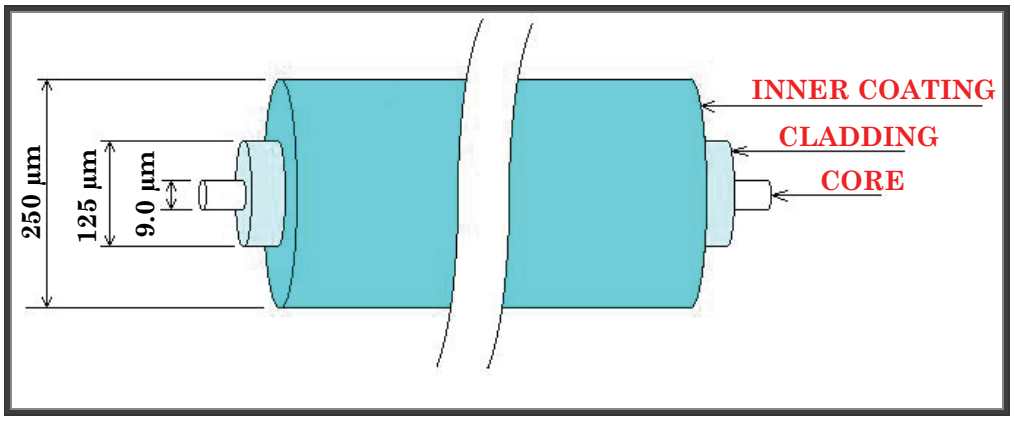

Figure 3.3. Schematic structure of a standard single mode optic fibre (SMF-28).

These fibres have been prepared by stripping the protective coatings a few centimeters from the fibre end. The bare fibre has been washed in chloroform in order to remove any coating residuals. Then the fibre end has been properly cut by using a precision cleaver in order to obtain a planar

cross-section, where the SnO_2 films have been deposited. A SEM (scanning electron microscope) image of the transverse section of a properly cut fibre is shown in figure 3.4.

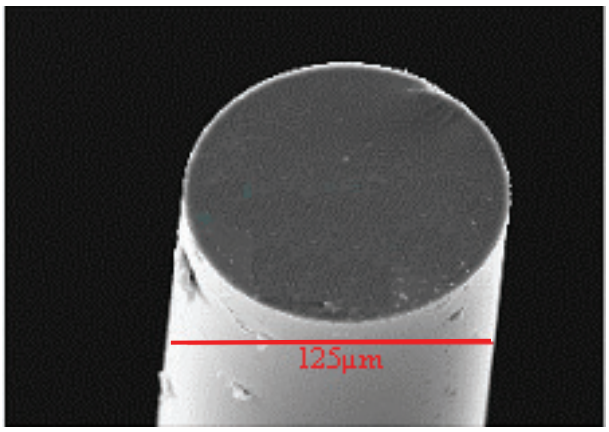

Figure 3.4 SEM image of a single mode optic fibre transverse section before the SnO_2 layer deposition.

The deposition set-up used for sensors fabrication is shown in figure 3.5. It consists of a high voltage source (FUG, 0-30kV), two syringes connected with a flexible pipe for the solution handling, a needle with an external diameter of 0,5 mm, connected with a high voltage source (17 ± 0.1 kV) in order to create a high electric field between the needle itself and a grounded metal substrate where the fibre end is located. The necessary temperature has been reached by means of a resistive heater, in contact with the substrate, constituted by two stainless steel plates of a few square centimeters and by a nichrome wire connected with a 300W voltage source. The heater was supplied with a chromium-nickel thermocouple connected with a multimeter for the temperature monitoring. The distance between the needle and the optical fibre end was about 30 mm. The deposition has been performed at a constant temperature of 320±5 °C. Liquid flow has been regulated by means of an air pump connected with the first syringe and kept

constant to 0,37 ml/min. Tin dioxide films grew according to the following reaction [10]:

$$SnCl_4 + 2H_2O \rightarrow SnO_2 + 4HCl$$

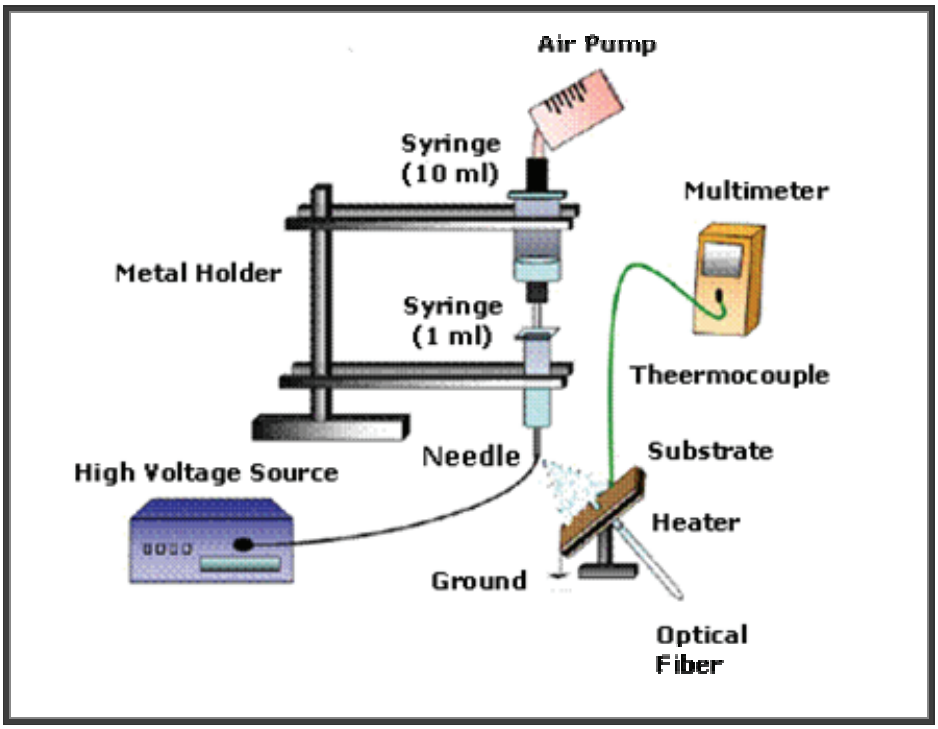

Figure 3.5 Schematic drawing of the ESP apparatus.

The SnO_2 films fabrication has been performed by means of a constant volume (5 ml) of an ethanol solution of $SnCl_4 \cdot 5H_2O$ but with different concentrations (0.01 and 0.001, mol/l). The deposited layers were labeled as reported in the table 3.1.

During the deposition, it is also possible the formation of amorphous SnO phase. Thermal treatment is one of the ways to transform SnO_x to SnO_2 and clean the films surface from the other dopants like water or alcohol present in the initial solution [19]. For this reason, after the deposition procedure and after the morphological and optical characterization, the prepared samples have been annealed at 500±5°C for 1 hour. The temperature has been increased from room temperature to 500°C with a constant rate of

5°C/min and, after the annealing procedure, the temperature has been decreased with the same rate down to the room temperature.

Concentration [mol/l]	**0.01**	**0.001**
	P2 **S4** **S5** **S6new** **S7** **S9**	**S11** **S11new** **S12** **S15** **S17** **S18**

Table 3.1. Prepared samples analyzed in the present work.

References

[1] H. A. Macleod, Thin-Film Optical Filters, 3rd ed. Bristol, U.K.: Inst. Phys., (2001).

[2] S. G. Ansary, S. W. Gosavi, S. A. Gangal, R. N. Karekar, and R. C. Aiyer, "Characterization of SnO_2-based H2 gas sensors fabricated by different deposition techniques," J. Mater. Sci., Mater. Electron. 8, 23–27 (1997).

[3] M. Penza, G. Cassano, P. Aversa, F. Antolini, A. Cusano, M. Consales, M. Giordano, and L. Nicolais, "Carbon nanotubes coated multitransducing sensors for VOCs detection," Sens. Actuators B, Chem. 111/112, 171–180 (2005).

[4] D. Zaouk, Y. Zaatar, A. Khoury, C. Llinares, J.-P. Charles, J. Bechara, "Electrical and optical properties of pyrolytically electrostatic sprayed fluorine-doped tin-oxide: dependence on substrate-temperature and substrate-nozzle distance," J. Appl. Phys. 87, 7539–7543 (2000).

[5] D. Zaouk, Y. Zaatar, A. Khoury, C. Llinares, J.-P. Charles, J. Bechara, "Fabrication on tin oxide (SnO_2) thin film by electrostatic spray pyrolysis," Microelectron. Eng. 51–52, 627–631 (2000).

[6] H. Gourari, M. Lumbreras, R.V. Landschoot, J. Schoonman, "Elaboration and characterization of SnO_2–Mn2O3 thin layers prepared by electrostatic spray deposition," Sens. Actuators B 47, 189–193 (1998).

[7] H. Gourari, M. Lumbreras, R. Van Landschoot, J. Schoonman, "Electrode nature effects on stannic oxide type layers prepared by electrostatic spray deposition", Sens. Act. B 58, 365–369 (1999).

[8] Y. Matsushima, Y. Nemoto, T. Yamazaki, "Fabrication of SnO_2 particle-layer on the glass substrate using electrospray pyrolysis method and the gas sensitivity for H2," Sens. Act. B 96, 133-138 (2003).

[9] E. H. A. Diagne, M. Lumberas, "Elaboration and characterization of tin oxide-lanthanum oxide mixed layers prepared by the electrostatic spray pyrolysis technique," Sens. Act. B 78, 98-105 (2001).

[10] Y. Matsui, M. Mitsuhashi , Y. Goto, "Early stage of tin oxide film growth in chemical vapor deposition," Surface and Coatings Technology 169, 549-552 (2003).

[11] R. Ramamoorthy, M. K. Kennedy, H. Nienhaus, A. Lorke, F. E. Kruis, and H. Fissan, “Surface oxidation of monodisperse SnOx nanoparticles,” Sens. Act. B 88, 281–285 (2003).

CHAPTER 4

Scanning probe microscopy: principles of operation

4.1 The scanning probe microscopy

Traditional optical microscopy, although it remains one of the most widespread imaging techniques due to its non destructive, non invasive, inexpensive, easy to implement characteristics, has a fundamental limitation in the spatial resolution to half the wavelength of light. In order to obtain an image of sub-micron or smaller features, the shorter wavelength is required to produce an interference pattern. This problem was overcome when G. Binnig and his colleagues in 1981 at the IBM Zurich Research Laboratory (Switzerland) developed the Scanning Tunneling Microscope (STM) to produce an atomic-scale image of a metallic silicon surface [1]. The atomic resolution is achievable because instead of constructing a microscope with the principle of the interference waves of matters (lights, electrons, etc), this interaction type microscopy maps the strength of the electronic interaction between the topmost layer of the specimen with an atom sized probe tip in terms of quantifying electron tunneling [1]. Binnig and Rohrer received a Nobel Prize in Physics in 1986 for their discovery. STM can only be used to study surfaces which are electrically conductive to some degree. Based on their design, in 1985, Binnig et al. developed an Atomic Force Microscope (AFM) to measure ultrasmall forces (less than 1 μN) present between the AFM tip and the sample surface [2]. AFM can be used for measurement of all engineering surfaces which may be either electrically conductive or insulating. The AFM has become a popular surface profiler for topographic and normal force measurements on the micro to nanoscale. AFM modified in order to measure both normal and lateral forces is called Lateral Force Microscope (LFM) or

Friction Force Microscope (FFM). AFM can be used in any environment such as ambient air [3-4], various gases [5], liquid [6-7], vacuum [8], at low temperatures (lower than about 100 K) [9-10] and high temperatures [11]. Imaging in liquid allows the study of live biological samples and it also eliminates water capillary forces present in ambient air at the tip'sample interface. Low temperature imaging is useful for the study of biological and organic materials and the study of low-temperature phenomena such as superconductivity or charge-density waves. Low temperature operation is also advantageous for high sensitivity force mapping due to the reduction in thermal vibration. Since the introduction of the STM and AFM, many variations of probe based microscopies, referred to as scanning probe microscopies SPMs, have been developed. While the pure imaging capabilities of SPM technique is dominated by the application of these methods as their early development stages, the physics of probe-sample interactions and the quantitative analyses of tribological, electronic, magnetic, biological and chemical surfaces have now become of increasing interest. Nanoscale science and technology are strongly driven by SPMs which allow investigation and manipulation of surfaces down to the atomic scale. With growing understanding of the underlying interaction mechanism, SPMs have found applications in many fields outside basic research fields. In addition, various derivatives of all these methods have been developed for special applications, some of them targeted far beyond microscopy.

The SPMs family includes Scanning Near Field Optical Microscope (SNOM). The advent of a near field scanning optical microscope was a natural procedure to construct an interaction-type microscope using light or photons as a substitute for electrons. In analogy to the STM, the strength of local electromagnetic interaction between a sample and an optical probe tip is mapped to produce a nanometer-scale image which lies far beyond the diffraction limit ($\lambda/2$). In fact until the development of SNOM this dimension was thought to represent the resolution limit for optical microscopy. SNOM overcomes the diffraction limit by confining light via a tiny aperture (typically 10 - 200 nm) which can be raster scanned over a sample surface to

construct an image point by point. Light emanating from this aperture rapidly diffracts, but for a small distance (about one aperture diameter) away from the aperture the spatial extent of the light is defined by the aperture. Thus, as long as the distance between the sample surface and the aperture is maintained at a small fraction of the aperture size, the resolution of the image will be determined by the size of the aperture and not the wavelength of light, as sketched in figure 4.1.

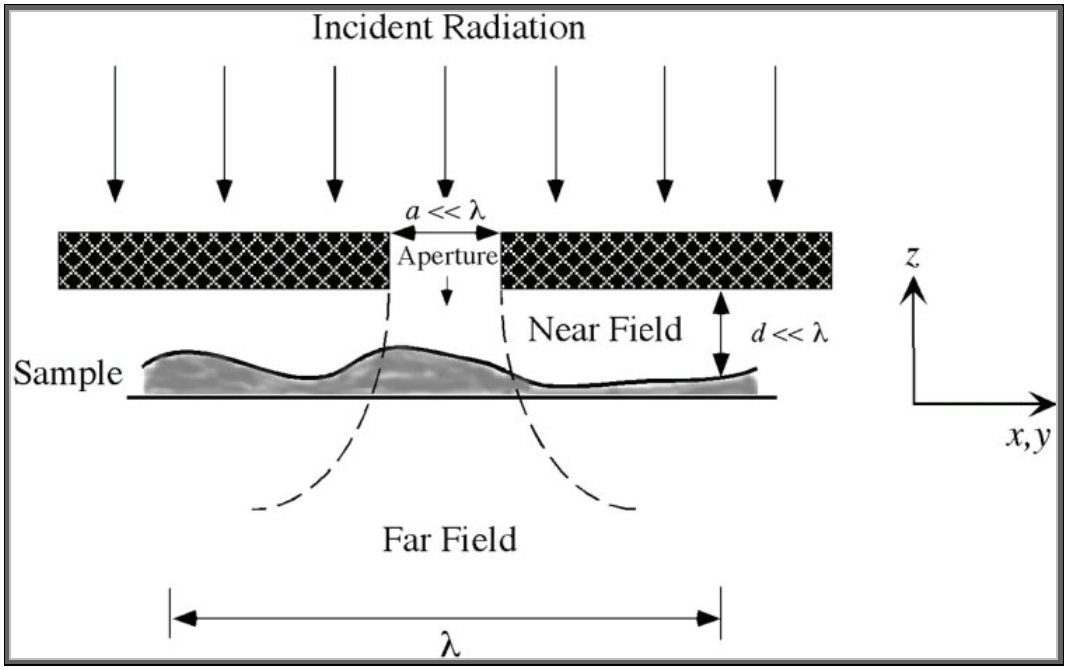

Figure 4.1. A sketch showing the basic principles of sub-wavelength resolution in near-field optics. The two critical requirements are: (1) a sub-wavelength light source (aperture in the illustration), and (2) placing the sample in the near field zone of the light source.

This idea was first proposed by E.H. Synge in 1928 [12]. In this paper, he also pointed out the two major obstacles that would prevent the realization of a visible light SNOM for another 60 years. They are: (1) the difficulty in making a subwavelength size light source that is bright enough and (2) the difficulty in bringing a sample to the near-field zone of such a light source due to the surface roughness of usual materials. These problems were not solved until the invention of scanning probe techniques in 1980s. However,

as early as 1972, the ability of near-field imaging to produce sub-diffraction limit resolution was demonstrated in microwaves, where a resolution of λ/60 was achieved with 3 cm wavelength electromagnetic waves [13, 14]. The first SNOM working at optical frequency was developed in 1984 by two independent groups [15, 16]. Lewis et al. described for the first time the possibility of constructing a scanning near field optical microscope based on a metal-coated probe with a 30 nm aperture [15]. Pohl et al. demonstrated that details of 25 nm sized fine-line structures could be imaged by passing an extremely narrow aperture along a test object [16].

The first major breakthrough in SNOM technology was obtained in 1991 by Betzig *et al.* [l7] with the introduction of a new reliable near-field source, consisting in a tapered optical fibre, metallized in the terminal part in such a way that a subwavelength aperture is left at the edge, having a diameter of a few tens of nm. In the original design this aperture was used to illuminate the sample and a resolution of 12 nm was claimed, in addition to a relevant signal strength. The definitive momentum leading to the success of SNOM was given by the development of a method to control the probe-sample distance, which permitted a simultaneous recover of the surface topography in addition to the optical properties. This method [l8, l9] was based on the detection of the lateral forces (shear-forces) which act between the laterally vibrating fibre probe and the sample when the relative distance is about 10nm.

A further progress in high resolution optical microscopy was obtained with the invention of the so-called apertureless SNOM [20-22]. In this configuration the subwavelength illuminating source is reduced to extreme limits, with a few dipoles located at the apex of a very sharp AFM or STM probe. When these dipoles are irradiated by an external light source they act as scattering centers, generating strong near-field components used to probe the surface. An excellent resolution of 3 nm was achieved in the first experiments, which has been pushed up to 0.8 nm in luminescence experiments [23].

Different contrast mechanisms in SNOM have been pointed out based on the refractive index, birefringent properties [24], polarization [25], or just on

the geometry of the sample. First luminescence experiments were performed on dye spheres [24] and on fluorescent molecules [26], while a new field was developed with the application of the SNOM to the investigation of the luminescence properties of low dimensional semiconductor heterostructures [27, 28] under low temperature conditions [29].

Nowadays the SNOM has been established as a unique tool in different research fields: single molecule spectroscopy [30, 31], high spatial resolution Raman spectroscopy [32] [33], nanolithography [34, 35], semiconductor heterostructures spectroscopy [36-38], ultrafast [39, 40] and coherent [41] spectroscopy on the nanoscale, applications to biological specimens [42, 43] and photonic-bandgap materials [44, 45].

4.2 The Atomic Force Microscopy

A typical AFM system consists of a micro-machined cantilever probe and a sharp tip mounted to a Piezoelectric (PZT) actuator and a position sensitive photo detector for receiving a laser beam reflected off the end-point of the beam to provide cantilever deflection feedback, as depicted in figure 4.2. For a detailed review see for example ref. [46].

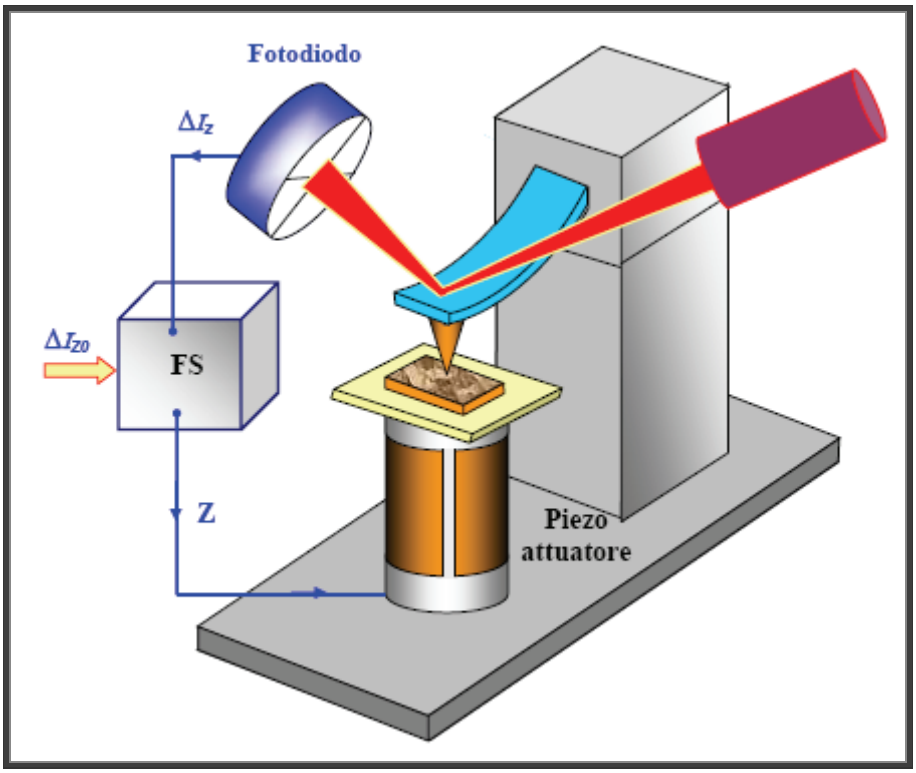

Figure 4.2. Schematic of basic AFM operation.

When using a feedback loop to keep a constant interaction between the tip and the sample, an error signal, additionally to the topography signal, will be recorded. This error signal translates the ability of the closed loop system to keep a constant force on the sample. The feedback loop is in most cases regulated by a PID (Proportional Integral and Differential) controller where the proportional, integral and differential factors of the system can be adjusted. Two different techniques can be distinguished to sense the

topography: static and dynamic. Both rely on the modification of the cantilever position due to influence of the surface proximity.

4.2.1 Static mode

The principle of AFM operation is to scan the tip over the sample surface with feedback mechanisms that enable the PZT scanners to maintain the tip at a constant force, or constant height above the sample surface. As the tip scans the surface of the sample, moving up and down with the contour of the surface, the laser beam deflected from the cantilever provides measurements of the difference in light intensities between the upper and lower photo detectors. Feedback from the photodiode difference signal, through software control from the computer, enables the tip to maintain either a constant force or constant height above the sample. A schematic diagram of these AFM operation is reported in figure 4.3. In the constant force mode, the PZT transducer monitors real time height deviation. In the constant height mode, the deflection force on the sample is recorded. The topographic image of the samples is taken from the sample Z-position data [47] .

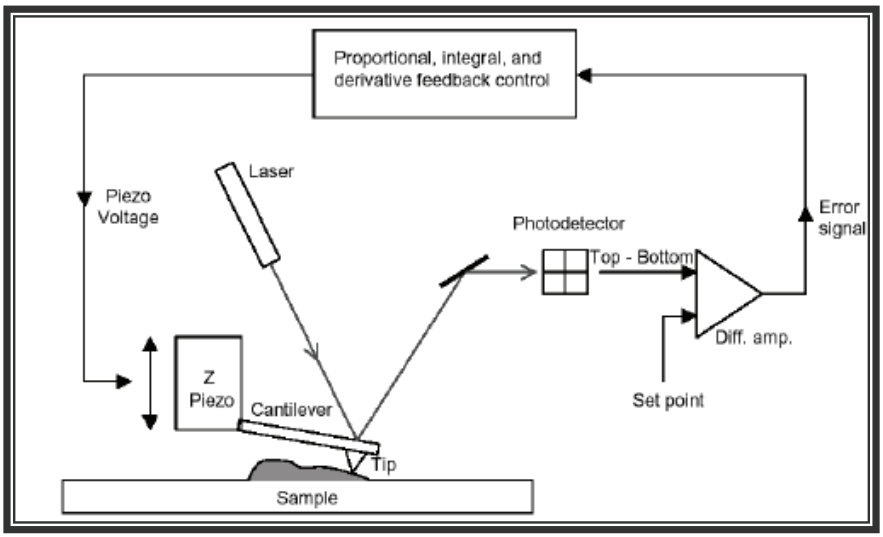

Figure 4.3. Schematic diagram of static AFM operation (contact mode).

The mode described is called contact mode or repulsive mode because the tip is deflected by the sample due to repulsive Coulomb forces (See figure 4.4). It is generally only used for flat samples that can withstand lateral forces during scanning.

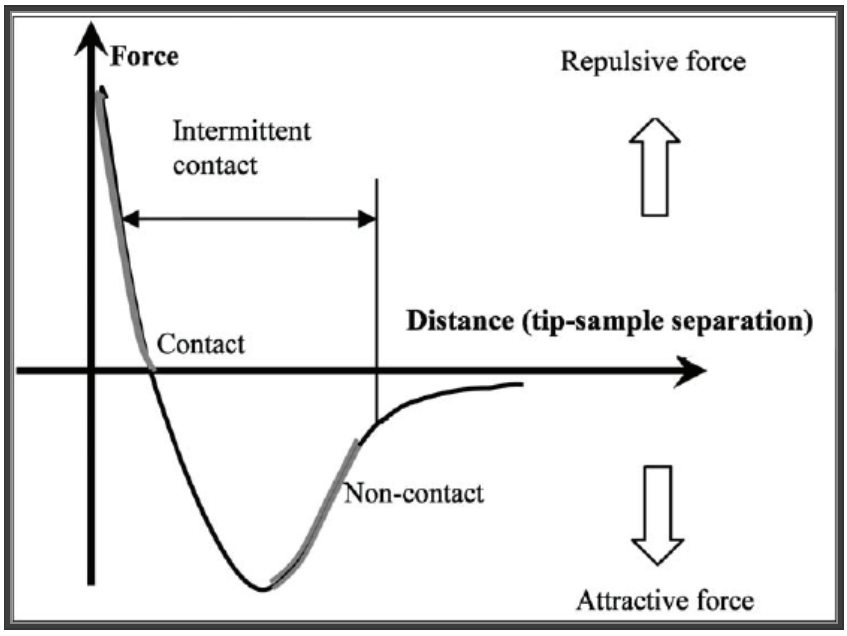

Figure 4.4. Interatomic force variation versus distance between AFM tip and sample.

4.2.2 Dynamic mode

In the dynamic modes (figures 4.5), the cantilever is deliberately vibrated. In particular, the cantilever is driven into periodic (AC) oscillation near its resonant frequency (tens to hundreds of kHz) with amplitudes of 5 to 100 nm. There are two basic methods of dynamic operation: amplitude modulation (AM also known as tapping mode) and frequency modulation (FM also known as non contact mode) operation. In AM-FM the actuator is driven by a fixed amplitude A_{drive} at a fixed f_{drive}, where f_{drive} is chosen close to a natural frequency f_0 of the probe. When the tip approaches the sample, elastic and inelastic interaction cause change in both the amplitude and the phase (relative to the driving signal) of the cantilever. The oscillation amplitude is used as a feedback parameter to measure the topography of the

sample surface. Additionally, material properties variations could be mapped by recording the phase shift between the driving force and the tip oscillation. On the other hand, in frequency modulation the cantilever is kept oscillating with a fixed amplitude at its resonance frequency. This resonance frequency depends on the forces acting between tip and sample surface. The spatial dependence of the frequency shift, the difference between the actual resonance frequency and that of the free lever, is the source of contrast. An image is formed by profiling the surface topography with a constant frequency shift [48].

The two dynamic modes differ only in the nature of the interaction as reported in figure 4.4. In AM-AFM mode, the tip contacts the sample on each cycle, so the amplitude is reduced by ionic repulsion as in contact mode. In FM-AFM long range Van der Waals forces reduce the amplitude by effectively shifting the spring constant experienced by the tip and changing its resonant frequency.

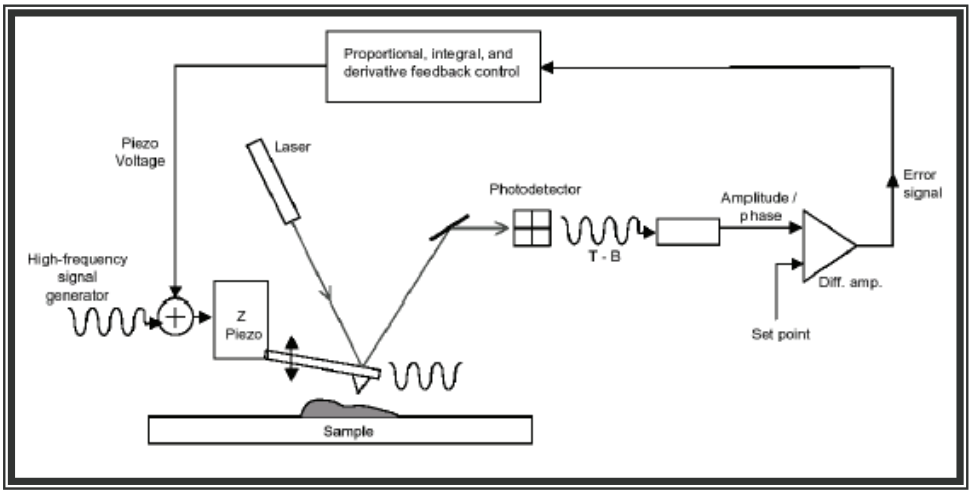

Figure 4.5. Schematic diagram of static AFM operation (non contact mode).

The interest and sophistication of dynamic AFM modes stems on four factors: (i) routine nanometer-scale spatial resolution of semiconductors, polymers and biomolecules and atomic resolution images of insulator surface in ultra high vacuum (UHV); (ii) the existence of several parameters

sensitive to the tip-sample interactions (amplitude, phase shift and cantilever deflection); (iii) the challenging features of the motion of a vibrating tip interaction with a surface and (iv) the potential to develop quantitative method to characterise material properties at nanometer scale.
In particular, AM-AFM offers a powerful method for mapping simultaneously topography and variations in the composition, friction, viscoelasticity and adhesion of the sample surface. This method was been called phase-contrast imaging or simply phase imaging [48].

4.2.3 Resolution in an atomic force microscope

Traditional microscopes have only one measure of resolution; the resolution in the plane of an image. An atomic force microscope has two measures of resolution; the plane of the measurement and in the direction perpendicular to the surface.
The in-plane resolution depends on the geometry of the probe that is used for scanning. In general, the sharper the probe is the higher the resolution of the AFM image (for atomic flat sample it is limited by diameter of atom at the probe tip, while for rough surface it is limited by the tip "end radius"). In the figure 4.6 below is the theoretical line scan of two spheres that are measured with a sharp probe and a dull probe.

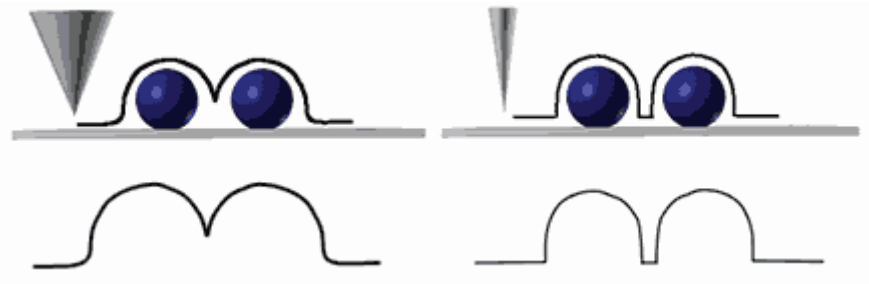

Figure 4.6. The image on the right will have a higher resolution because the probe used for the measurement is much sharper.

The vertical resolution in an AFM is limited only by electronic noise and by the mechanical vibrations of the probe above the surface. Sources for

vibrations are acoustic noise, floor vibrations, and thermal vibrations. Getting the maximum vertical resolution requires minimizing the vibrations of the instrument. For this reason it is important to reduce as much as possible the influence of external vibrations by means of vibration-insulating systems.

4.3.4 Protection against vibrations

Any scanning probe microscope is an oscillatory system with its own resonant frequency ω_0. External mechanical vibrations with frequencies coinciding with may excite resonance in the measuring heads structure, which results in fluctuations of the tip relatively to the sample that is perceived as a parasitic periodic noise deforming and dithering the SPM images of samples surface. To reduce the influence of external vibrations the measuring heads are made of massive metal details with high (more than 100 kHz) resonant frequencies. Scanners have low resonant frequencies. In the design of modern SPM it is necessary to reach a compromise between the scanner range (the size of maximum scanned area) and its resonant frequency. Typical values for resonant frequencies are in the range 10 - 100 kHz. The simplest vibration-insulating system is the passive one. The basic idea incorporated in passive vibration-insulating systems is the following. The amplitude of forced oscillations of a mechanical system quickly decays at large values of the difference between the excitation frequency and own resonant frequency of the system ω_K (see figure 4.7). Therefore external vibrations with frequencies $\omega_{EXT} >> \omega_K$ practically do not affect the oscillatory system. Hence, if the measuring head of a probe microscope is placed on a vibration-insulating platform or on an elastic suspension, then only external fluctuations with frequencies close to the resonant frequency of the vibration-insulating system will be picked-up by the microscope. Since the resonant frequencies of SPM heads are in the range 10 - 100 kHz, choosing the resonant frequency of vibration-insulating systems low enough (about 5 - 10 Hz), it is possible to protect the device from external vibrations rather effectively. In order to quench oscillations even at their own resonant frequencies, dissipative elements with viscous friction are introduced into

vibration insulating systems. Thus, to reach effective protection it is necessary to make the resonant frequency of the vibration insulating system as small as possible.

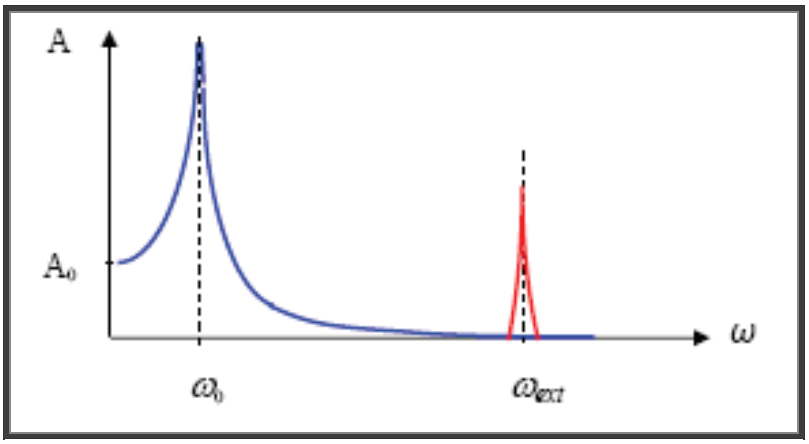

Figure 4.7. Blue color: SPM resonant curve Red color : frequency spectrum of external vibrations.

4.2.4 AFM probes

Surface sensing in the atomic force microscope is performed using special probes made of an elastic cantilever with a sharp tip on the end, also called standard probes. Such probes are produced by photolithography and etching of silicon, SiO_2 or Si_3N_4 layer deposited onto a silicon wafer [49]. One end of the cantilever is firmly fixed on the silicon base, the holder, and the tip is located on the free cantilever end. Figure 4.8 reports SEM images of common AFM tips. The curvature radius of AFM tip apex is of the order of 1-50 nanometers depending on the type and the technology of manufacturing. The angle near the tip apex is 10-20 degree.

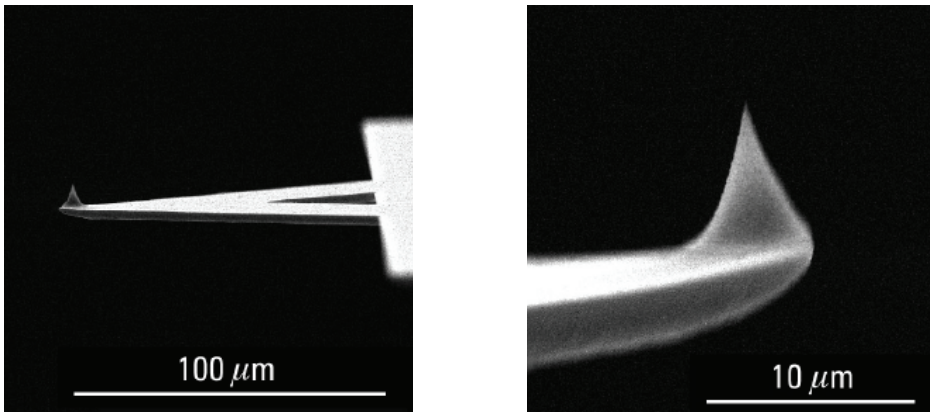

Figure 4.8. SEM images of common SiO2 AFM tips.

Another type of AFM probes are cantilevered pulled optical fibre probes, see figure 4.9.

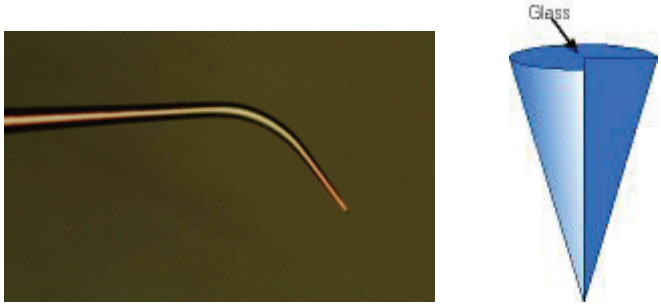

Figure 4.9. Cantilevered optical fibre AFM probe.

The interaction force F of a tip with the surface can be estimated from the Hooke law: $F=k\,\Delta z$ where k is the cantilever elastic constant, Δz is the tip displacement corresponding to the bending produced by the interaction with the surface. The k values vary in the range 10 -3 ÷ 10 10N/m depending on the cantilever material and geometry. The cantilever resonant frequency is important during AFM operation in dynamic modes. Natural frequencies of cantilever are determined by the following formula (see for example ref. [50]):

$$\omega_{ri} = \frac{\lambda_i}{l^2}\sqrt{\frac{E\,J}{\rho\,S}}$$

Where l is the cantilever length; E the Young's modulus; J the inertia moment of the cantilever cross-section; ρ the material density; S the cross section; λi a numerical coefficient (in the range 1 ÷100), depending on the oscillation mode. Frequency main modes are usually in the 10 ÷1000 kHz range.

The key component in an AFM is the sensor for measuring the force on the tip due to its interaction with the sample. A cantilever (with a sharp tip) with extremely low spring constant is required for high vertical and lateral resolutions at small forces (0.1 nN or lower) but at the same time a high resonant frequency is desirable (about 10 to 100 kHz) in order to minimize the sensitivity to vibration noise from the building which is near 100 Hz. This require a spring with extremely low vertical spring constant (typically 0.05 to 1 N/m) as well as low mass (on the order of 1 ng). In fact to obtain atomic resolution with AFM, the spring constant of the cantilever should be weaker than the equivalent spring between atoms. For example, the vibration frequency ω of atoms bound in a molecule or in a crystalline solid are typically $10E^{(13)}$ Hz or higher. Combining this with the mass of the atom, on the order of $10E^{(-25)}$ kg, gives an interatomic spring constant k on the order of 10 N/m [51]. Therefore, a cantilever beam with a spring constant of about 1N/m or lower is desirable.

4.3 The scanning near field optical microscopy

The theoretical interpretation of the SNOM basic principles can be afforded in the framework of the propagation-scattering theory of electromagnetic waves. The difference with conventional optics concerns the fact that in our case both the light sources and the scattering structures have sub-wavelength dimensions, therefore methods involving the constant phase approximation or the definition of a point spread function (PSF) based on the Fraunhofer approximation can no longer be applied. The exact solution of the Maxwell equations is needed with proper boundary conditions on the scattering surface, leading to both the generation and the detection of evanescent waves, which play a key role in achieving sub-wavelength spatial resolution.

In this paragraph we want to illustrate how the diffraction phenomenon naturally arises in the propagation of light and how it is possible to achieve sub-wavelength lateral resolution by exploiting the evanescent components of the electromagnetic field. Then the key concepts of far field and near field will be introduced.

For more detailed descriptions of the theoretical aspects related to SNOM technique we remand to proper references.

4.3.1 Propagation, diffraction and evanescent waves

The solution of a general diffraction problem consists in calculating the field at the point (x, y, z) once we know the field on the plane z = 0, as well as its behaviour at an infinite distance from that plane. Actually this is a propagation problem which, in the framework of the Maxwell equations, will lead to the diffraction phenomenon as a manifestation of the wave nature of the electromagnetic field.

Let us assume [52] a monochromatic wave having frequency ω which travels in the z < 0 half-space. Moreover let us assume to know the exact form of the electric field $\vec{E}$ in the plane z = 0 and that the electromagnetic wave travels in vacuum. What we are looking for is the explicit form $\vec{E}$ (x , y, z) in the z > 0 half-space. For the sake of simplicity we will consider the scalar amplitude E of the field reminding that its vectorial nature can be taken into account

just considering E as one of the Cartesian components. Assuming a harmonic temporal dependence, the scalar field verifies the Helmholtz equation:

$$\frac{\omega^2}{c^2}E(\vec{r})+\nabla^2 E(\vec{r})=0 \tag{4.1}$$

If we consider the field E(x, y, z) as a function of x and y on the plane z = const., we can introduce the Fourier transform $\widetilde{E}$ along the xy plane such as

$$E(x,y,z)=\int_{-\infty}^{+\infty}\int_{-\infty}^{+\infty}\widetilde{E}(\alpha,\beta,z)e^{i(\alpha x+\beta y)}d\alpha\, d\beta \tag{4.2}$$

The problem of finding the expression of E(x, y, z) is then led back to the determination of its Fourier transform $\widetilde{E}$ (α, β, z) which can be done by using the Helmholtz equation (4.1). We then find

$$\frac{\partial^2\tilde{E}}{\partial z^2}+\left(\frac{\omega^2}{c^2}-\alpha^2-\beta^2\right)\tilde{E}=0 \tag{4.3}$$

The general solution can be written as the sum of two exponential functions

$$\widetilde{E}(\alpha,\beta,z)=A(\alpha,\beta)e^{i\gamma z}+B(\alpha,\beta)e^{-i\gamma z} \tag{4.4}$$

Where we have indicated:

$$\begin{cases}\gamma(\alpha,\beta)=\sqrt{\dfrac{\omega^2}{c^2}-\alpha^2-\beta^2} & \text{For } \alpha^2+\beta^2<\dfrac{\omega^2}{c^2}\\ \gamma(\alpha,\beta)=i\sqrt{\alpha^2+\beta^2-\dfrac{\omega^2}{c^2}} & \text{For } \alpha^2+\beta^2>\dfrac{\omega^2}{c^2}\end{cases} \tag{4.5}$$

If we consider a field propagating along the positive z direction, as it must vanish at infinity, the term B must vanish as well. The term A(α, β) can be easily calculated writing the expression of the field in the z = 0 plane

$$\left[E(x,y,z)\right]_{z=0} = \int_{-\infty}^{+\infty}\int_{-\infty}^{+\infty} A(\alpha,\beta)e^{i(\alpha x+\beta y)}d\alpha\, d\beta \tag{4.6}$$

and thus it can be deduced that

$$A(\alpha,\beta) = \left[\widetilde{E}(\alpha,\beta,z)\right]_{z=0} = \frac{1}{4\pi^2}\int_{-\infty}^{+\infty}\int_{-\infty}^{+\infty}\left[E(x,y,z)\right]_{z=0} e^{-i(\alpha x+\beta y)}dx\, dy \tag{4.7}$$

namely A(α, β) is the Fourier transform of the field in the z = 0 plane which is supposed to be known. It follows that

$$\widetilde{E}(\alpha,\beta,z) = \left[\widetilde{E}(\alpha,\beta,z)\right]_{z=0} e^{i\gamma z} \tag{4.8}$$

Finally we can write the solution of the propagation problem as

$$E(x,y,z) = \int_{-\infty}^{+\infty}\int_{-\infty}^{+\infty}\left[\widetilde{E}(\alpha,\beta,z)\right]_{z=0} e^{i\gamma z}\, e^{i(\alpha x+\beta y)}d\alpha\, d\beta \tag{4.9}$$

which can be summarized as follows: "in order to calculate the field propagated from a point in the plane z = 0 to a generic point (x, y, z) we must calculate the Fourier transform of the field in the z = 0 plane, apply the propagator exp[iγ(α, β) z] to each spatial frequency component, and then return to the real space by summing all the spectral components of the field".

From equation (4.9) we can note that the field has been written as a superposition of plane waves having a wave vector $\vec{k}$ = (α, β, γ) the components of which satisfy the relation $\alpha^2+\beta^2+\gamma^2 = \omega^2/c^2$ in vacuum. The result reported in equation (4.7) is also called *angular spectrum* of the field, that is we have calculated the amplitude of the each plane-wave component propagating along the direction defined by the wave vector $\vec{k}$. The notion of spatial frequency is made intuitive by considering the example of a finite grating as illustrated in figure 4.10 (A). It shows a periodicity d along the x axis, while the period is infinite along the y axis, thus the

associated spatial frequencies are $f_x = \alpha/2\pi = 1/d$ along the horizontal direction and $f_y = 0$ along the vertical one. In the Fourier spectrum of this grating there will appear the fundamental frequency $1/d$ as well as the higher harmonics.

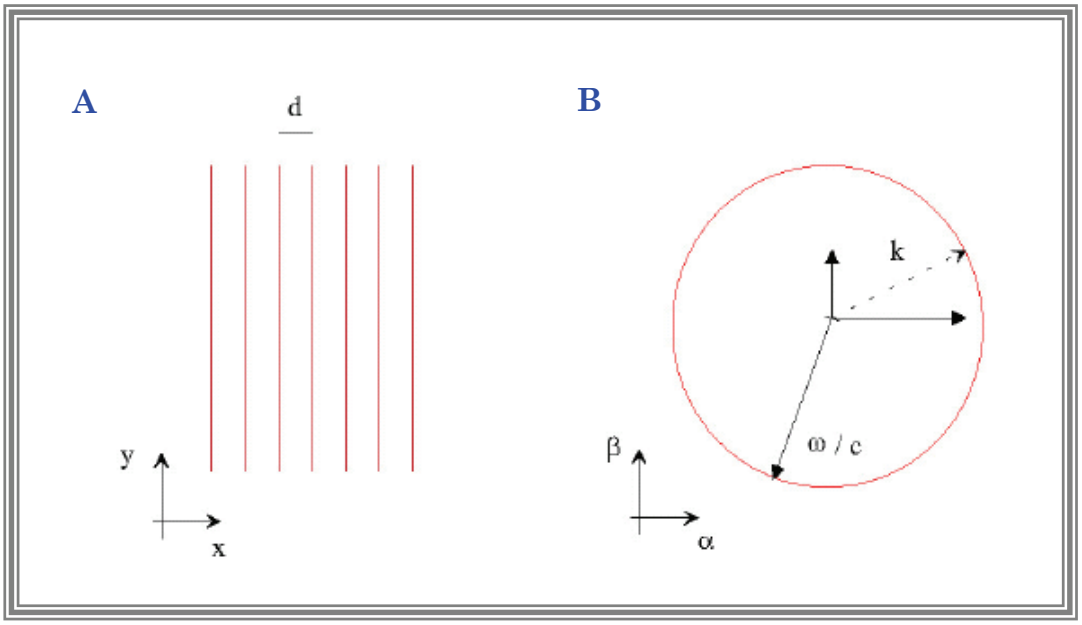

Figure 4.10 Representation of a grating in the real (A) and in the reciprocal Fourier space (B). The grating shows a finite periodicity d along the x-axis and an infinite periodicity along the y-axis. This leads to a wave vector (α, β) in which $\alpha = 2\pi/d$ and $\beta = 0$.

Returning to equation (4.9), the first remark is that each spatial frequency of the function E(x, y, 0) corresponds to a plane wave having a well defined propagation direction. This can be seen in figure 4.10 (B) where we can observe that a weak value of α determines a wave which electric field is mainly along the y direction, while a high value of α corresponds to a wave more and more polarized along the x-axis. The possibility to isolate a single propagation direction, measuring the related amplitude of the electric field, namely the measure of the angular spectrum of the radiation, gives us information on the Fourier transform of the field; this can be done both placing a small detector in the far field of the radiation, or by focussing the radiation onto a screen; in fact each spatial frequency having amplitude $\tilde{E}$

(α, β, 0) corresponds to a propagation direction characterized by a wave vector $\vec{k}$ = (α, β, γ), which itself corresponds to a point on the focal plane image. We can say that propagation provides a spectral analysis in the spatial frequency domain. But the question is more subtle, actually propagation acts also as a *low-pass filter* and this fact puts a limit on the achievable lateral resolution.

Let us consider an example in which high spatial frequencies of the electric field are present, corresponding to rapid variations of the electric field on a short length scale: the incidence of light on a rectangular diaphragm having dimensions a and b. In this case the integral in equation (4.7) gives

$$\widetilde{E}(\alpha,\beta,z=0) \propto \frac{\sin(\alpha a/2)}{\alpha}\frac{\sin(\beta b/2)}{\beta} \tag{4.10}$$

that is the spectrum of the spatial frequencies generated by the object. We note that the spectrum decreases slowly towards the high frequencies due to the discontinuity of the field at the edges. It is intuitive that it is almost impossible to reconstruct the sharp boundary edges by superposing only the low spatial frequency components. It is then necessary to use waves having high spatial frequencies to take into account the fact that the field changes abruptly at the edges.

But looking at equation (4.5) we note that for the high spatial frequencies such as $\alpha^2+\beta^2+\gamma^2 \rangle \omega^2/c^2$ the γ component of the wave vector is purely imaginary, this implies that the propagator is not a simple phase factor but gives rise to waves which decay exponentially towards the positive z direction. Far from the source, their contribution is completely negligible and they do not contribute to the image formation if the detector is placed at several λ of distance from the z = 0 plane. Only the low spatial frequencies $\alpha^2+\beta^2+\gamma^2 \langle \omega^2/c^2$ have a real component of the wave vector along the z direction and can propagate. The maximum value for the wave vector in the (x , y) plane is $\omega/c = 2\pi/\lambda$ corresponding to a spatial frequency $f_{\max} = 1/\lambda$. It is then evident that the fine details of the structures of E (x , y, 0) which are

smaller than the radiation wavelength, are lost during the propagation, so that any conventional optical image cannot give raise to details smaller than $\cong \lambda$.

The fact that the high spatial frequencies, characterized by having $\left|k_{\Uparrow}\right|^2 \rangle \omega^2/c^2$ decrease exponentially on a length scale $z = 1 / \gamma$, while the low frequency ones can propagate towards infinity, justifies the statement that propagation acts as a low-pass exponential filter on the angular spectrum. This behaviour defines two different spatial regions: the **Near-Field** region which is located at small distances $z << \lambda$ from the sample, where the high frequency components still "survive"; and the **Far-Field** region, located at $z >> \lambda$, where only the low frequencies have a non negligible amplitude. This can be put on an analytical formulation by rewriting equation (4.9) as

$$\mathrm{E}(\mathrm{x},\mathrm{y},\mathrm{z}) = \mathrm{E}_{\mathrm{FAR-FIELD}}(\mathrm{x},\mathrm{y},\mathrm{z}) + \mathrm{E}_{\mathrm{NEAR-FIELD}}(\mathrm{x},\mathrm{y},\mathrm{z}) \tag{4.11}$$

where

$$E_{FAR-FIELD} = \int\int_{\alpha^2+\beta^2 \langle \frac{\omega^2}{c^2}} \widetilde{E}(\alpha,\beta,z=0)\, e^{i\gamma z}\, e^{i(\alpha x+\beta y)}\, d\alpha\, d\beta \tag{4.12}$$

$$E_{NEAR-FIELD} = \int\int_{\alpha^2+\beta^2 \rangle \frac{\omega^2}{c^2}} \widetilde{E}(\alpha,\beta,z=0)\, e^{-|\gamma| z}\, e^{i(\alpha x+\beta y)}\, d\alpha\, d\beta \tag{4.13}$$

It is evident that conventional microscopy techniques both illuminate and collect light in the far-field and this limits the achievable lateral resolution. To obtain sub-wavelength resolution it is in fact necessary to collect the hidden information, the high spatial frequencies, where it is located, that is very close to the surface under investigation. Two complementary solutions can be adopted: we can illuminate the surface from the far field and place a small detector at close distance from the surface, which will be sensible to evanescent waves; otherwise it is possible to illuminate locally the sample with an electromagnetic field containing high spatial frequencies, and then detect the scattered light in the far-field. In this case as the high spatial

frequencies correspond to evanescent waves, the nanosource will be kept close to the surface.

We will now analyze more deeply the diffraction phenomenon, how it naturally arises from the propagation theory and how it limits the spatial resolution. The expression (4.7) shows that the amplitude of the spectral components of the electromagnetic field are given by its Fourier transform. We can then apply the mathematical properties of the Fourier transform to our case: let Δx be the width of a light beam travelling along the z direction, and α_{MAX}, the maximum value of the wave-vector component along x. We can write:

$$\Delta x \, \alpha_{MAX} \geq 2\pi \tag{4.14}$$

which is equivalent to the Heisenberg uncertainty relation. If the field does not change rapidly on a length Δx , this inequality provides the order of magnitude of the high-frequency cut-off of the angular spectrum $\alpha_{\max} \approx 2\pi/\Delta x$.

This expression describes what is traditionally called *natural diffraction* of a light beam; in fact if we introduce the angle θ formed by the wave vector $\vec{k}$ = (α, β, γ) and the z propagation axis (i.e. $\cos\theta = \hat{k} \cdot \hat{z}$), we can write $\alpha = 2\pi/\lambda \sin\theta$ and then, for small angles, $\theta_{MAX} \approx \lambda/\Delta x$. This formula gives an order of magnitude for the divergence angle of a general source having linear dimensions Δx, as for example a slit or even a laser beam. Equation (4.14) links as well the dimensions of the smallest object observable with the maximum value of the spatial frequency present in its spectrum which will be of the order of $\alpha_{\max} \approx 2\pi/\lambda$ in the conventional far-field experiments, giving a maximum achievable lateral resolution $\Delta x \cong \lambda$.

4.3.2 SNOM configurations: Collection-Mode and Illumination-Mode

A possible classification of SNOM concepts [53] is based on the role of the probe that can be used either as a collector or as an illuminator, see figure 4.11. We briefly summarize the working principles of SNOM describing its main configurations: Collection-Mode and Illumination-Mode.

We have discussed the possibility to overcome the diffraction limit by detecting the high spatial frequency components which are localized in the so called near-field region and in order to do this two conditions must be fulfilled:

- The nano-probes must couple with the high spatial frequencies of the electromagnetic fields. This implies that its dimensions must be of the order of the smallest feature we want to image.

- The nano-probes must be placed in the near-field region, i.e. very close to the sample surface (d << λ).

In particular it can be demonstrated that for the high spatial frequencies the cut-off length $\Lambda = 1/\sqrt{k_{\Uparrow}^2 - k^2}$ gives the order of magnitude for the probe-sample maximum distance for which a resolution $\Delta x \approx 2\pi/|k_{\Uparrow}|$ can be obtained.

This summarizes the physical principle of what is called collection-mode SNOM [54], in which the sample is irradiated by a source located in the far field, while the nano-probe can be either the small aperture present at the edge of a tapered optical fiber (aperture-SNOM), or a tapered metallic (or dielectric) AFM tip (apertureless-SNOM). However the most widely employed and versatile configuration is the illumination-mode SNOM in which the high spatial frequencies of the sample are "stimulated" directly by the fields emitted by the nanosource and the scattered light is collected in the far field.

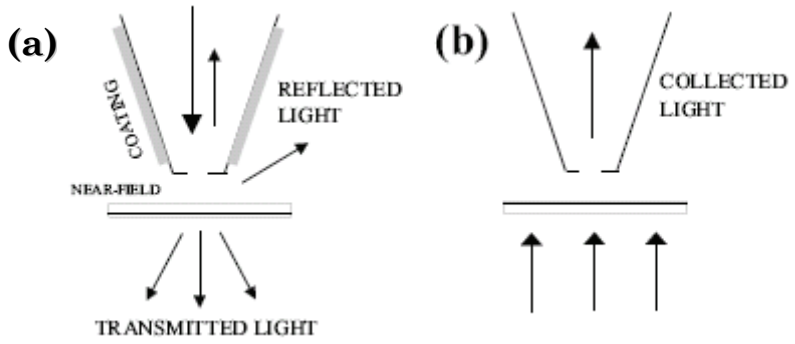

Figure 4.11 Near field microscopes classification (a) Illumination-mode SNOM and (b) Collection-mode SNOM.

It has been demonstrated that, by using the reciprocity theorem [55], there exist an equivalent illumination-mode setup for any collection-mode one and vicecersa.

Again two conditions must be fulfilled:

- The field emitted by the nanosource must couple with the surface features. This means that the nanosource must be small enough to generate and excite the high spatial frequencies of the sample.

- The sample must be placed in the near field of the nanosource.

The modelization of the illumination-mode SNOM can be carried out again in the framework of propagation-scattering theory in addition to a model for the fields emitted by the aperture.

Rigorous calculation of the electric field emitted by a real nanosource is a very difficult problem which has not yet been solved exactly. For an aperture probe the simplest model is to suppose that its properties can be correctly described by calculation of the emission field of a small circular aperture in a metallic screen. That is a classical problem in diffraction theory. The most drastic approximation is to suppose that the field in the aperture is the incident field: this is the well known Kirchhoff

approximation. The results of such an approximation are discussed in Jackson's textbook [56]. But when the diameter of the aperture is small compared with the wavelength, the Kirchhoff approximation is no longer valid because boundary conditions have to be taken into account and the field inside the aperture can no longer be approximated by the incident field. In 1944 Bethe [57] presented a more rigorous method: he derived the diffracted field from a fictitious magnetic charge and current inside the hole. In 1950 Bouwkamp [58] corrected the mistake in Bethe's equation for the near-field. Recently calculations were performed on a more realistic screen with non-vanishing thickness and finite conductivity [59]. Other models have been developed using the Green dyadic function [60] or the multiple-multipole approximation [61] but they are quite complicated, require long computation times and only numerical results are presented. In contrast the Bethe-Bouwkamp method leads to analytical formulas, which explains why it is so extensively used in near-field calculations.

4.3.3 SNOM operation modes: Constant Height and Constant Gap Modes

Although different SNOM designs have been developed, each suitable for a particular application, from a mechanical point of view the SNOM is a member of the scanning probe microscopy family. Here the physical interaction between the probe and the sample is characterized by the exchange of photons and the measured quantities are related to the optical properties of the samples.

In its most general concept a SNOM can be sketched as reported in figure 4.12 and it consists of:

- A probe acting as a nanoscopic light scatterer.
- A piezoelectric transducer capable to move the sample with the desired precision.
- A detector of the probe/sample interaction.
- An independent device for controlling the probe/sample distance.
- A computer driving the entire system.

A very precise sample scan is achieved by means of piezoelectric transducers. Usually the sample is raster scanned with respect to the probe but only the relative motion is important; if the probe is scanned, the microscope is called stand-alone. In our sketch the sample is mounted on a transducer, in the non stand-alone configuration. The scan is made on the xy plane either at constant speed or by discrete steps. Constant speed (from about 10 nm/s to a few μm/s) is generally preferable for probe preservation. The light scattered by the sample is collected differently depending on the specific configuration, and driven to the detector. Data sampling is always made at discrete steps, by means of an Analog to Digital Converter (ADC) card and a personal computer; a half tone image is then reconstructed from the acquired data matrix.

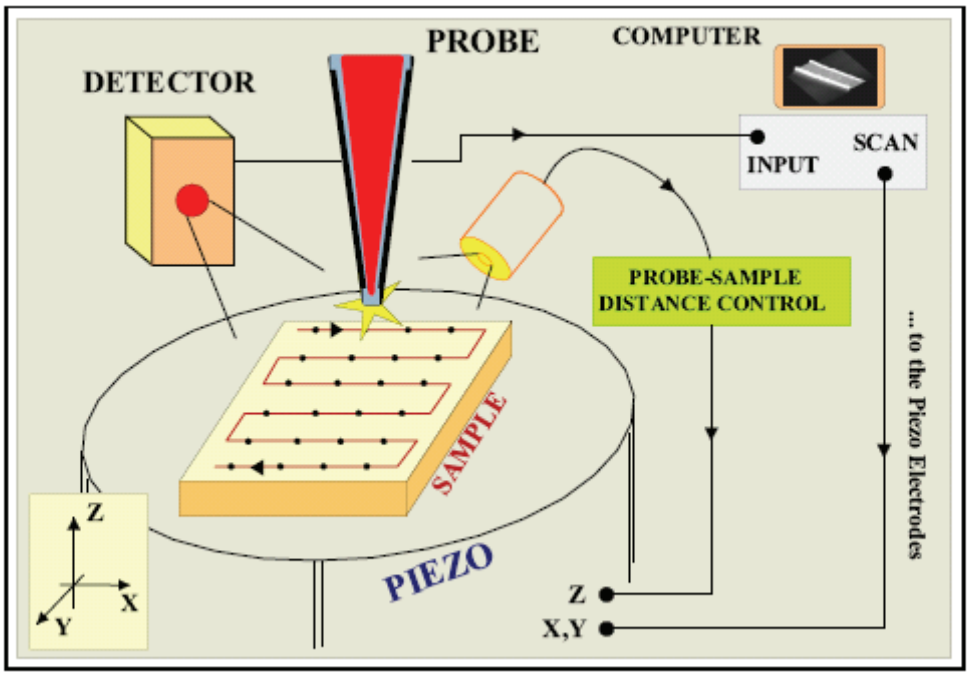

Figure 4.12 Basic sketch of Scanning Near Field Optical Microscope.

During the scan, the probe-sample distance is controlled in such a way to keep the probe within the surface field region. A distance measurement is performed, necessary to control the z position of the sample by means of a

feedback loop. Two distinct operation modes can be employed as shown in figure 4.13: in constant height mode (CHM) the probe scans the sample at a fixed height from the mean surface plane; in this configuration the feedback loop is not active, but it can be automatically switched on to prevent the probe from accidentally touching the surface.

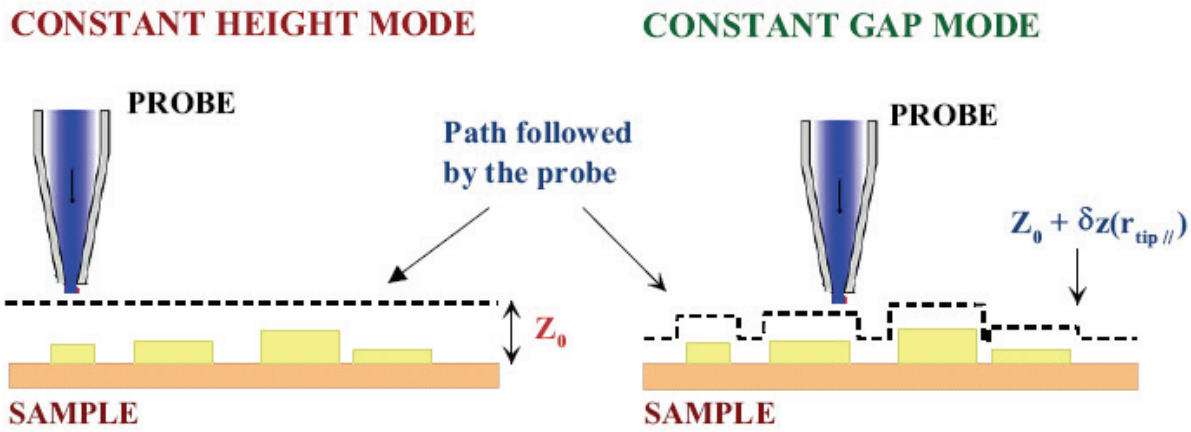

Figure 4.13 Schematics of the operation modes.

In the previous paragraphs we pointed out that a SNOM, in order to get a resolution comparable to the aperture diameter *a,* must operate at distances from the sample of $d \le a/10$ that is $d \le 10\,nm$; this means that CHM can be used only on samples where the roughness is less than a few nm. Differently, in the constant gap mode (CGM), thanks to the feedback loop, the probe follows exactly the surface roughness. Moreover in CGM the loop adjustment signal is acquired to form the topography image which can thus be obtained simultaneously with the image of the probe-sample optical interaction. These two images must be analyzed in conjunction and a comparison between the two is worthwhile in order to identify measurement artifacts.

4.4 The scanning probe system

The scanning probe system is a commercial AFM-SNOM aparartus: the MultiView 1000 by Nanonics Imaging Ltd. (detailed information about the system can be found on the website www.nanonics.co.il). This system is capable of simultaneous collection mode SNOM and normal force AFM imaging using the same probe. In such a way, it is possible to simultaneously relate the optical behaviour, with subwavelenght resolution, to structures topography imaged with similar resolution.

The scanning instrument is configured around a dual optical microscope by Olympus, see figure 4.10.

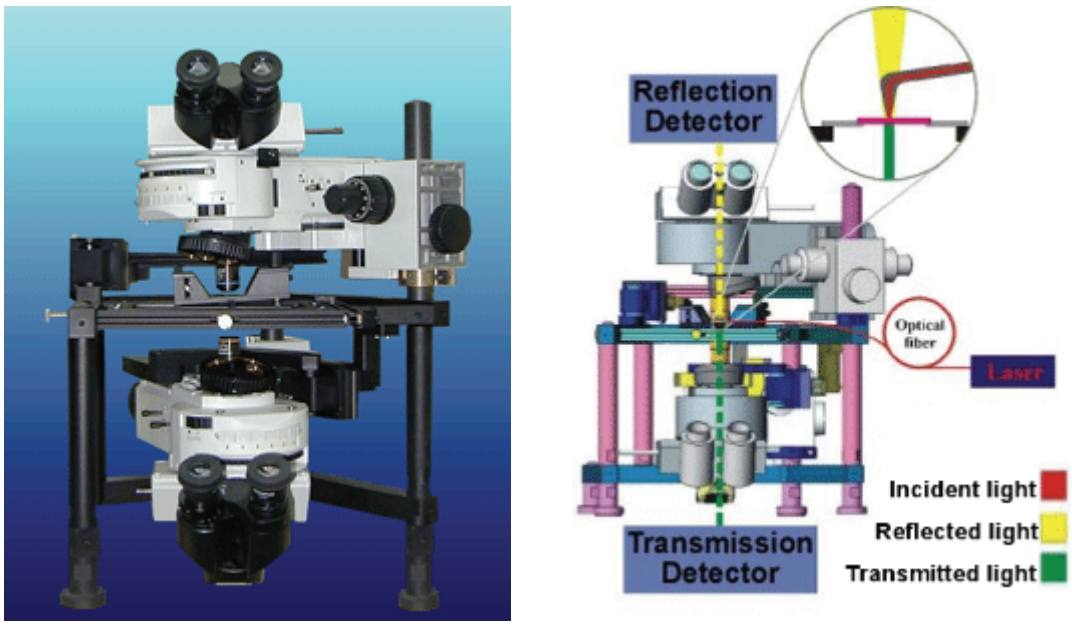

Figure 4.10. Complete MultiView 1000 system with a dual optical microscope.

Such an arrangement allows the SNOM head, showed in figure 4.11, incorporating the probe and its positioning mechanism, to be mounted at the specimen stage location, with a long working distance objective positioned above the stage. The probe can be guided effectively to the chosen scanning area by the objective and a CCD camera, because the probe itself easily fits

under such objective without obscuring the far-field view through the lens (see figure 4.11).

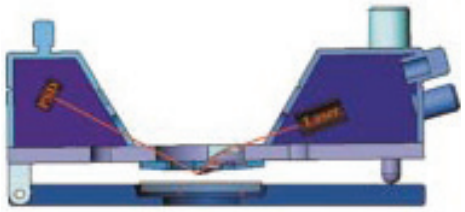

Figure 4.11. SNOM head.

In other words, the unique geometry of the Nanonics SNOM head and cantilevered probes leaves the optical axis free both above and below the sample, allowing the user to view the tip positioning during scanning and to perform SNOM imaging in reflection, transmission, and collection modes. The SNOM probe consists of a modified AFM cantilever fabricated from a conventional tapered optical fibre having a near 90-degree bend close to the tip aperture and coated with metal on the bottom of the tip itself.

Like all other scanning probe techniques at the heart is the scanning system: its design and function are primary determinants of the attainable scan resolution. A 3D flat scanner is employed to move the specimen under the fixed probe in a raster pattern to generate the desired images. It allows for up to 75 microns of x, y and z fine motion of the sample and a high resolution in the z direction (~ 0.01 nm). The required precision of the sample positioning necessitates that the whole system rest on a vibration isolation table to eliminate the transfer of mechanical vibrations from the external environment to the instrument itself.

The z-position of the probe tip and its instantaneous separation from the specimen surface is monitored with a standard optical system. Moreover the tip was maintained in the near field of the sample surface using a real time normal force feedback. This was accomplished by oscillating the tip (perpendicular to the specimen surface) and detecting, by mean of a quadrant photodiode, the scattered light from a diode laser focused onto the top of the probe. As the sample surface approaches the tip, the signal

decreases and the feedback circuit is used to maintain a constant tip–sample distance (about 15 nm), while scanning the sample under the tip. The normal force feedback signal provides a topographic image of the samples simultaneously generated with the optical images.

The super-resolution of SNOM is achieved by the subwavelength aperture (diameter d=300 nm of the used tapered optical fibre coated with 100 nm of Cr-Au) placed into the sample near-field. While, AFM resolution in the x, y directions is of the order of the probe terminal part dimension and in z direction is limited only by electronic noise and by the mechanical vibrations of the probe above the surface.

In the present work, it was always used tapping operating mode. A set of tapered cantilevered multimode fibre (850-1300 nm, core diameter 50 μm) probe (spring constant : ~ 3 N/m) with a 300 nm optical aperture was used to collect radiation in the NIR range. The cantilever was oscillated at its resonant frequency. The oscillation amplitude decreases when the sample surface is brought close enough to the tip so that the tip feels the attractive and repulsive forces. Tapping mode works by keeping a damped constant oscillation amplitude as the tip scans over the surface, in order that the tip-sample distance is held constant. In this study, the cantilever was oscillated at high amplitude and the set point for imaging was 80%, i.e. the amplitude was damped to about 80% of its amplitude in free space due to the interaction between the tip and surface.

In order to investigate the topographic and optical properties of the deposited films it was used a configuration called direct configuration and it was only sometimes used the so called reverse configuration.

As it is possible to see in figure 4.12, in the direct configuration:

- the fabricated samples (optical fibre with SnO_2 layers deposited onto the cleaved transverse section) were coupled to a superluminescent diode with central wavelength λ=1550 nm and an output power of approximately 0.25 mW;
- the emergent optical field from the layers were collected by the SNOM probe, which was in turn coupled to an InGaAs detector.

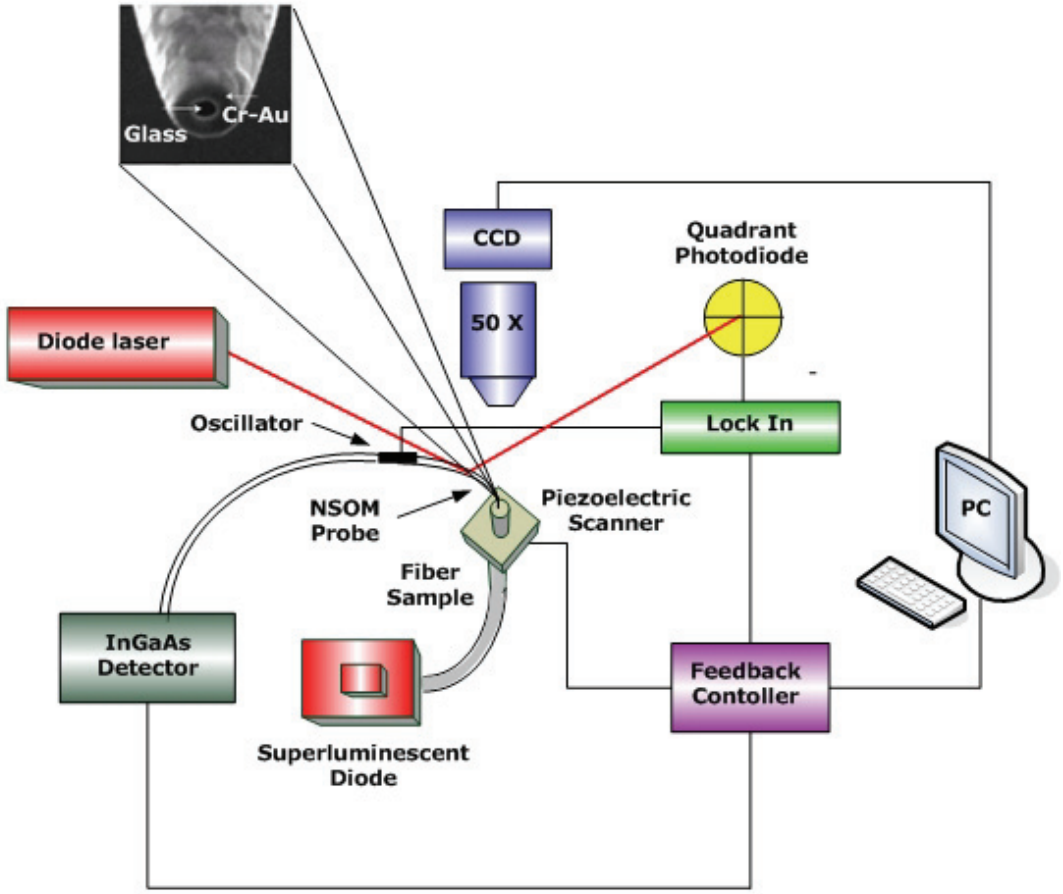

Figure 4.12. Scheme of the direct configuration.

While in the reverse configuration (figure 4.13) the cantilevered optical probe was coupled to the superluminescent diode and the fibre sample was coupled to the InGaAs detector.

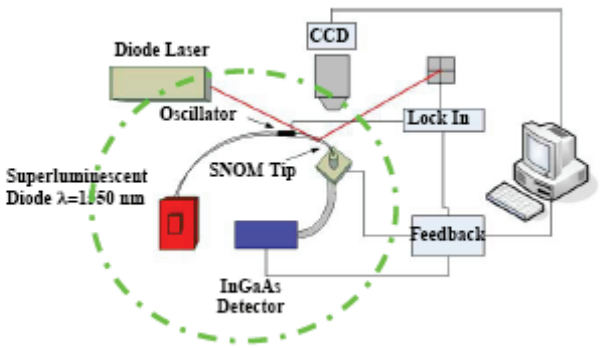

Figure 4.13. Scheme of the reverse configuration.

All the AFM-SNOM images reported in this work were processed by the WSxM free software by Nanotec [62].

References

[1] G. Binnig, H. Rohrer, Ch. Gerber, E. Weibel, "Surface study by scanning tunneling microscopy," Phys. Rev. Lett. 49, 57-61 (1982).

[2] G. Binnig, C. F. Quate, Ch. Gerber, "Atomic force microscope," Phys. Rev. Lett. 56, 930-933 (1986).

[3] B. Bhushan, Handbook of Micro/Nanotribology, 2nd edn. (CRC, Boca Raton 1999).

[4] O. Marti, J. Colchero, j. Mlynek, "Combined scannino force and friction microscopy on mica," Nanotechnol. 1, 141-144 (1990).

[5] N. A. Burham, R. J. Domiguez, R. L. Mowery, R. J. Colton, "Probing the syrface forces of mono-layer films with an atomic force microscope," Phys. Rev. Lett. 64, 1931-1934 (1990).

[6] O. Marti, B. Drake, P.K. Hansma, "Atomic force microscopy of liquid-covered surfaces: atomic resolution images," Appl. Phys. Lett. 51, 484-486 (1987).

[7] B. Drake, C. B. Prater, A. L. Weeisenhorn, S. A. C. Gould, T. R. Albrecht, C. F. Quate, D. S. Cannell, H. G. Hansma, P. K. Hansma, "Imaging crystals, polymers and processes in water with atomiv force microscope," Science 243 1586-1589 (1989).

[8] G. Meyer, N. M. Amer, "Novel approach to atomic force microscopy," Appl. Phys. Lett. 53, 1045-1047 (1988).

[9] F. J. Giessibl, Ch. Gerber, G. Binnig, "A low-temperature atomic force/scanning tunneling microscope for ultrahigh vacuum," J. Va. Sci. Technol. B 9, 984-988 (1991).

[10] T. R. Albrecht, P. Grutter, D. Rugar, D. P. E. Smith, "Low temperature force microscope with all-fibre interferometer," Ultramicroscopy 42-44, 1638-1646 (1992).

[11] C. Basire, D. A. Ivanov, "Evolution of the lamellar structure during crystallization of a semicrystalline-amorphous polymer blend: Time resolved hot-stage SPM study," Phys. Rev. Lett. 85, 5587-5590 (2000).

[12] E. A. Synge, "A suggested method for extending microscopic resolution into the ultramicroscopic region", Phil. Mag. 6, 356-362 (1928).

[13] M. Fee, S. Chu and T.W. Hansch, "Scanning electromagnetic transmission line microscope with sub-wavelength resolution," Opt. Commun. 69, 219-224 (1989).

[14] F. Keilmann, K.W.Kussmaul, and Z. Szentirmay, "Imaging of optical wavetrains", Appl. Phys. B 47, 169-176 (1988).

[15] A. Lewis, M. Isaacson, A. Harootunian, et al., "Development of a 500 A spatial resolution light microscope: light is efficiently transmitted through l/16 diameter apertures," Ultramicroscopy 13, 227 (1984).

[16] D. W. Pohl, W. Denk, and M. Lanz, "Optical stethoscopy: image recording with resolution l/20,"Appl. Phys. Lett. 44, 651 (1984).

[17] E. Betzing, J. K. Trautman, T.D. Harris, J. S. Weiner and R. L. Kostelak Science 251, 1468 (1991).

[18] E. Betzig, P. L. Finn and J. S. Weiner Appl. Phys. Lett. 60, 2484 (1992).

[19] R. Toledo-Crow, P. C. Yang, Y. Chen, and M. Vaez-Iravani, Appl. Phys. Lett. 60, 2957 (1992).

[20] F. Zenhausern, M. P. O'Boyle, and H. K. Wickramasinghe, Appl. Phys. Lett. 65, 1623 (1994).

[21] F. Zenhausern, Y. Martin, and H. K. Wickramasinghe, Science 269, 108 (1995)

[22] R. Bachelot, P. Gleyzes, and A. C. Boccara, Opt. Lett. 20, 1924 (1995)

[23] Y. Martin, F. Zenhausern, and H. K. Wickramasinghe, Appl. Phys. Lett. 68, 2475 (1996).

[24] J. K. Trautman et al. J. Appl. Phys. 71, 4659 (1992).

[25] E. Betzig, J. K. Trautman, T. D. Harris, J. S. Weiner, and R. Wolfe, Appl. Opt. 31, 4563 (1992).

[26] E. Betzig and R. J. Chichester, Science 262, 1422 (1993).

[27] H. F. Hess, E. Betzig, T. D. Harris, L. N. Pfeiffer, and K. W. West, Science 264, 1740 (1994).

[28] R. D. Grober et al., Appl. Phys. Lett. 64, 1421 (1994).

[29] R. D. Grober, T. D. Harris, J. K. Trautman, and E. Betzig, Rev. Sci. Instrum. 65, 626 (1994).

[30] J. K. Trautman, J . J . Macklin, L. E. Brus, and E. Betzig, Nature 369, 40 (1994)

[31] X. S. Xie and R. C. Dunn, Science 265, 361 (1994).
[32] S. Webster, D. N. Batchelder, and D. A. Smith, Appl. Phys. Lett. 72, 1478 (1998)
[33] D. Zeisel, V. Deckert, R. Zenobi, and T. Vo-Dinh, Chem. Phys. Lett. 283, 381 (1998).
[34] M. K. Herndon, R. T. Collins, R. E. Hollingsworth, P. R. Larson, and M. B. Johnson, Appl. Phys. Lett. 74, 141 (1999).
[35] J. A. Rogers, A. Dodabalapur, Z. Bao, and H. E. Katz, Appl. Phys. Lett. 75, 1010 (1999).
[36] A. Richter et al., Phys. Rev. Lett. 79, 2145 (1997)
[37] V. Emiliani et al., Phys. Rev. B 60, 13335 (1999).
[38] K. Matsuda, T. Saiki, H. Saito, and K. Nishi, Appl. Phys. Lett. 76, 73 (2000)
[39] T. Giinter et al., Appl. Phys. Lett. 75, 3500 (1999)
[40] B. A. Nechay, U. Siegner, F. Morier-Genoud, A. Schertel, and U. Keller, Appl. Phys. Lett. 74, 61 (1999).
[41] Y. Toda, T. Sugimoto, M. Nishioka, and Y. Arakawa, Appl. Phys. Lett. 76, 3887 (2000).
[42] L. A. Gheber, J. Hwang, and M. Edidin, Appl. Opt. 37, 3574 (1998).
[43] U. M. Rajagopalan, S. Mononobe, K. Yoshida, M. Yoshimoto, and M. Ohtsu, Jpn. J. Appl. Phys. Part 138, 6713 (1999).
[44] E. B. McDaniel, J. W. P. Hsu, L. S. Goldner, E. Shirley, and G. W. Bryant, Phys. Rev. B 55, 10878 (1997).
[45] S. Fan, I. Appelbaum, and J. D. Joannopoulos, Appl. Phys. Lett. 75, 3461 (1999).
[46] Nader Jalili and Karthik Laxminarayana, “A review of atomic force microscopy imaging system: application to molecular metrology and biological sciences,” Mechatronics 14, 907-945 (2004).
[47] S. Fujisawa, M. Ohta, T. Konishi, Y. Sugawara, S. Morita, “Difference between the forces measured by an optical lever deflection and by an optical interferometer in an atomic force microscope,” Rev. Sci. Instrum. 65, 644-647 (1994).

[48] R. Garcia and R. Perez, “Dynamic atomic force microscopy methods,” Surface Science Reports 47, 197-301 (2002).

[49] O. Wolter, T. Bayer, J. Greshner, “Micromachined silicon sensors for scanning force microscopy,”J. Vac. Sci. Technol. B 9 1353-1357 (1991).

[50] I. A. Birger, B. F. Shorr, G. B. Iosilevich, “Calculation of details of machines,” Publisher Mashinostroenie, Moscow 1979.

[51] D. Rugar, P. K. Hansma, “Atomic force microscopy,” Phys. Today 43, 23-30 (1990).

[52] J. J. Greffet, “Diffraction, spectre angulaire et ondes evanescentes, in Ecole Thematique in “Microscopie Optique En Champ Proche”, La Londe Les Maures, (2000).

[53] M. Labardi, P. G. Gucciardi, and M. Allegrini, “Near-Field Optical Microscopy,” La Rivista del Nuovo Cimento 23, 1 (2000).

[54] E. Betzig, M. Isaacson, and A. Lewis, Appl. Phys. Lett. 51, 2088 (1987).

[55] E. R. Mendez, J . J . Greffet, and R. Carminati, Opt. Comm. 142, 7 (1997).

[56] J. D. Jackson, Elettrodinamica Classica, Zanichelli, 1984.

[57] H. A. Bethe, “Theory of diffraction by small holes,” Phys. Rev. 66, 163 (1944).

[58] C. J. Bouwkamp, Rep. Phys. 27, 35 (1954).

[59] A. Liu and G. W. Bryant, Phys. Rev. B 59, 2245 (1999).

[60] A. Dereux, C. Girard, and J. C. Weeber, J. Chem. Phys. 112, 7775 (2000).

[61] L. Novotny, D. W. Pohl, and P. Regli, J. Opt. Soc. Am. A 11, 1768 (1994).

[62] I. Horcas, R. Fernandez, J.M. Gomez-Rodriguez, J. Colchero, J. Gomez-Herrero and A. M. Baro Rev. Sci. Instrum. 78, 013705 (2007).

CHAPTER 5

Morphological and near field optical properties

5.1 Near field behaviour of SnO_2 films characterized by well separated microstructures

In this paragraph we will show that very flat SnO_2 film are not able to influence the emerging field while that ones characterized by isolated microstructures, positioned in correspondence of the sample fibre core, reveal highly unusual capability of locally enhancing the collected optical near field. The observed phenomenon leads to new concepts of fibre optic chemical sensors and in fibre microsystem as well [1, 2].

5.1.1 Flat SnO_2 film: sample S9

In figure 5.1 (left) we report the AFM image of the sample S9 topography obtained using a solution volume of 5 ml and a concentration of 0.01 mol/l, before the annealing process. The image refers to a 13.0 μm x 13.0 μm area, approximately centred on the optical fibre core, indicated with a blue circle. Figure 5.2 (left) represent a 3D view of the same image. From these images it is clear that the deposited layer is very flat. In order to have quantitative information about the sample topography we analyzed the surface heights histogram, as reported in figure 5.3; we found an average surface height of 95.11 nm and a RMS roughness (root mean square roughness) of 27.45 nm.
From figures 5.1 (right) and 5.2 (right) it is possible to note that the optical near field collected on the sample surface, simultaneously to its topography, is not influenced by the presence of such SnO_2 layer; in fact it has the expected Gaussian profile of the emergent field from the cleaved end of a single mode optical fibre.

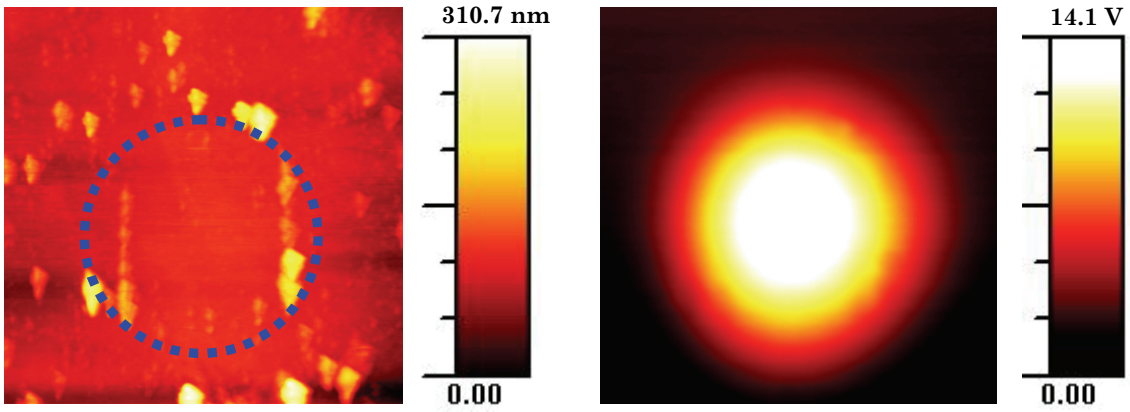

Figure 5.1 AFM topography image (left) and radiation intensity simultaneously collected by the SNOM probe (right), with a scan area of 13.0 μm x 13.0 μm of the sample S9.

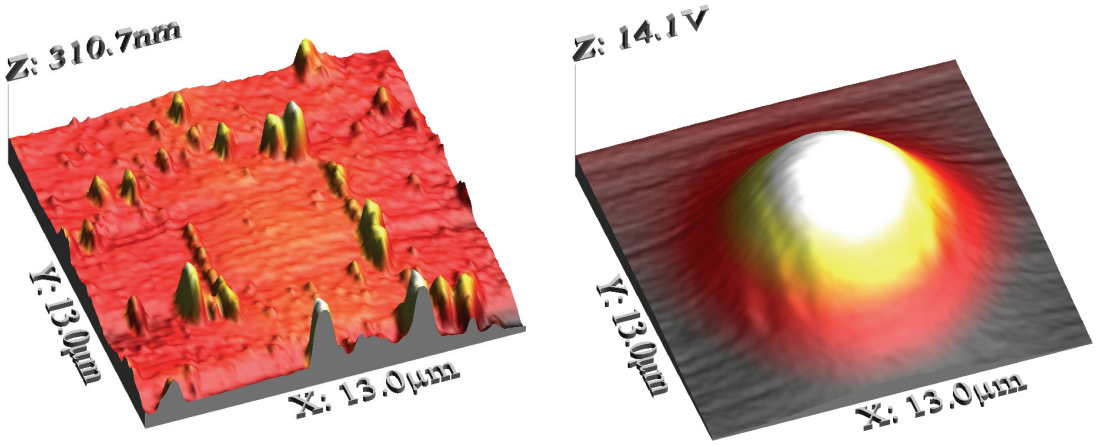

Figure 5.2 Three-dimensional view of the AFM topography image (left) and radiation intensity simultaneously collected by the SNOM probe (right) reported in figure 5.1.

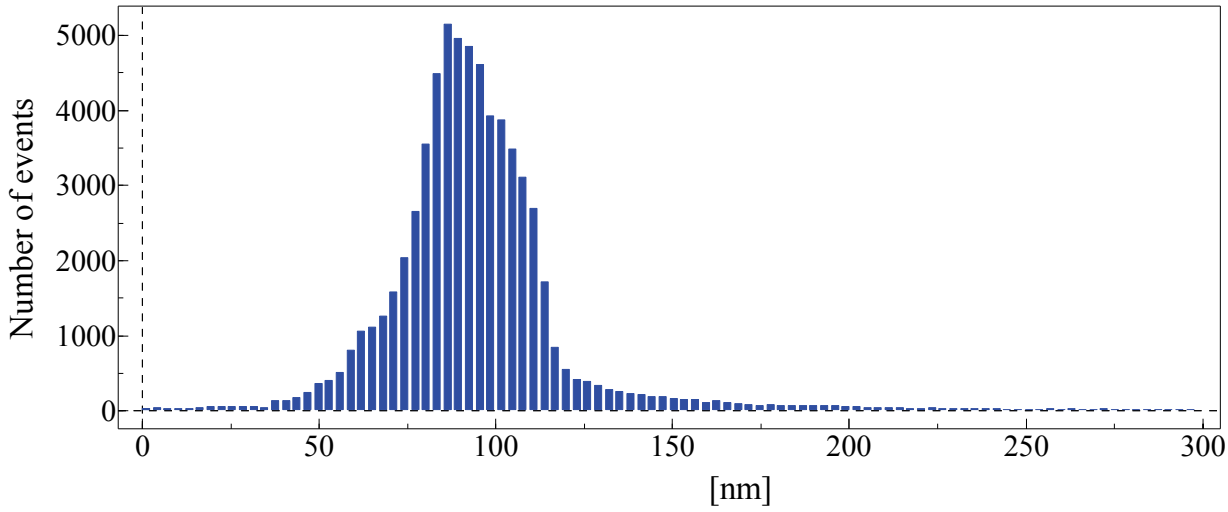

Figure 5.3 Histogram of the heights relative to scanned area of sample S9.

5.1.2 Multi-structures SnO_2 film: sample S4

In figure 5.4 (left) we report the AFM image of the sample S4 topography obtained using a solution volume 5 ml and a concentration of 0.01 mol/l, after the annealing process. Figure 5.6 (left) represent a 3D view of the same image. The image refers to a 11.6 μm x 10.4 μm area, centred on the optical fibre core (see blue circle); it reveals the presence of several microstructures well separated from each other, whose dimensions are reported in figure 5.5.

The shape of the microstructures is ellipsoid like, for this reason we used the symbols A, B and H to indicate the characteristic dimensions: the minor axis, the major axis and the mean height respectively (see figure 5.5).

Figures 5.4 - 5.6 (right) demonstrate that the presence of these micro-structures, with dimensions comparable to he radiation wavelength (λ=1550 nm), leads to a surprisingly modification of the near field profile transmitted through the optical fibre coating: the optical near field is locally enhanced in correspondence of them. In fact, the structures spacing is large enough to make it possible an effective light localization in the high refractive index SnO_2 bumps. In particular, the prominent effect takes place in correspondence of the central one indicated with a black circle in figure 5.5,

whose lateral dimension match very well with λ: A=1.437 μm B=1.542 μm, while the height is H=250 nm.

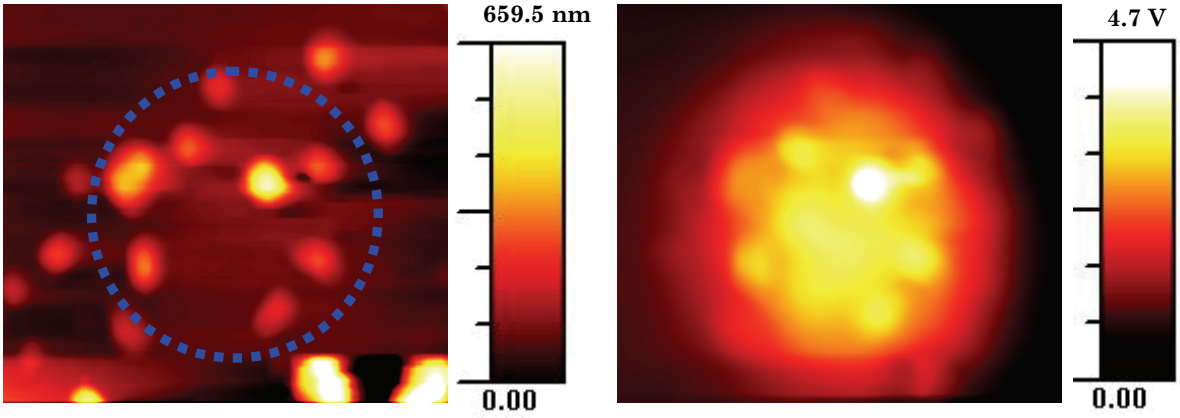

Figure 5.4 AFM topography image (left) and radiation intensity simultaneously collected by the SNOM probe (right), with a scan area of 11.6 μm x 10.4 μm of the sample S4.

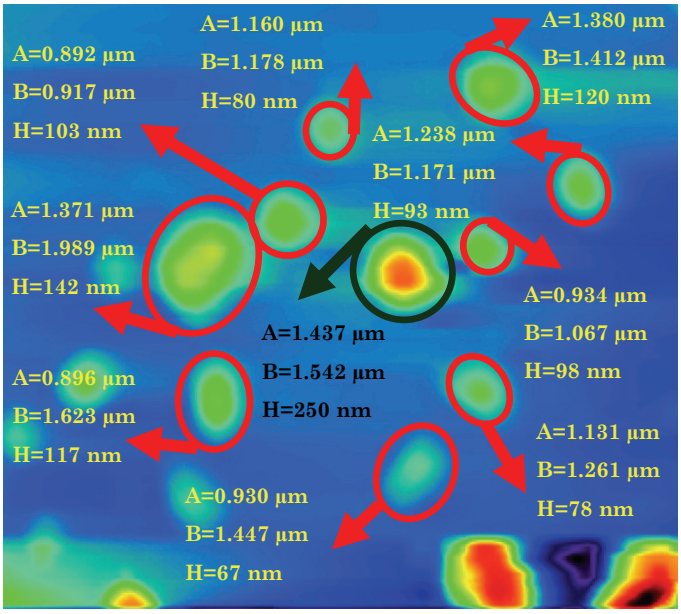

Figure 5.5 Data relative to each microstructure of sample S4 topography reported in figure 5.4 (left).

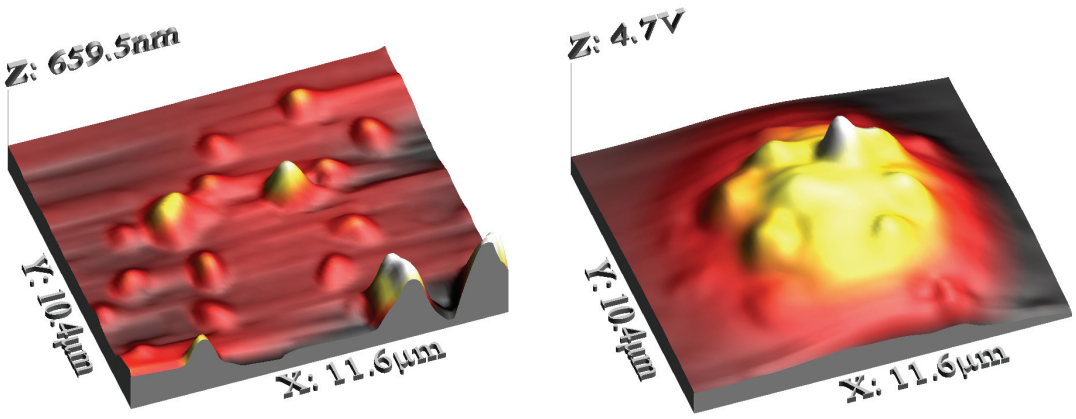

Figure 5.6 Three-dimensional view of the AFM topography image (left) and radiation intensity simultaneously collected by the SNOM probe (right) reported in figure 5.4.

In order to have some quantitative information about the sample topography, we analyzed the height distribution (see figure 5.7) relative to the scanned area; we found an average surface height of 231.70 nm and a RMS roughness of 54.19 nm.

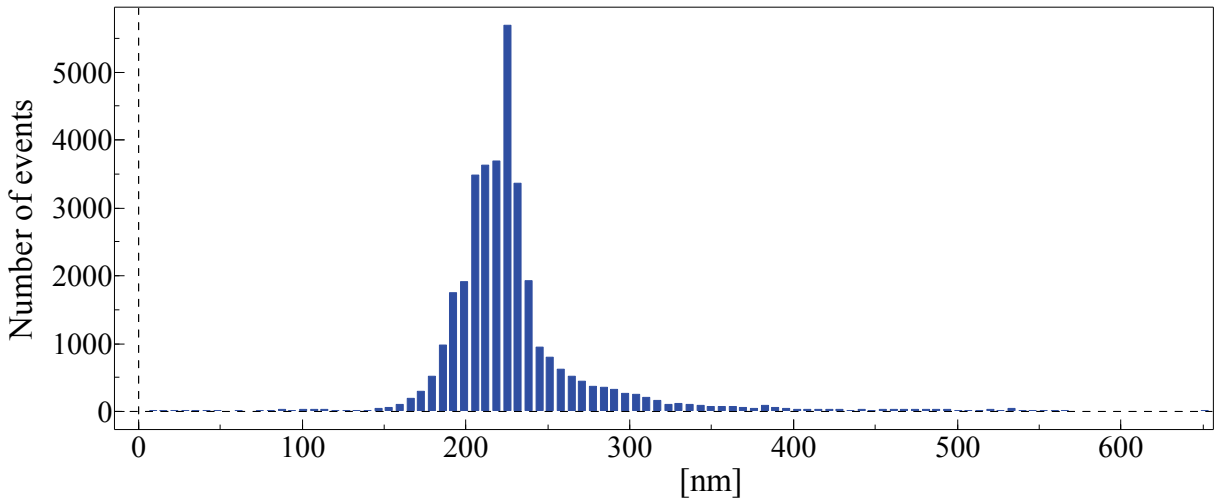

Figure 5.7 Histogram of the heights relative to scanned area of sample S4 reported in figure 5.1 (left).

5.1.3 Double-structure SnO_2 film: sample S11new

In figure 5.8 (left) we report the AFM image of the sample S11new topography obtained using a solution volume 5 ml and a concentration of 0.001 mol/l, after the annealing process. Figure 5.9 (left) represent a 3D view of the same image. The image refers to a 8.8 μm x 7.8 μm area, centred on the optical fibre core; it reveals the presence of two SnO_2 peaks very close to each other and not perfectly resolved because the tip is too large compared to the spatial separation between the structures. The characteristic dimensions of the two structures are: A≈700 nm, B≈2700.0 nm, H≈2400.0 nm and A'≈1300 nm, B'≈ 1900 nm, H'≈2100.0 nm.

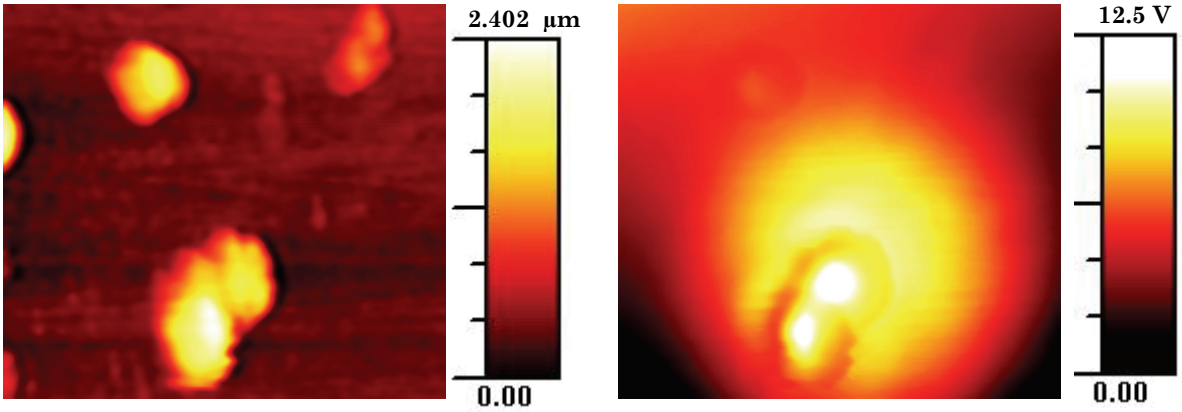

Figure 5.8 AFM topography image (left) and radiation intensity simultaneously collected by the SNOM probe (right), with a scan area of 8.8 μm x 7.8 μm of the sample S11new.

Figures 5.8 - 5.9 (right) demonstrate that the presence of the two micro-structures, with dimensions comparable to the wavelength of the radiation, leads again to a surprisingly modification of near field profile transmitted through the optical fibre coating: the optical near field is locally enhanced in correspondence of these microstructures. Also in this case, the lateral dimensions and the structures spacing are able to confine light in the high refractive index SnO_2 structures leading to an effective light localization.

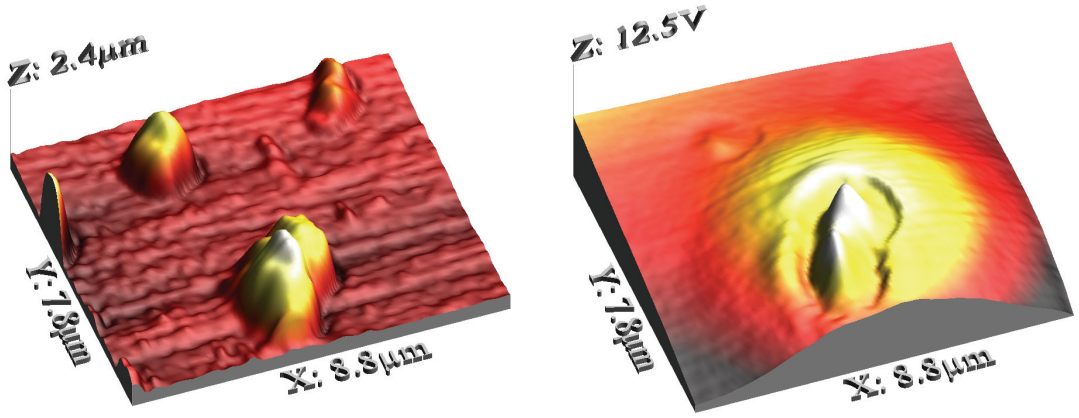

Figure 5.9 Three-dimensional view of the AFM topography image (left) and radiation intensity simultaneously collected by the SNOM probe (right) reported in figure 5.8.

In figure 5.10 we reported the surface heights histogram; we found an average surface height of 0.4977 µm and a RMS roughness of 0.3652 µm.

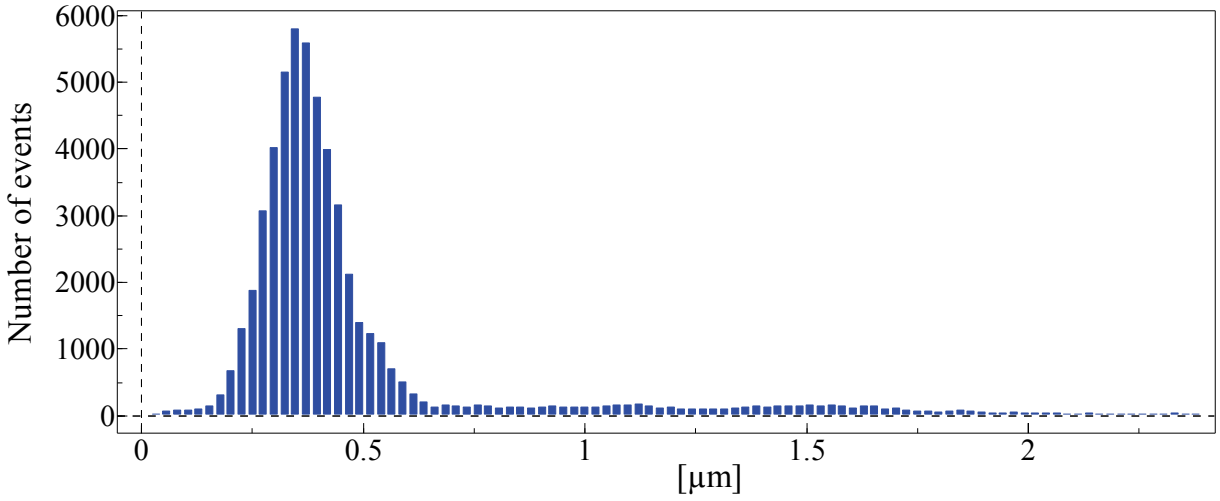

Figure 5.10 Histogram of the heights relative to scanned area of sample S11new reported in figure 5.5 (left).

5.1.4 Single structure SnO_2 film: sample S11

The most pronounced effect of the optical near field enhancement was observed for the sample S11 (prepared using a solution volume 5 ml and a concentration of 0.001 mol/l), whose topography is characterized by the presence of one isolated microstructure in the fibre core region, as shown in figures 5.11 – 5.12 (left). The isolated microstructure has approximately the shape of an half ellipsoid, with dimensions A ≈ 1800 nm, B ≈ 2100 nm and H ≈ 1900.0 nm, on a flat SnO_2 substrate. It is evident from figures 5.11 – 5.12 (right) that the optical near field is strongly enhanced in correspondence of the microstructure.

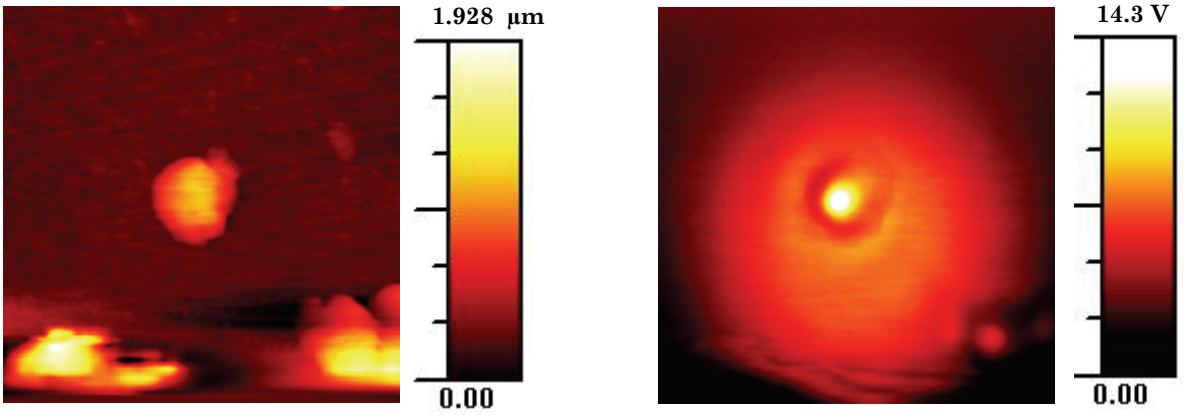

Figure 5.11 AFM topography image (left) and radiation intensity simultaneously collected by the SNOM probe (right), with a scan area of 9.0 µm x 9.0 µm of the sample S11.

In figure 5.13 we reported the surface heights histogram; we found an average surface height of 0.5017 µm and a RMS roughness of 0.2223 µm.

Before discussing the obtained results it is important to stress, that the optical images showed represent the collected optical near field intensity distribution emitted by a standard optical fibre with an SnO_2 coating, when it is illuminated by a superluminescent diode. In other words, they don't represent a contrast due to intrinsic optical properties of the sample. Hence the strong correlation between samples topography and near field profiles reveal an effective enhancement of the optical near field in correspondence of the structures and it is not a contrast enhancement between a flat

substrate and particles with different dielectric constant respect to the substrate.

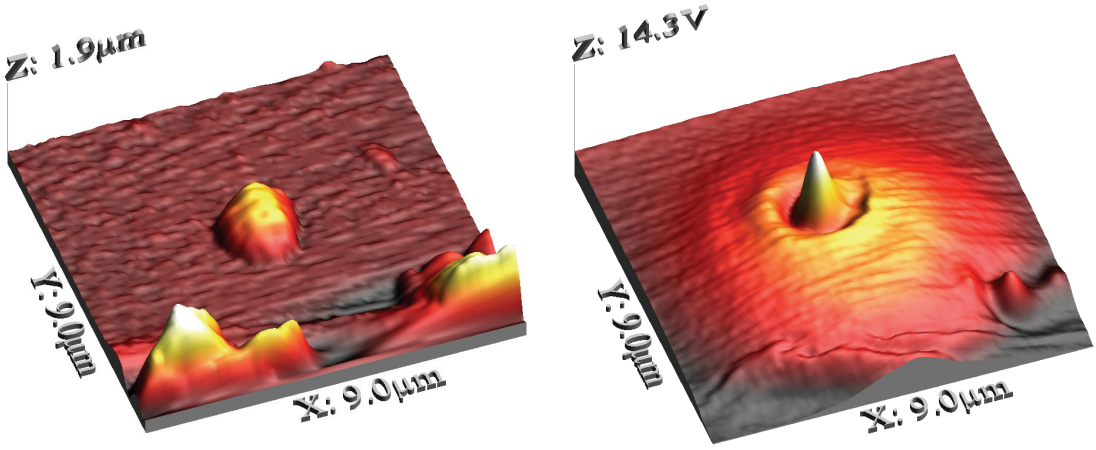

Figure 5.12 Three-dimensional view of the AFM topography image (left) and radiation intensity simultaneously collected by the SNOM probe (right) reported in figure 5.11.

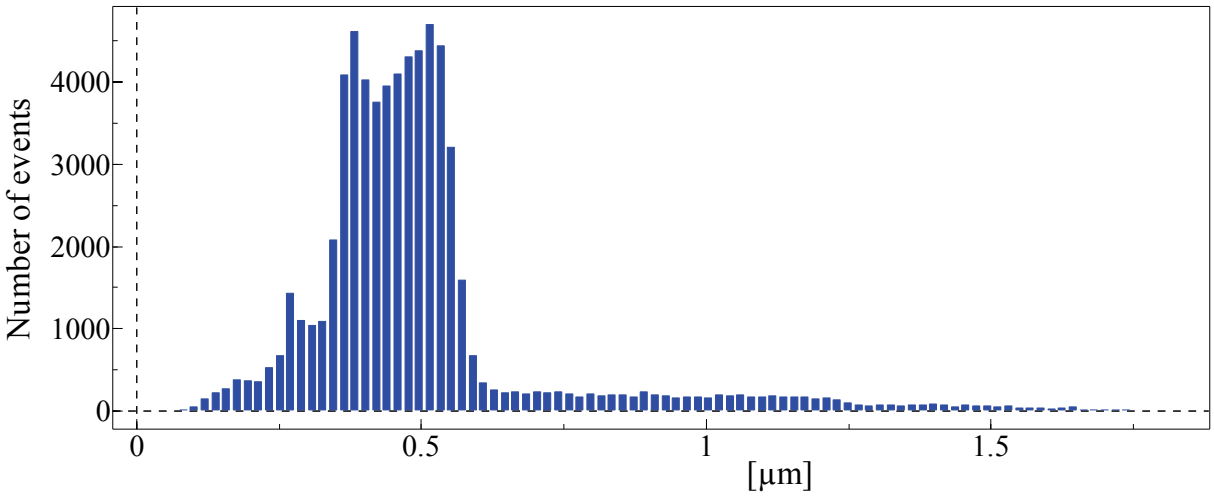

Figure 5.13 Histogram of the heights relative to scanned area of sample S11 reported in figure 5.11.

This was also supported by the experimental evidence that flat SnO_2 films were not able to influence the optical near field emerging from a single mode fibre. On the contrary, a different behaviour was observed in the case of particle layer films characterized by the presence of structures with

dimensions comparable to the operating wavelength injected into the fibre itself.

Moreover, in order to demonstrate that the field enhancement is observable only in the near field range, we also recorded the emergent field at a constant sample-probe distance of approximately 2 μm as reported in figure 5.14. For a sample-tip distance comparable to the optical wavelength, the field profile is not able to completely maintain information about the film morphology, even if a significant distortion of the beam shape is still clearly observable. By increasing the sample-tip distance, up to few times the wavelength (we selected 7 μm), the collected optical field profile assumes the Gaussian shape, as expected in far field imaging.

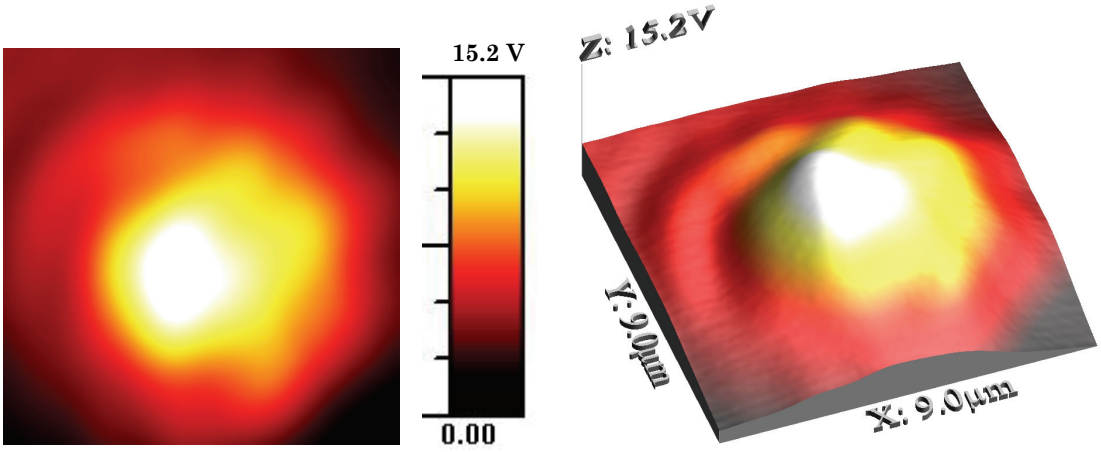

Figure 5.14 Two-dimensional (left) and three-dimensional (right) view of the emergent field intensity collected from sample S11 at constant tip-sample distance of about 2 μm.

With regard to this specific sample, if we suppose that the optical field perturbation is only local (in correspondence of the microstructure), then the unperturbed field can be obtained by interpolating the data upon the exclusion of the microstructure related area. We found that the integrals of the intensity of the perturbed and unperturbed optical field respectively are equal, inferring that the microstructure produces a local redistribution of the intensity distribution. In figure 5.15 we reported a cross-section of the

measured intensity distribution (red line) and of the interpolating surface (dotted blue line) obtained as described above. The local intensity enhancement, calculated as the ratio between the maximum measured intensity and the corresponding intensity of the unperturbed field is about 1.8. The spot-size of the enhanced field measured at FWHM (Full Width Half Maximum) is about 500 nm.

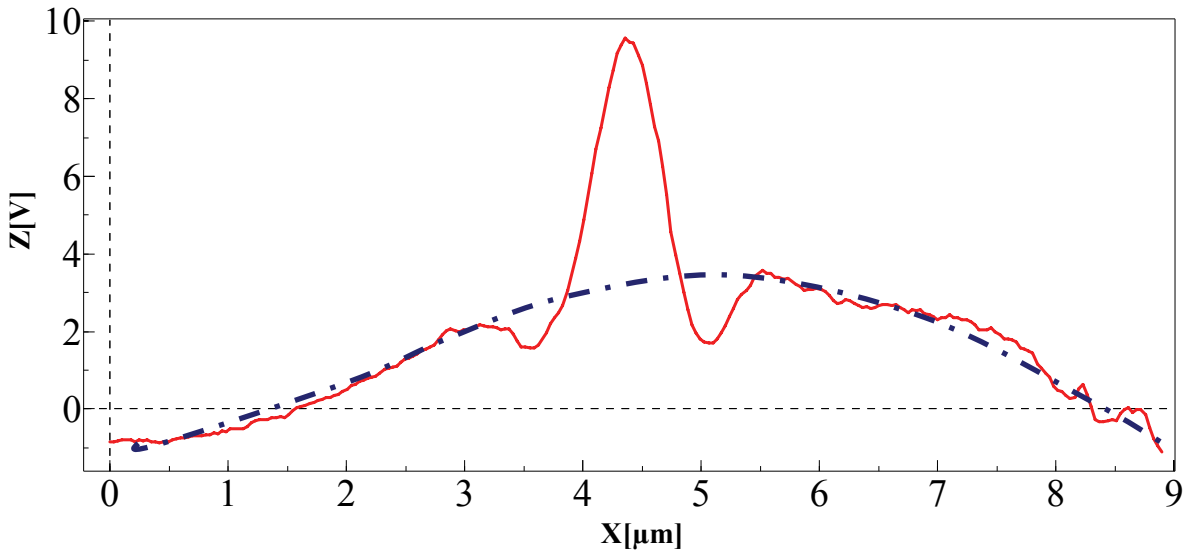

Figure 5.15 A cross-section of the measured intensity of the optical near field (red line) emergent from the sample S11, relative to a line parallel to the y axis of the figure 5.11 (left) passing through the peak and of the interpolating surface (dotted blue line).

In order to better understand the nature of the local field enhancement an additional test was carried out. We modified the experimental set-up in order to have the reverse configuration as described in the chapter 4: the cantilevered optical probe was coupled to the superluminescent diode and the fibre sample was coupled to the InGaAs detector while all the other components were the same. In this way, by scanning the SNOM probe on the sample surface (in a region approximately centred onto the fibre core), it was possible to construct a map of the radiation intensity coupled into the standard optical fibre coated with the SnO_2 overlay. Figure 5.16 shows that

the profile of the radiation intensity coupled to the sample fibre using the reverse configuration, is very similar to that one transmitted through the optical fibre coating and collected in the forward configuration. In this case the local intensity enhancement is about 1.5 calculated using the same procedure reported above in the text.

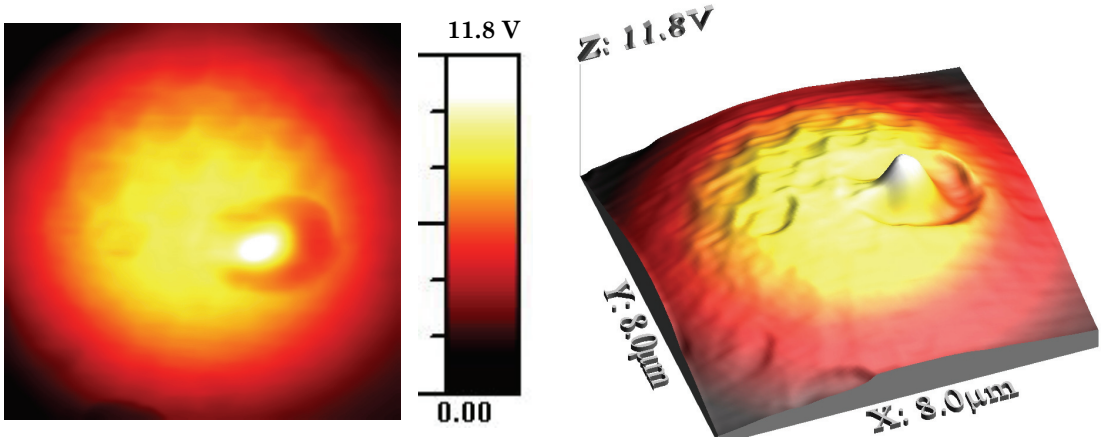

Figure 5.16 Two-dimensional (left) and three-dimensional (right) view of the radiation intensity coupled into the standard optical fibre when the sample S11 was illuminated by the SNOM probe.

Based on these results, it is possible to give an effective explanation of the observed phenomenon. Referring to the direct configuration, we can say that the radiation impinging at the base of the microstructure, coming from the layer of the same material, continues to propagate inside of it confined by the high refractive index contrast between the oxide (SnO_2 refractive index: 1.967 for λ=1550 nm, as above reported) and the air and by the geometry of the microstructure. Near the structure surface and its end, part of the propagative field becomes evanescent and it will be detected by the SNOM probe together with the propagative one. It is well known that when focusing a light beam into a sub-wavelength spot, the electric field of such spot may be represented as the sum of propagating and evanescent modes. In near-field zone the contribution of evanescent modes may become significant compared to propagating modes. Inversely in far-field zone only the propagating modes may be considered. In other words, the local

enhancement of the optical field in the region of the microstructure is also accompanied by a conversion of part of the field from propagative to evanescent. We collected radiation in the near-field zone by the cantilevered optical probe thus recording the sum of the two contributions. Since the structure dimensions are comparable to the radiation wavelength (as revealed from AFM measurements) we can exclude that the local field enhancement can be due to truly evanescent field. In addition, the reverse profile is very similar to that one obtained in forward configuration indicating a strong reciprocity not compatible with a structure able to convert at its ends (due to diffraction limit) all the propagating contribute in the evanescent counterpart. We can conclude that the particle-layer acts as an element able to guide and focuse light and that it works in both direct and reverse configuration.

5.2 Effects of the processing parameters and post processing thermal annealing on film morphology and optical near field

As said in the chapter 2, one of the most important deposition parameter is the metal chloride concentration; in fact it was shown in literature that the concentration of the sprayed solution plays an important role in the film morphology.

In this paragraph we will discuss the features of two groups of layers deposited with different solution concentration: 0.01 mol/l and 0.001 mol/l.

After the deposition procedure and after the morphological and optical characterization, the prepared samples had been annealed at 500±5°C for 1 hour in order to transform SnO_x to SnO_2 and to clean the films surface from the other dopants, like water or alcohol present in the initial solution. The temperature had been increased from room temperature to 500°C with a constant rate of 5°C/min and, after the annealing procedure, the temperature has been decreased with the same rate down to the room temperature. Of course, after the annealing process the samples was been characterized again.

We are able to compare the sample topography before and after the annealing process because, collecting the emerging field from the sample fibre, we are sure to be investigating almost the same spatial region centred on the sample fibre core.

For each investigated sample we will report the topography and the near field intensity, simultaneously collected, before and after the thermal treatment, in order that it will be possible to evaluate some common features between samples deposited at the same solution concentration and some effect of the thermal treatment on the surface morphology and on the emerging field.

5.2.1 Effect of the sprayed solution concentration on the films morphology

In this paragraph we will analyze the surface morphology of two groups of samples deposited with different metal chloride concentration:

- Concentration 0.001 mol/l: sample S11new, sample S12, sample S15, sample S17 and sample S18.
- Concentration 0.01 mol/l: sample P2, sample S4, sample S6new, sample S7 and sample S9.

In order to easily compare the films morphology of samples belonging to the same group, we will discuss the features relative to each one and after we will report all the topography images in the same page.

Sample S11 new topography (see figure 5.17 A) is characterized by the presence of three microsctructure; two of which are very close to each other and not perfectly resolved because the tip is too large compared to the spatial separation between the structures. As for the previous cases we use the symbols A, B and H to indicate the structures characteristic dimensions: the minor axis, the major axis and the mean height respectively. The characteristic dimensions of the these two structures are: A≈700 nm, B≈2700 nm, H≈2400 nm and A'≈1300 nm, B'≈ 1900 nm, H'≈2100 nm. While the dimensions of the third are A≈1540 nm, B≈1770 nm and H≈1500 nm.

Sample S12 topography (see figure 5.17 B) is characterized by the presence of several microstructures well separated from each other, whose shape is ellipsoid like. The characteristic dimensions A, B and H vary in the following ranges: A ∈ (1.2 ÷2.2) μm, B ∈ (1.3 ÷3.9) μm, H ∈ (500 nm ÷1.2 μm).

Sample S15 surface (see figure 5.17 C) presents three microstructures even if the third one is at the border of the image. The characteristic dimensions of the two structures are: A≈1300 nm, B≈1560 nm, H≈750 nm and A'≈1280 nm, B'≈ 1450 nm, H'≈750 nm. While the dimensions of the third are A≈2000 nm, B≈2160 nm and H≈2500nm.

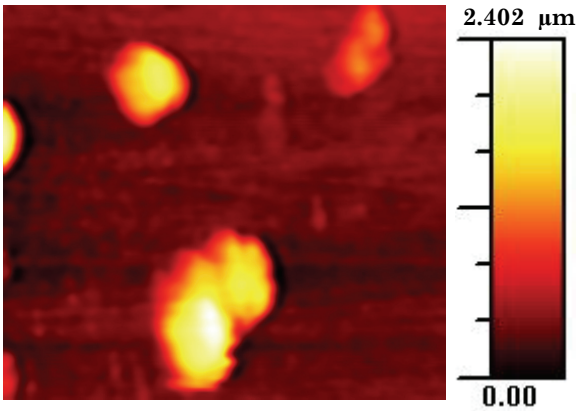

A: Sample S11new (8.8 µm x 7.8 µm)

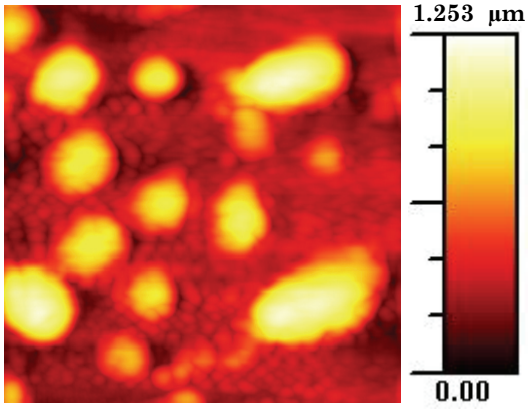

B: Sample S12 (10.0 µm x 10.0 µm)

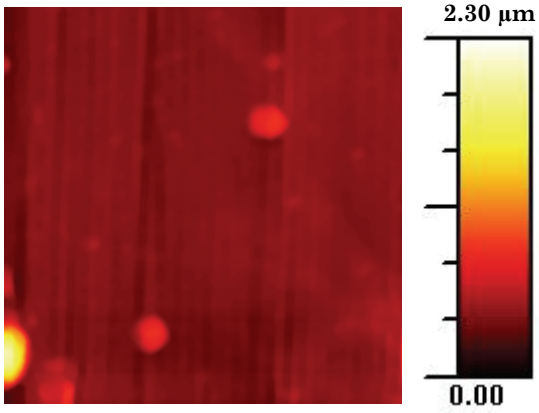

C: Sample S15 (14.0 µm x 14.0 µm)

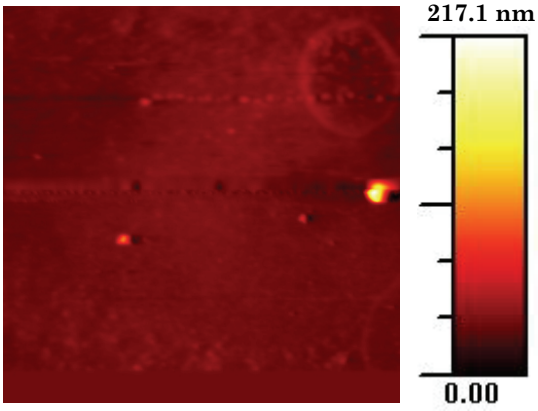

D: Sample S17 (15.0 µm x 15.0 µm)

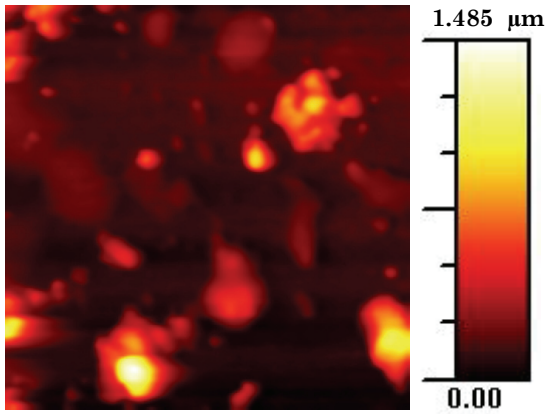

E: Sample S18 (12.0 µm x 12.0 µm)

Figure 5.17 AFM topographic images (two-dimensional view) of the first group of samples deposited with concentration 0.001 mol/l, before the annealing process.

Also sample S17 surface present only three relevant structure (see figure 5.17 D) whose dimension are: A≈420 nm, B≈480 nm, H≈30 nm; A'≈540 nm, B'≈ 650 nm, H'≈70 nm; A"≈990 nm, B"≈ 1030 nm, H"≈145 nm.

Sample S18 surface (see figure 5.17 E) is characterized by the presence of few isolated grains with no regular shape whose lateral dimensions are of the order few microns and the mean height is of the order of one micron.

Looking at figure 5.17 we can conclude that there is a common behaviour between the samples belonging to this first group: they present a surface characterized by a similar flat background (the range of z scale is, except for sample S17, of the same order of magnitude) and few isolated structures whose lateral dimensions ranges from 500 nm to few microns.

Sample P2 topography (see figure 5.18 A) is characterized by the presence of so many grains that cover uniformly the scanned region. The mean lateral dimension is about 310 nm, while the mean height is about 220 nm.

Sample S4 topography (see figure 5.18 B) is characterized by the presence of several bumps but with no regular shape. The major part of them have lateral dimensions smaller than 500 nm and a mean height of the order of 150 nm, while few others have mean lateral dimensions of the order of 1 μm and a mean height of 300 nm. There is only one microstructure whose characteristic dimensions are A≈1430 nm, B≈1900 nm and H≈450 nm.

Sample S6new topography (see figure 5.18 C) presents several structures of rectangular shape whose lateral dimensions a and b vary in the following range: $a \in (2.3 \div 3.4)$ μm, $b \in (3.4 \div 4.8)$ μm, while the average height is about 4.0 μm.

Figure 5.18 D represents sample S7 topography. It can be clearly seen that the sprayed layer is constituted by two main group of grains which have almost a regular round shape. A first group is characterized by mean lateral dimension of the order of 1300 nm and a mean height of the order of 300 nm and a second one with mean lateral dimension 700 nm and a mean height of about 230 nm.

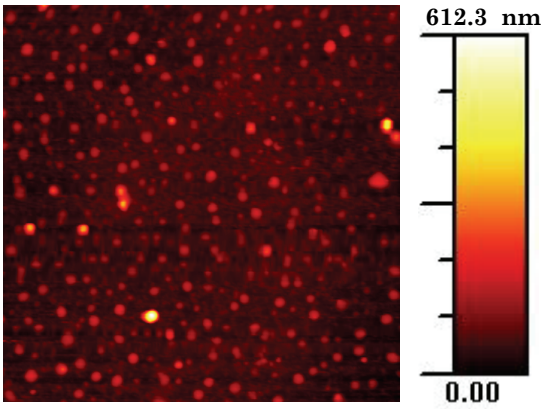

A: Sample P2 (12.9 µm x 12.9 µm)

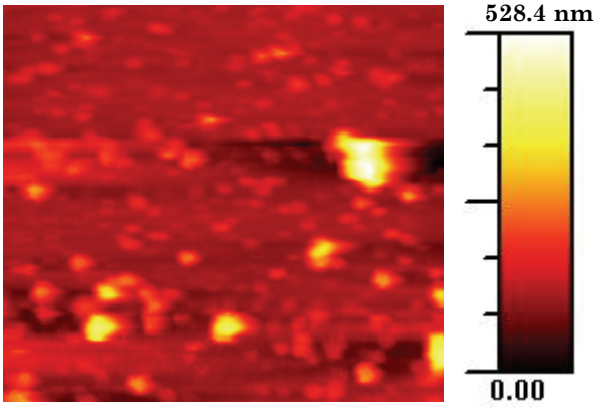

B: Sample S4 (11.5 µm x 10.4 µm)

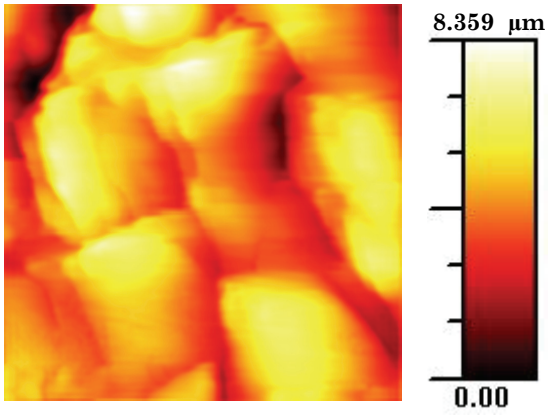

C: Sample S6new (9.05 µm x 9.0 µm)

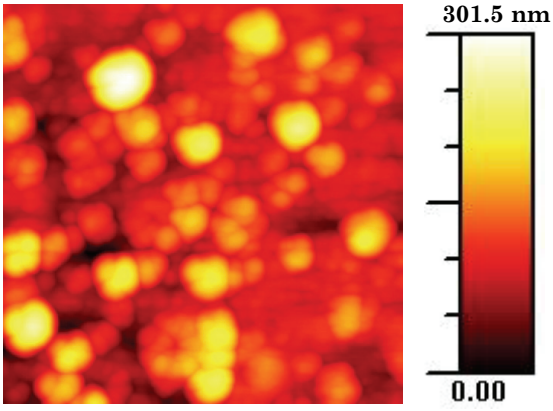

D: Sample S7 (10.0 µm x 10.0 µm)

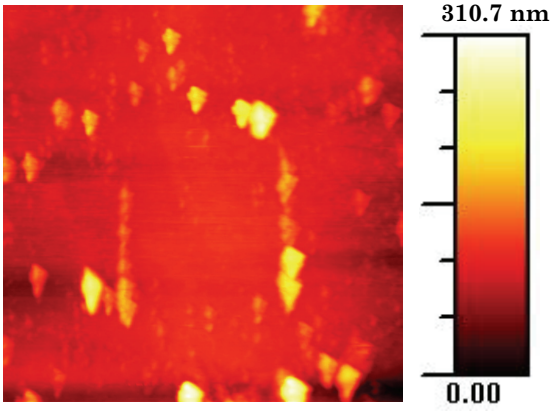

E: Sample S9 (13.0 µm x 13.0 µm)

Figure 5.18 AFM topographic images (two-dimensional view) of the second group of samples deposited with concentration 0.01 mol/l, before the annealing process.

From figure 5.18 E it is possible to see that sample S9 topography is very flat; in fact the average surface height is 95.11 nm and the RMS roughness (root mean square roughness) is 27.45 nm.
Looking at figure 5.18, excluding sample S6new and sample S9, we can conclude that increasing the metal chloride concentration it is possible to obtain a more structured surface morphology.
Regarding the samples S6new and S9, it is evident that we obtained very different topographic morphology even if the solution concentration was the same; probably this is due to the fact that, in the two cases, the fibre alignment with regards the spray direction changed in an uncontrolled way. For this reason, it is fundamental an improvement of the deposition technique that is currently on going in order to minimize the detrimental effects of unwanted misalignment during fibre positioning.

5.2.2 Effect of thermal annealing on sample morphology and optical near field

In this paragraph we will analyze the effect of thermal annealing on the same two groups of samples deposited with different metal chloride concentration:

- Concentration 0.001 mol/l: sample S12, sample S15, sample S17 and sample S18.
- Concentration 0.01 mol/l: sample P2, sample S4, sample S6new and sample S7.

Because the surface morphology before the annealing process was already described in the previous paragraph, we will now focalize the attention on the surface morphology after the annealing process and on its effect also on the collected near field intensity distribution.

Sample S12

In figure 5.19 we report the AFM image (left) of the sample S12 topography and the near field intensity distribution simultaneously collected (right), before the annealing process. The image refers to a 10.0 μm x 10.0 μm area, approximately centred on the optical fibre core.

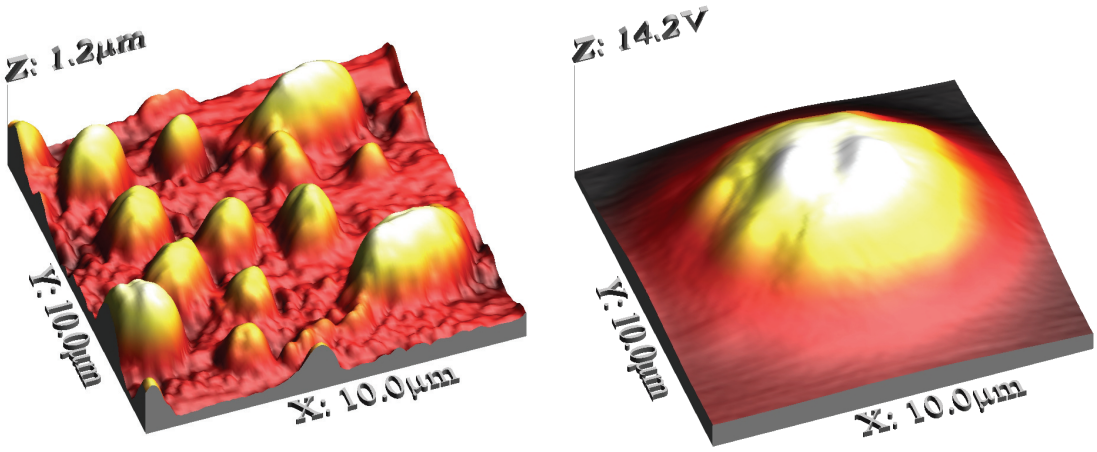

Figure 5.19 Three-dimensional view of the AFM topography image (left) and radiation intensity simultaneously collected by the SNOM probe (right) before thermal annealing on sample S12.

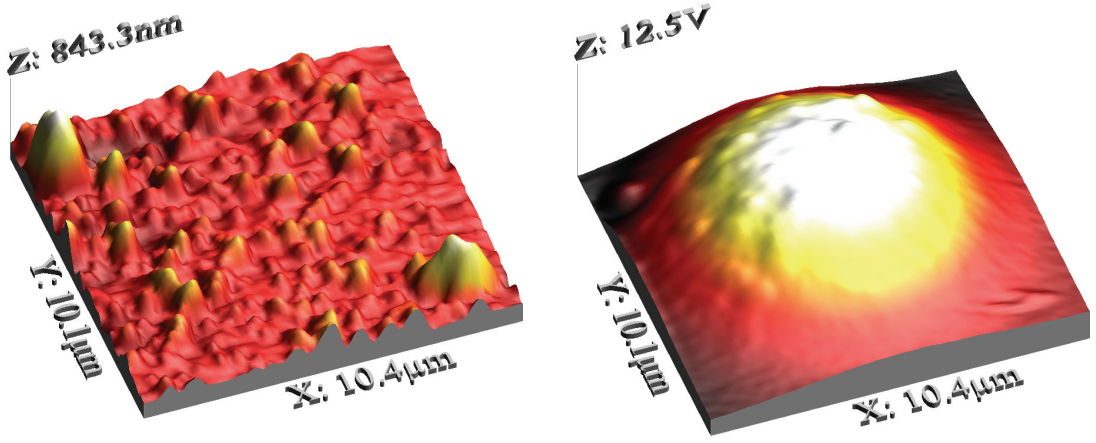

Figure 5.20 Three-dimensional view of the AFM topography image (left) and radiation intensity simultaneously collected by the SNOM probe (right) after thermal annealing on sample S12.

In figure 5.20 we report the AFM image (left) of the sample S12 topography and the near field intensity distribution simultaneously collected (right), after the annealing process. The image refers to a 10.4 μm x 10.1 μm area, approximately centred on the optical fibre core.

As it is possible to note in figure 5.20 (left), the large structures present on the S12 sample topography before the thermal treatment (figure 5.19 left), was been transformed into small grains whose average dimensions are: $\overline{A} \cong$ 700 nm, $\overline{B} \cong 1.1$ μm, $\overline{H} \cong 350$ nm.

In order to have additional information about the effect of annealing process on the sample topography we also analyzed the distribution of the heights (see figure 5.21) in the two images reported in figures 5.19 and 5.20 (left).

We found: an average surface height of 43.7 nm and a RMS roughness of 248.5 nm before annealing; while an average surface height of 231.70 nm and a RMS roughness of 54.19 nm after annealing. In this case the RMS roughness after the annealing is slightly decreased.

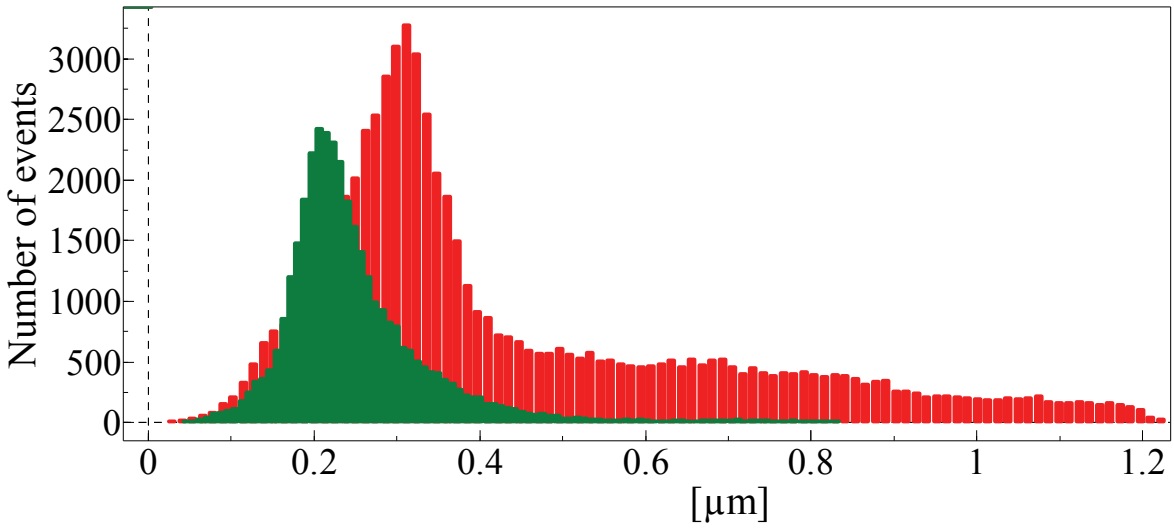

Figure 5.21 Histograms of the heights relative to the scanned area of sample S12 before (red) and after (green) the annealing process.

Sample S15

In figure 5.22 we report the AFM image (left) of the sample S15 topography and the near field intensity distribution simultaneously collected (right), before the annealing process. The image refers to a 14.0 μm x 14.0 μm area, approximately centred on the optical fibre core.

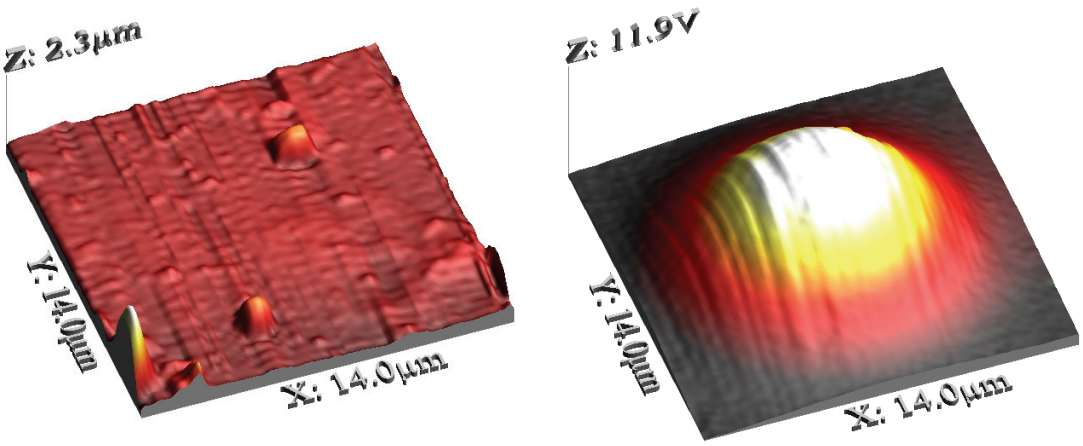

Figure 5.22 Three-dimensional view of the AFM topography image (left) and radiation intensity simultaneously collected by the SNOM probe (right) before thermal annealing on sample S15.

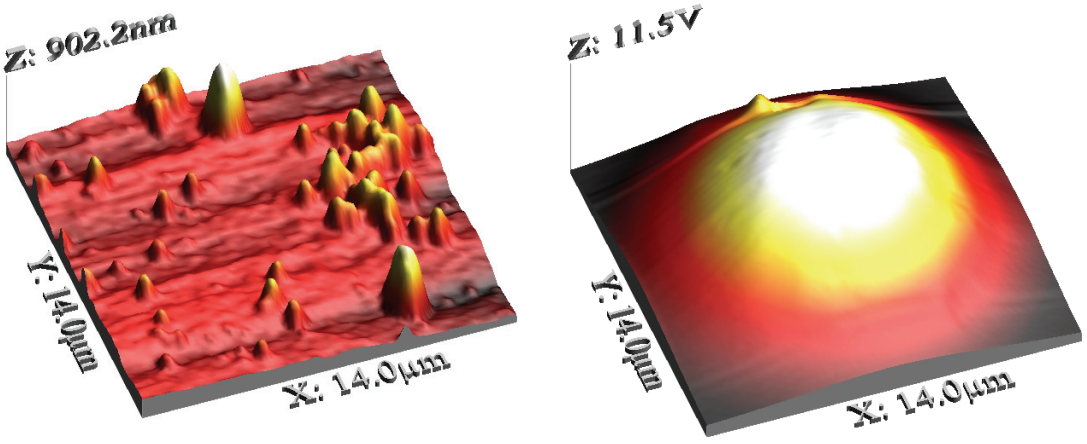

Figure 5.23 Three-dimensional view of the AFM topography image (left) and radiation intensity simultaneously collected by the SNOM probe (right) after thermal annealing on sample S15.

In figure 5.23 we report the AFM image (left) of the sample S15 topography and the near field intensity distribution simultaneously collected (right), after the annealing process. The image refers to a 14.0 μm x 14.0 μm area, approximately centred on the optical fibre core.

From the image 5.23 (left) it is clear that the deposited layer is almost flat characterized by the presence of small grains whose lateral dimensions are of the order of 750 nm and a mean height of about 350 nm.

From figure 5.23 (right) it is possible to note that the optical near field collected on the sample surface is not influenced by the presence of such SnO_2 layer; in fact the Gaussian profile is slightly perturbed only in correspondence of one SnO_2 grain.

In order to have additional information about the effect of annealing process on the sample topography we also analyzed the distribution of the heights (see figure 5.24) in the two images reported in figures 5.22 and 5.23 (left).

We found: an average surface height of 473.6 nm and a RMS roughness of 136.5 nm before annealing; while an average surface height of 193.7 nm and a RMS roughness of 105.4 nm after annealing. In this case the RMS roughness after the annealing is of the same order of magnitude.

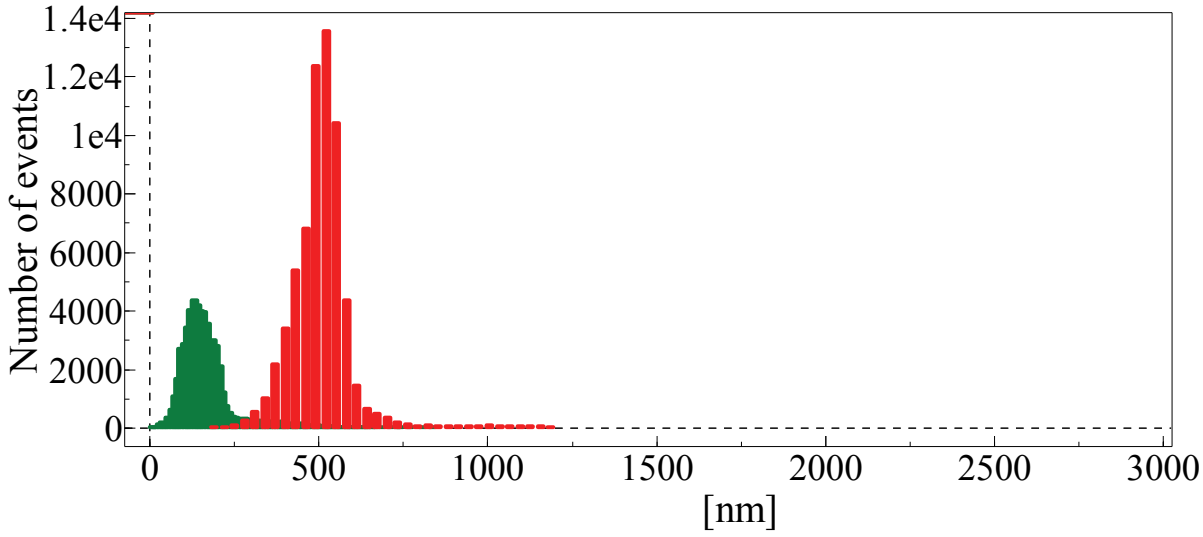

Figure 5.24 Histograms of the heights relative to the scanned area of sample S15 before (red) and after (green) the annealing process.

Sample S17

In figure 5.25 we report the AFM image (left) of the sample S17 topography and the near field intensity distribution simultaneously collected (right), before the annealing process. The image refers to a 15.0 μm x 15.0 μm area, approximately centred on the optical fibre core.

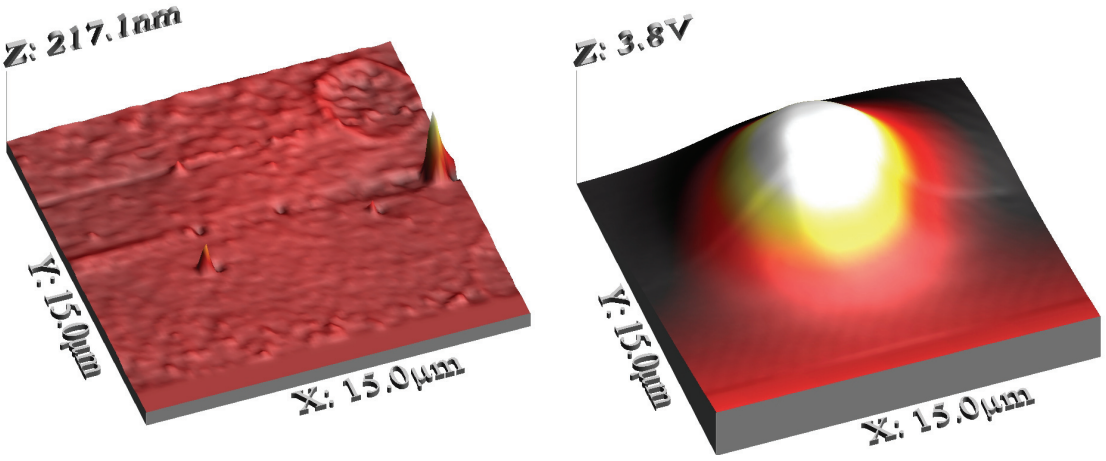

Figure 5.25 Three-dimensional view of the AFM topography image (left) and radiation intensity simultaneously collected by the SNOM probe (right) before thermal annealing on sample S17.

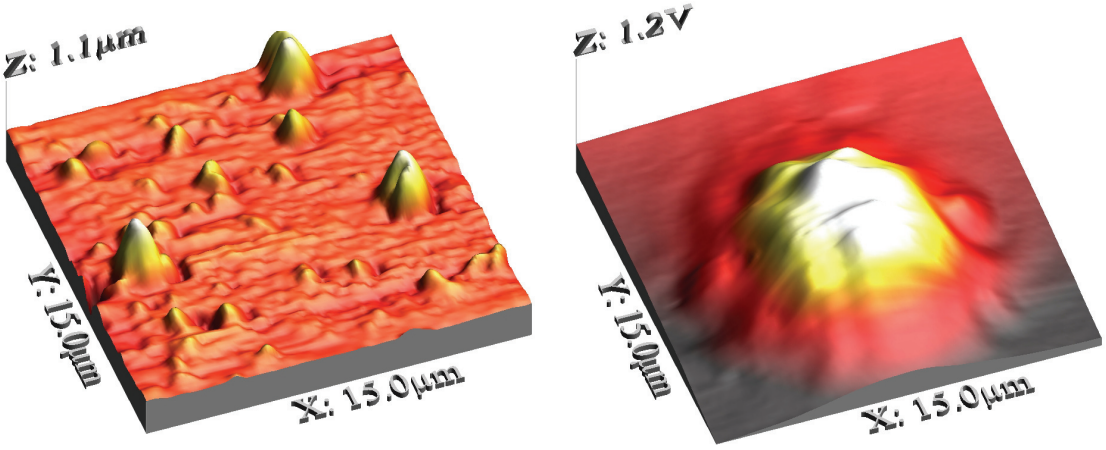

Figure 5.26 Three-dimensional view of the AFM topography image (left) and radiation intensity simultaneously collected by the SNOM probe (right) after thermal annealing on sample S17.

In figure 5.26 we report the AFM image (left) of the sample S15 topography and the near field intensity distribution simultaneously collected (right), after the annealing process. The image refers to a 15.0 μm x 15.0 μm area, approximately centred on the optical fibre core.

From the image 5.26 (left) it is possible to see that the deposited layer is characterized by the presence of several small grains and three bigger ones. The lateral dimensions of the smaller grains are of the order of 1200 nm and the mean height is about 250 nm; while the lateral dimensions of the bigger grains are about 1950 nm and the mean height is about 800 nm.

From figure 5.26 (right) it is possible to note how the optical near field is influenced by the presence of the aforementioned SnO_2 grains; in fact the Gaussian profile is perturbed in between the SnO_2 grains.

In order to have additional information about the effect of annealing process on the sample topography we also analyzed the distribution of the heights (see figure 5.27) in the two images reported in figures 5.25 and 5.26 (left).

We found: an average surface height of 35.46 nm and a RMS roughness of 6.20 nm before annealing; while an average surface height of 439.60 nm and a RMS roughness of 83.35 nm after annealing. In this case the RMS roughness after the annealing is increased of one order of magnitude.

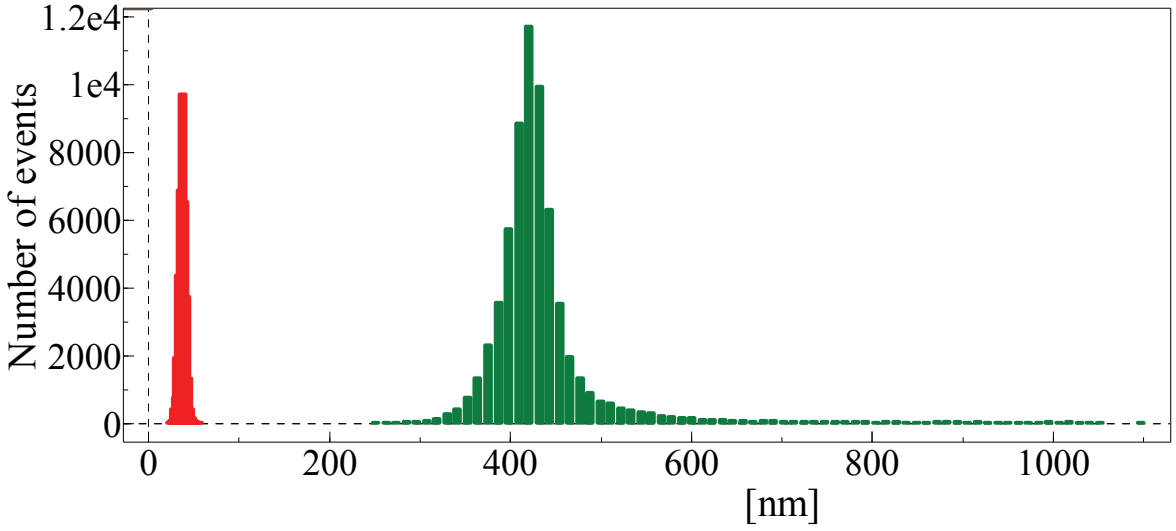

Figure 5.27 Histograms of the heights relative to the scanned area of sample S17 before (red) and after (green) the annealing process.

Sample S18

In figure 5.28 we report the AFM image (left) of the sample S18 topography and the near field intensity distribution simultaneously collected (right), before the annealing process. The image refers to a 12.0 μm x 12.0 μm area, approximately centred on the optical fibre core.

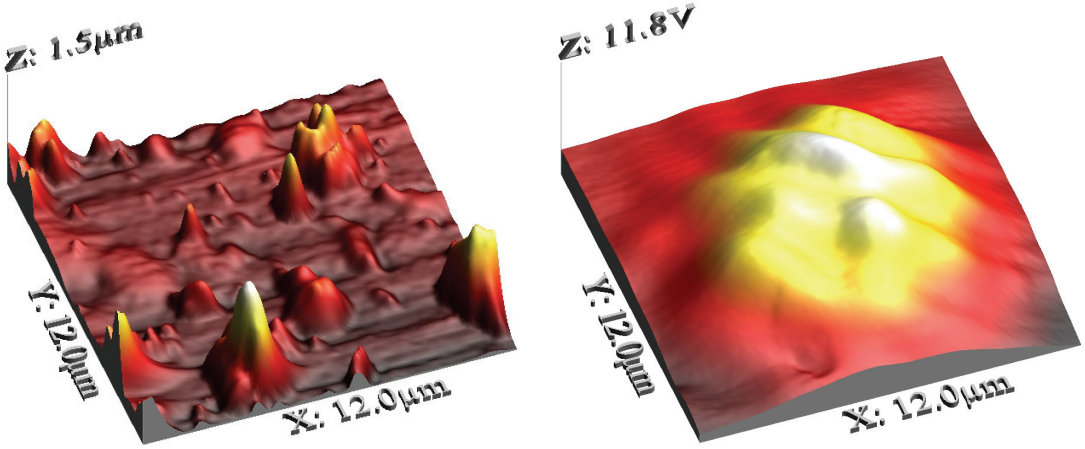

Figure 5.28 Three-dimensional view of the AFM topography image (left) and radiation intensity simultaneously collected by the SNOM probe (right) before thermal annealing on sample S18.

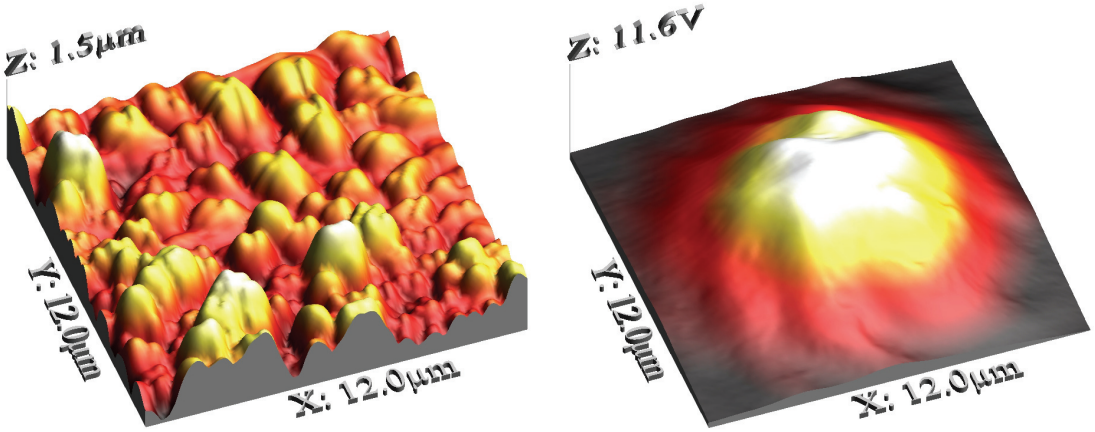

Figure 5.29 Three-dimensional view of the AFM topography image (left) and radiation intensity simultaneously collected by the SNOM probe (right) after thermal annealing on sample S18.

In figure 5.29 we report the AFM image (left) of the sample S18 topography and the near field intensity distribution simultaneously collected (right), after the annealing process. The image refers to a 12.0 μm x 12.0 μm area, approximately centred on the optical fibre core.

It can be clearly seen from figure 5.29 (left) that the SnO_2 layer after the thermal treatment is constituted by two main group of grains which have approximately the shape of an half ellipsoid. A first group is characterized by mean axes dimension ranging from 850 nm to 1.8 μm and a second one with mean axes dimension ranging from 1.5 μm to 3.5 μm.

From figure 5.29 (right) it is possible to note how the optical near field is influenced by the presence of the aforementioned SnO_2 grains; in fact the Gaussian profile is perturbed in between the SnO_2 grains.

In order to have additional information about the effect of annealing process on the sample topography we also analyzed the distribution of the heights (see figure 5.30) in the two images reported in figures 5.28 and 5.29 (left).

We found: an average surface height of 195.6 nm and a RMS roughness of 173.5 nm before annealing; while an average surface height of 653.8 nm and a RMS roughness of 206.2 nm after annealing. In this case the RMS roughness after the annealing is of the same order of magnitude.

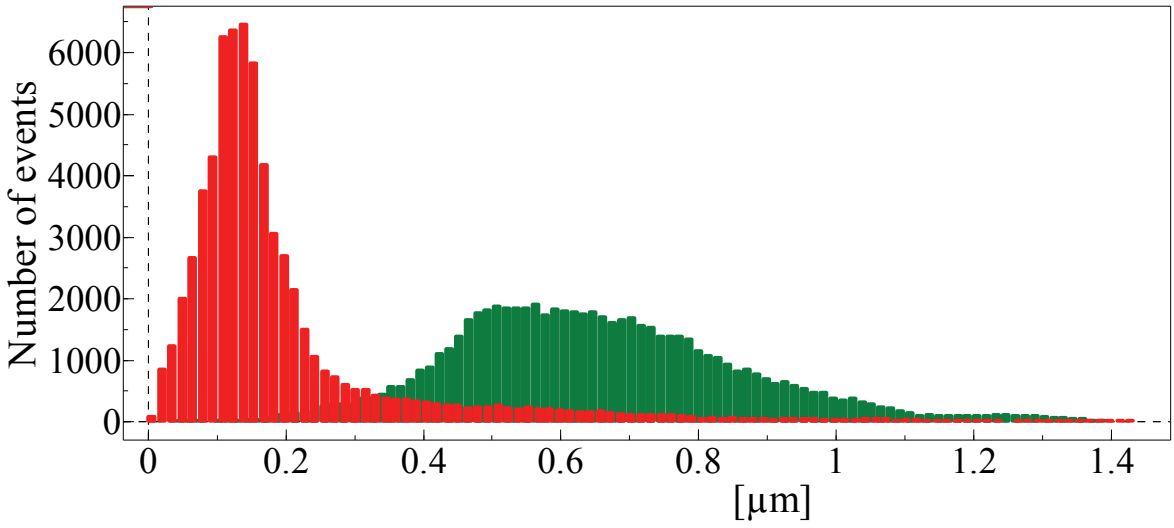

Figure 5.30 Histograms of the heights relative to the scanned area of sample S18 before (red) and after (green) the annealing process.

Sample P2

In figure 5.31 we report the AFM image (left) of the sample P2 topography and the near field intensity distribution simultaneously collected (right), before the annealing process. The image refers to a 12.9 μm x 12.9 μm area, approximately centred on the optical fibre core.

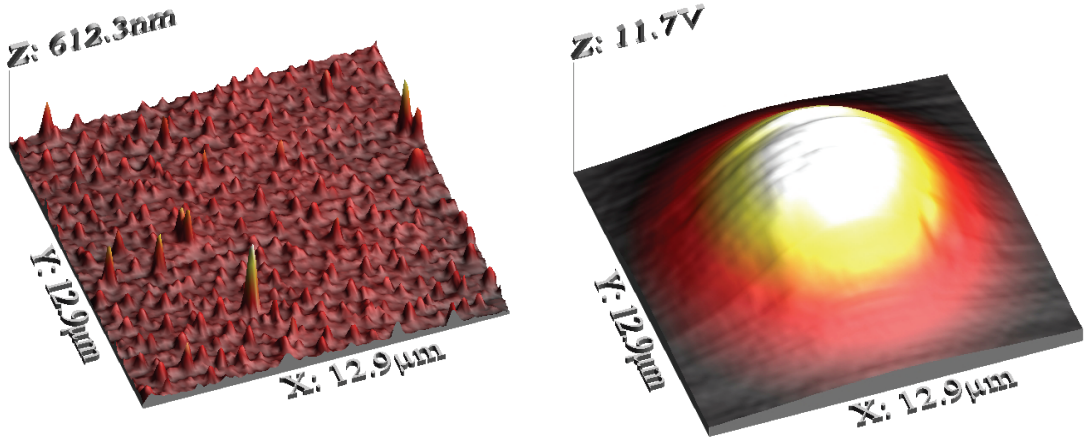

Figure 5.31 Three-dimensional view of the AFM topography image (left) and radiation intensity simultaneously collected by the SNOM probe (right) before thermal annealing on sample P2.

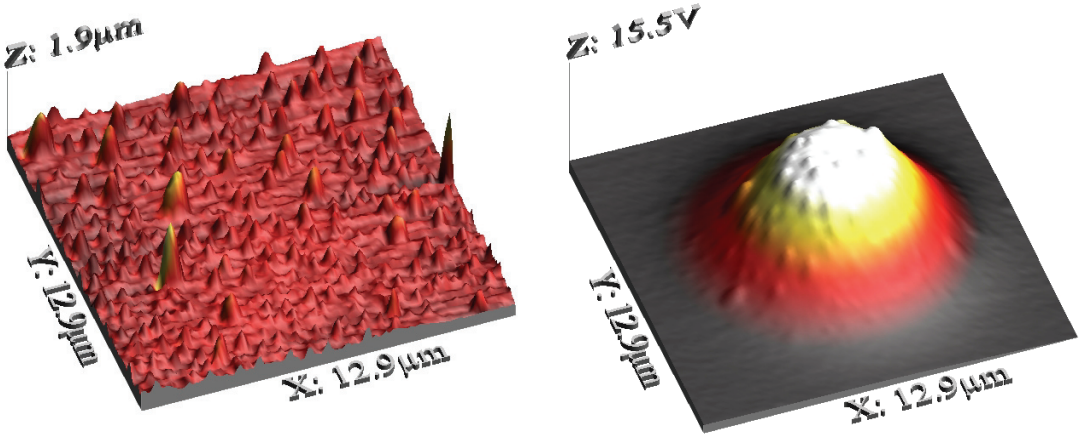

Figure 5.32 Three-dimensional view of the AFM topography image (left) and radiation intensity simultaneously collected by the SNOM probe (right) after thermal annealing on sample P2.

In figure 5.32 we report the AFM image (left) of the sample P2 topography and the near field intensity distribution simultaneously collected (right), after the annealing process. The image refers to a 12.9 μm x 12.9 μm area, approximately centred on the optical fibre core. It reveals the presence of several SnO_2 grains. In order to obtain quantitative information about these grains we analyzed the distribution of the bumps heights and sizes in a squared region strictly containing the core region (because we are interested to those grains able to perturb the emerging field). The distribution of bumps size revealed the presence of about 183 SnO_2 bumps, covering about 14% of the total area, as reported in figure 5.33. Supposing the bumps have a circular base, from the mean area it is possible to derive the mean radius and so the mean lateral dimension: $x \approx y \approx 465$nm.

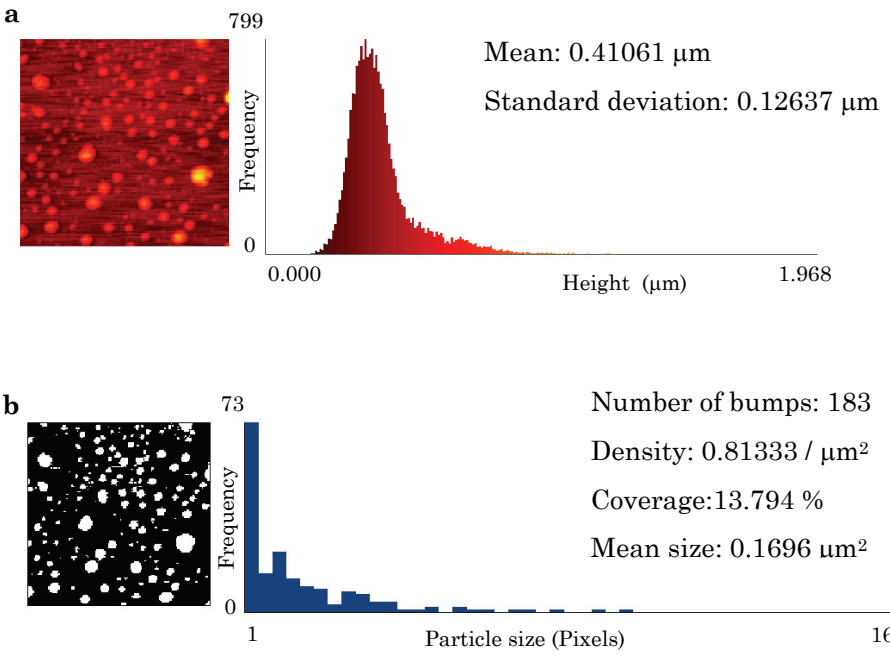

Figure 5.33 Histogram of the heights relative to a squared region strictly containing the core region of the sample P2 (a) and analysis of bumps present in the same region (b).

Figure 5.32 (right) demonstrate that in correspondence of the biggest bumps there is a light diffraction effect and thus a modification of the near field profile transmitted through the optical fibre coating.

In this case, the bumps have a mean height of about 700 nm and a mean width of about 550 nm. In fact, it can be clearly observed how the typical Gaussian shape of the fundamental mode propagating through the single-mode optical fibre is modified in correspondence of these SnO_2 peaks. As said in the previous paragraphs, this can be justified by considering the high refractive index of the SnO_2 (approx. 1.967 at λ=1550 nm) bumps which in turn try to guide the light. However, the lateral dimensions and the bumps spacing (mean bumps spacing is about 1 μm) are too small to allow a correct light localization due to the significant overlap of the evanescent field.

We finally analyzed the distribution of the heights (see figure 5.34) in the two images reported in figures 5.31 and 5.32 (left). We found: an average surface height of 62.34 nm and a RMS roughness of 31.45 nm before annealing; while an average surface height of 386.62 nm and a RMS roughness of 137.50 nm after annealing. In this case the RMS roughness after the annealing is increased of one order of magnitude.

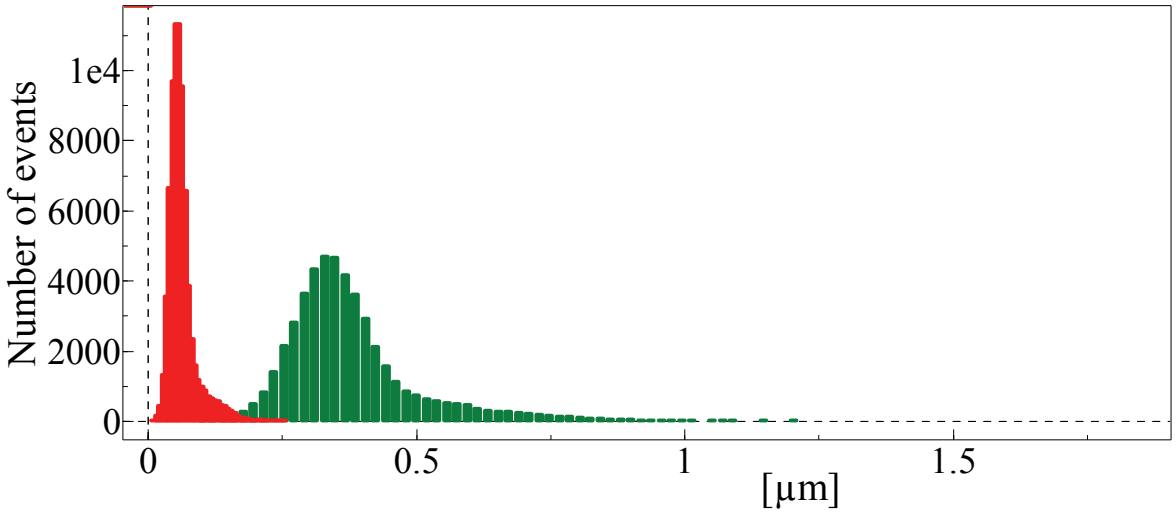

Figure 5.34 Histograms of the heights relative to the scanned area of sample P2 before (red) and after (green) the annealing process.

Sample S4

In figure 5.35 we report the AFM image (left) of the sample S4 topography and the near field intensity distribution simultaneously collected (right), before the annealing process. The image refers to a 11.5 μm x 10.4 μm area, approximately centred on the optical fibre core.

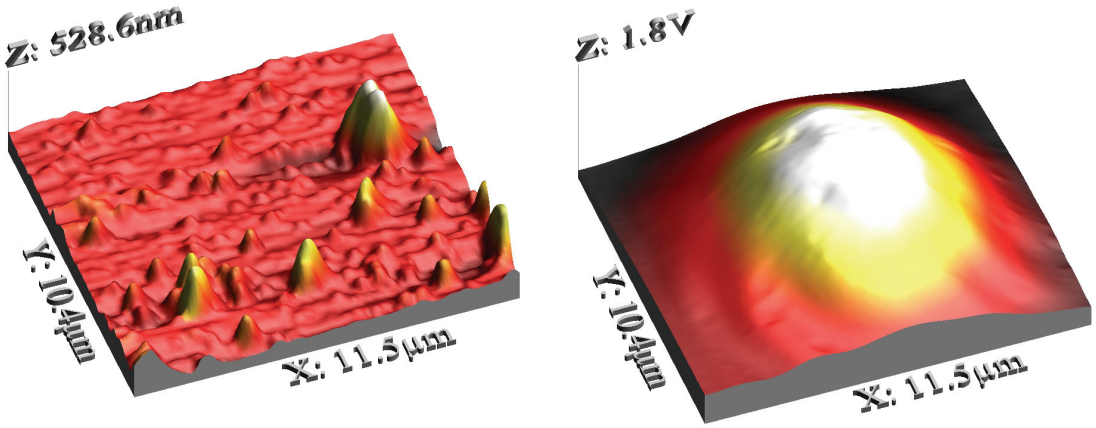

Figure 5.35 Three-dimensional view of the AFM topography image (left) and radiation intensity simultaneously collected by the SNOM probe (right) before thermal annealing on sample S4.

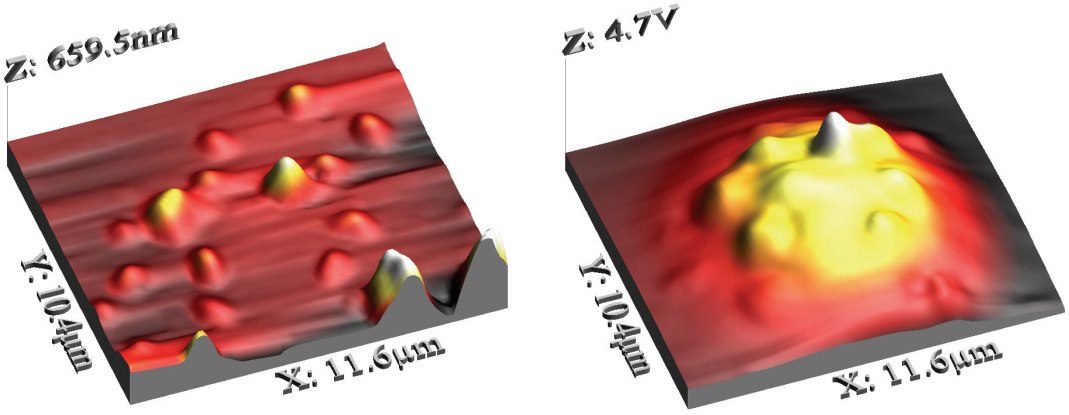

Figure 5.36 Three-dimensional view of the AFM topography image (left) and radiation intensity simultaneously collected by the SNOM probe (right) after thermal annealing on sample S4.

In figure 5.36 we report the AFM image (left) of the sample S4 topography and the near field intensity distribution simultaneously collected (right), after the annealing process. The image refers to a 11.6 μm x 10.4 μm area, approximately centred on the optical fibre core. As observable, the surface morphology reveal the presence of several microstructures well separated from each other, whose dimensions are reported in the paragraph 5.1.2. As described before, the presence of such microstructures strongly modify the collected near field intensity, as it possible to see in figure 5.36 (right).

In order to have additional information about the effect of annealing process on the sample topography we also analyzed the distribution of the heights (see figure 5.37) in the two images reported in figures 5.35 and 5.36 (left).

We found: an average surface height of 134.81 nm and a RMS roughness of 48.91 nm before annealing; while an average surface height of 231.70 nm and a RMS roughness of 54.19 nm after annealing. In this case the RMS roughness before and after the annealing is of the same order of magnitude.

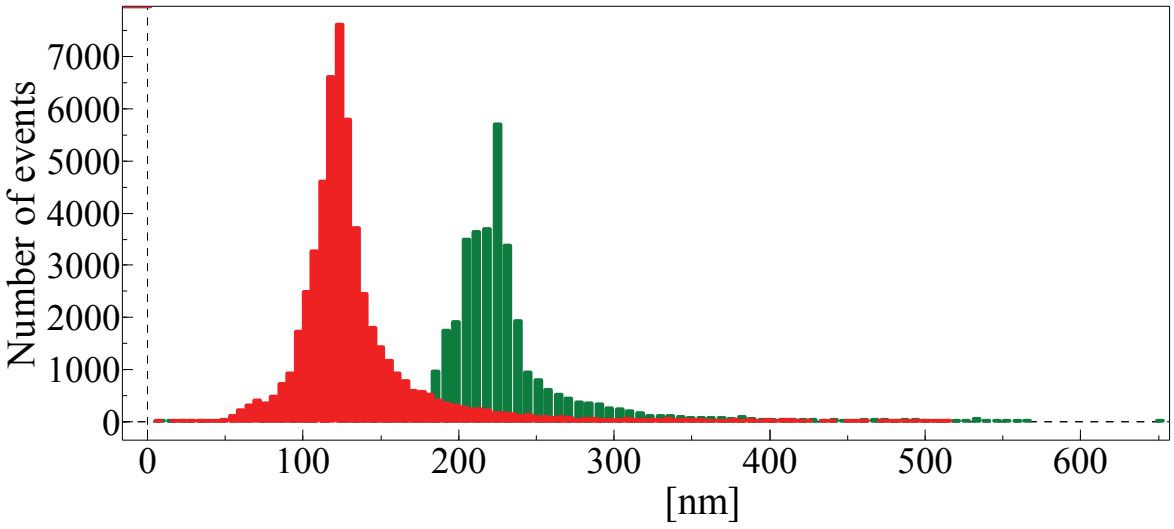

Figure 5.37 Histograms of the heights relative to the scanned area of sample S4 before (red) and after (green) the annealing process.

Sample S6new

In figure 5.38 we report the AFM image (left) of the sample S6new topography and the near field intensity distribution simultaneously collected (right), before the annealing process. The image refers to a 9.0 μm x 9.0 μm area, approximately centred on the optical fibre core.

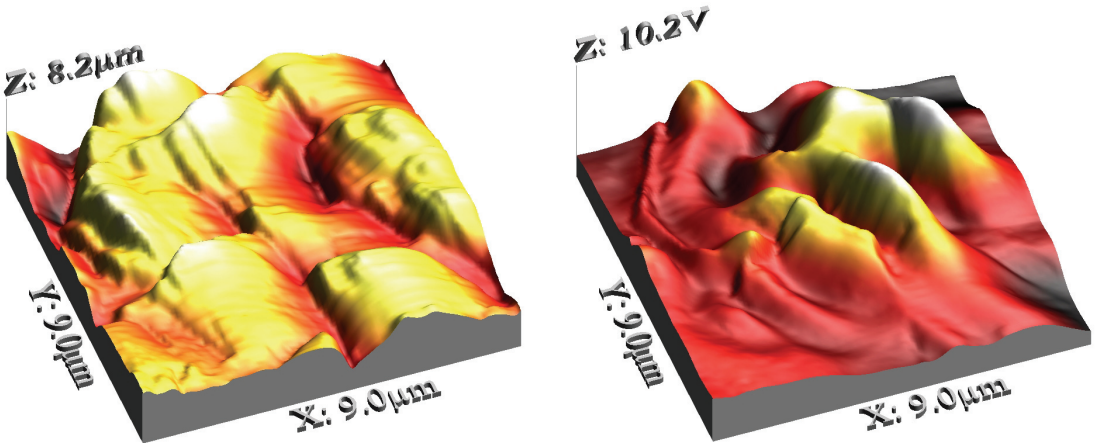

Figure 5.38 Three-dimensional view of the AFM topography image (left) and radiation intensity simultaneously collected by the SNOM probe (right) before thermal annealing on sample S6new.

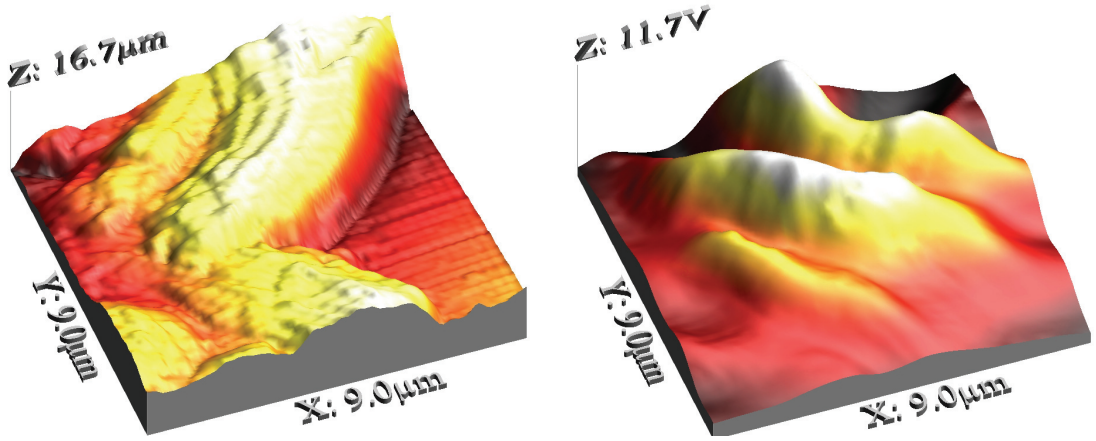

Figure 5.39 Three-dimensional view of the AFM topography image (left) and radiation intensity simultaneously collected by the SNOM probe (right) after thermal annealing on sample S6new.

In figure 5.39 we report the AFM image (left) of the sample S6new topography and the near field intensity distribution simultaneously collected (right), after the annealing process. The image refers to a 9.0 μm x 9.0 μm area, approximately centred on the optical fibre core. As observable, the surface morphology mainly consists of two elongated structures with mean lateral dimensions (3.6x4.1) μm, (3.3x8.3) μm and average height about 8.0 μm and 13.5 μm respectively.

Moreover, it can be seen that the structures are formed by aggregating grains with mean lateral dimensions less than 1 μm. From figure 5.39 (right), the strong modifications of the emergent near-field profile induced by the aforementioned morphology can be clearly appreciated.

We finally analyzed the distribution of the heights (see figure 5.40) in the two images reported in figures 5.38 and 5.39 (left). We found: an average surface height of 4.431 μm and a RMS roughness of 1.313 μm before annealing; while an average surface height of 8.847 μm and a RMS roughness of 3.487 μm after annealing. In this case the RMS roughness after the annealing became three times higher.

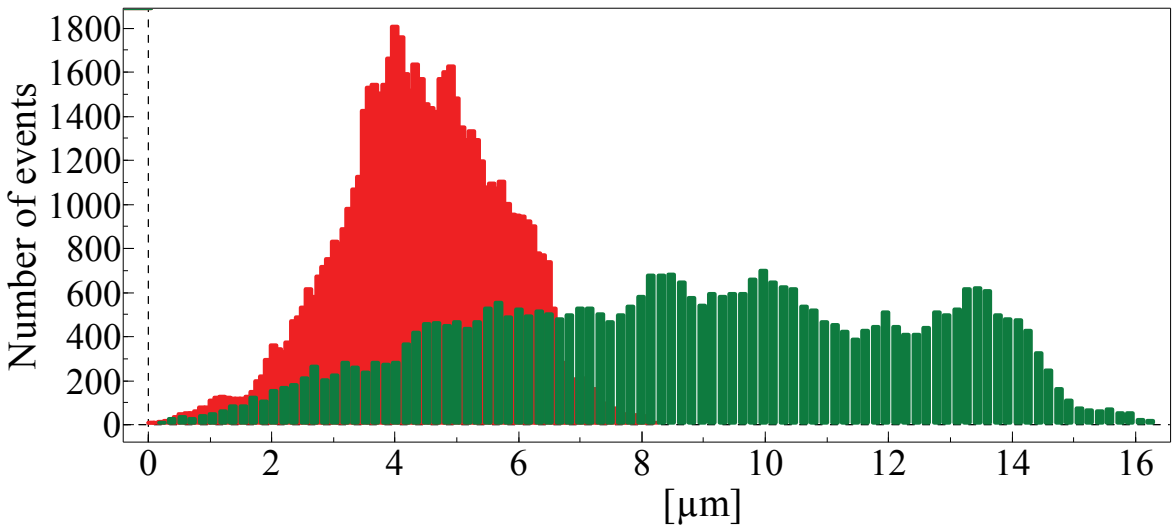

Figure 5.40 Histograms of the heights relative to the scanned area of sample S6new before (red) and after (green) the annealing process.

Sample S7

In figure 5.41 we report the AFM image (left) of the sample S7 topography and the near field intensity distribution simultaneously collected (right), before the annealing process. The image refers to a 10.0 μm x 10.0 μm area, approximately centred on the optical fibre core.

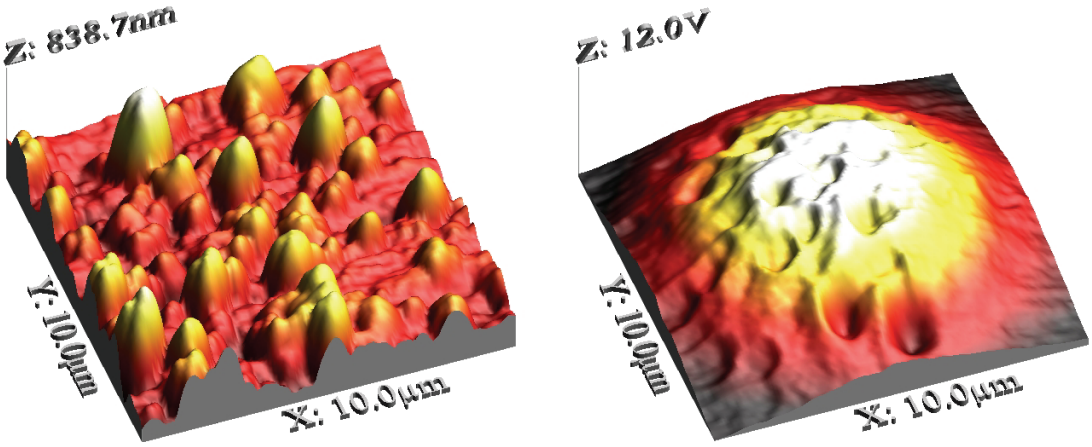

Figure 5.41 Three-dimensional view of the AFM topography image (left) and radiation intensity simultaneously collected by the SNOM probe (right) before thermal annealing on sample S7.

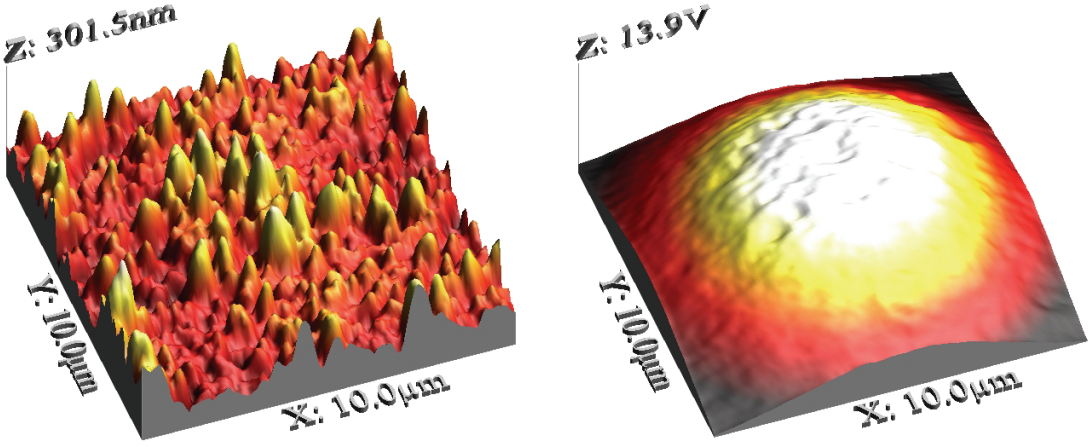

Figure 5.42 Three-dimensional view of the AFM topography image (left) and radiation intensity simultaneously collected by the SNOM probe (right) after thermal annealing on sample S7.

In figure 5.42 we report the AFM image (left) of the sample S7 topography and the near field intensity distribution simultaneously collected (right), after the annealing process. The image refers to a 10.0 μm x 10.0 μm area, approximately centred on the optical fibre core.

It can be clearly seen from figure 5.42 (left) that the SnO_2 layer after the thermal treatment is constituted by a lot of grains whose mean dimensions are smaller than that of grains present on the surface before annealing.

Comparing figures 5.41 and 5.42 (right) it is possible to note that in this case the optical near field less influenced by the presence of the post annealing SnO_2 grains.

In order to have additional information about the effect of annealing process on the sample topography we also analyzed the distribution of the heights (see figure 5.43) in the two images reported in figures 5.41 and 5.42 (left).

We found: an average surface height of 313.2 nm and a RMS roughness of 118.7 nm before annealing; while an average surface height of 110.0 nm and a RMS roughness of 39.6 nm after annealing. In this case the RMS roughness after the annealing is slightly decreased.

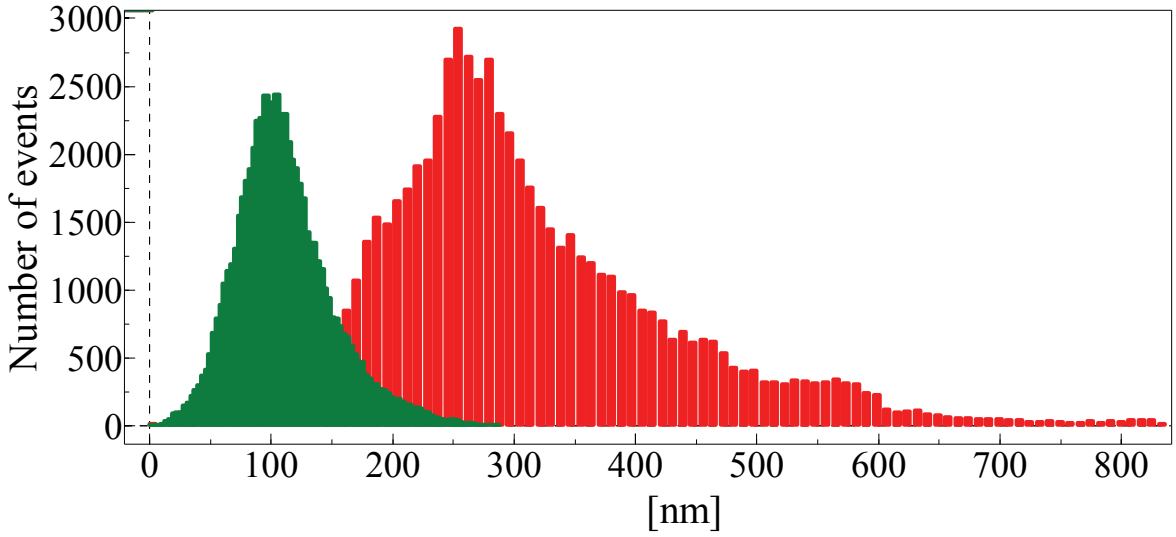

Figure 5.43 Histograms of the heights relative to the scanned area of sample S7 before (red) and after (green) the annealing process.

5.3 Topography modification by mean of UV irradiation

This experimental section was inspired by the search of a methodology to produce the desired SnO_2 structures able to enhance the near field.

As a matter of the fact, studies carried out in the past about the optical properties of tin dioxide showed that absorption region of SnO_2 films lies in the wavelength range as low as 250 – 300 nm, while in the VIS and NIR wavelength range it results to be transparent [3].

Therefore we wanted to investigate if the adsorption of the UV radiation can lead some change in the polycristalline arrangement of SnO_2 films and thus in the surface morphology.

In this paragraph we will show some preliminary results about the real possibility to locally modify the surface morphology of an SnO_2 film by mean of UV irradiation performed through the AFM-SNOM system.

To this aim it was employed a pig-tailed He-Cd laser whose operation wavelength is 325 nm, with a maximum output power of 500 mW. The UV laser radiation was properly coupled to a multimodal optical fibre (200-1200 nm with core diameter 200 μm) SNOM probe (see figure 5.44) whose terminal optical aperture is 200 nm (while the whole terminal diameter is 350 nm because of the metallization layer). The power coupled to the SNOM probe was decreased to about 100 mW in order to prevent damage of the probe aperture caused by thermal effect; in fact a probe with optical aperture 200 nm can be burnt by radiation with input power major than 200 mW.

In this way, using the scanning probe system with an appropriate SNOM tip, it became possible select a precise spatial region, to observe the film topography, to perform the UV irradiation and then to observe again the topography.

We want to stress that, the experiment we are describing would have been impossible without the use of the complex scanning probe system described into the chapter 4, that allows to perform both AFM and SNOM measurement using the same tip.

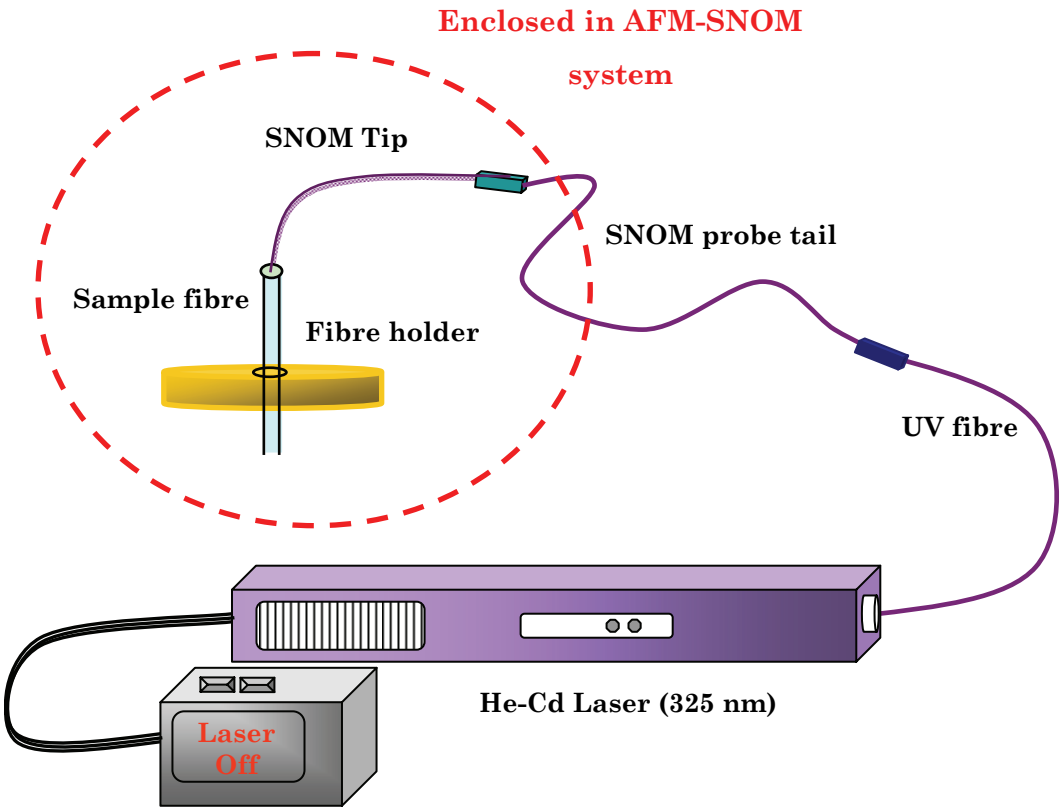

Figure 5.44 Experimental set-up employed for UV irradiation.

The experiments was led according to the following steps.

First of all, it was performed a map of the layer topography in a certain spatial region taking the laser off. After that we selected a smaller region that contained some SnO_2 grains and performed a new topographic map in order to have a better resolution of the selected features. The last one will be our reference topography before illuminating. At this point, we switched on the laser and, without changing anything, we scanned again all the previous spatial region in order to irradiate by the SNOM probe the selected SnO_2 structures. Finally, we turned off the laser and scanned once a time the same region in order to have a topographic map that can be compared with the reference one in order to evaluate if there was an effect due to UV irradiation. This procedure was repeated several times in order to follow the

variations of the topography by changing the illumination time (that is the scan time point by point).

The investigated SnO_2 film (sample S5) was obtained using a solution volume of 5 ml and a concentration of 0.01 mol/l. In figure 5.45 A) we report an optical image of the whole surface layer deposited as usual onto the distal end of an optical fibre, captured by the CCD camera.

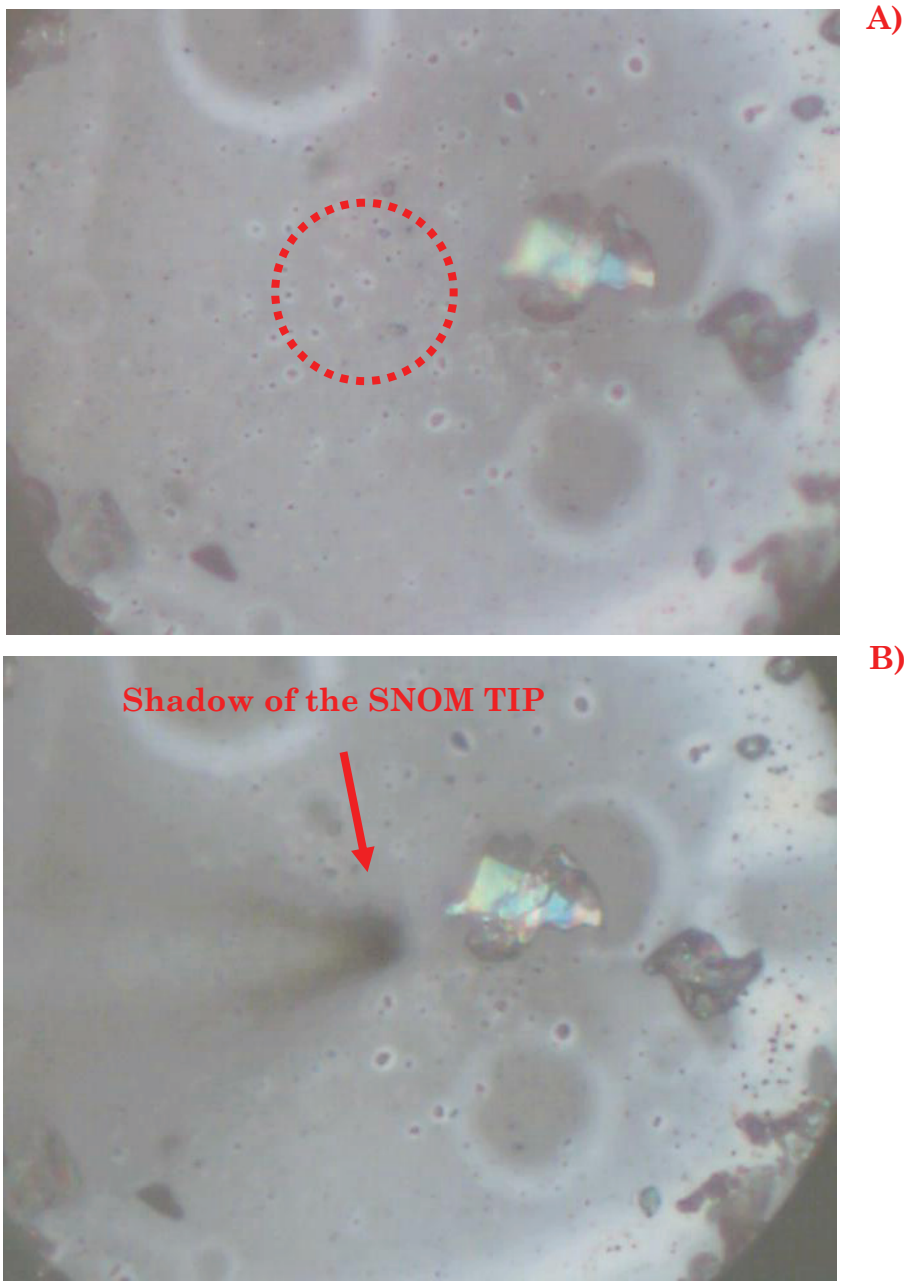

Figure 5.45 Optical image of the sample S5, made by a CCD camera (A) and relative position of the SNOM probe on its surface.

We described in the previous chapter the system arrangement that allows the SNOM head to be mounted at the specimen stage location, with a long working distance objective (50 X) positioned above the stage. In this way the probe can be guided effectively to the chosen scanning area by the objective and the CCD camera, because the probe itself easily fits under such objective without obscuring the far-field view through the lens. In figure 5.45 B) it is possible to see the shadow of the SNOM tip guided in such a way to scan an area far from the borders and free from large particles (like the iridescent one). The investigated area is enclosed into the red circle showed in figure 5.45 A).

In figure 5.46 we report the two-dimensional view of AFM images relative to the first sequence of test performed on a spatial region of 2 μm x 2 μm. Figure 5.46 A) shows the reference topography before illuminating; the blue arrows indicates the SnO_2 grain that will be investigated. This spatial region was irradiated four times (varying the illumination time from 7 ms to 20 ms) and after each irradiation the topography was been imaged. As it can be clearly seen in the sequence of figures 5.46 the afore mentioned SnO_2 grain vary its morphology both in dimensions and shape. In order to follow its variation we used the symbols A, B and H to indicate its characteristic dimensions: the minor axis, the major axis and the mean height respectively. In the table below we report these value refferring to each image.

	RMS Roughness (nm)	Mean Height (nm)	Minor axis (nm)	Major axis (nm)	Mean height (nm)
A)	26.9	66.5	282	318	65
B) 7 ms	30.4	77.2	353	410	65
C) 7 ms	30.8	88.6	326	503	70
D) 20 ms	32.6	109.6	284	522	75
E) 20 ms	30.8	84.5	301	429	75

Table 5.1 Topographic value relative to the AFM image 5.46.

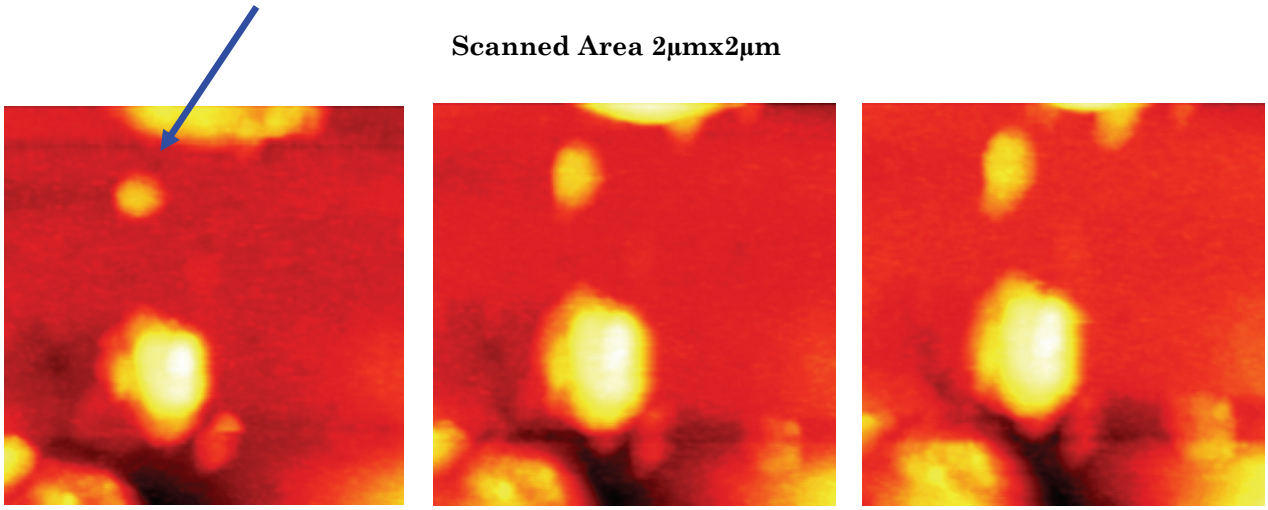

A) Reference Image
Zmax= 200.9 nm

B) First Irradiation (7ms)
Zmax= 226.3 nm

C) Second Irradiation (7ms)
Zmax= 231.0 nm

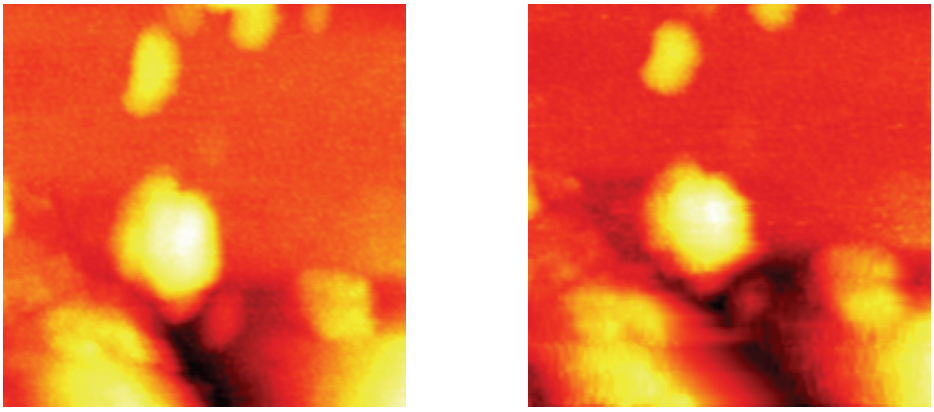

D) Third Irradiation (20 ms)
Zmax= 250.2 nm

E) Fourth Irradiation (20 ms)
Zmax= 208.7 nm

Figure 5.46 AFM images relative to sequencial irradiation: A) reference topography without radiation; B), C), D), E) topography after the first, the second, the third and the fourth irradiation respectively.

The reference shape is almost round, while after the irradiation it assumes a lengthened shape. From the values reported in the table 5.1 it is possible to see that the in some cases the structure dimensions encrease and in some others they decrease; this is due, of course, to the fact that also the flat background around the grain is changing because of the UV irradiation. In

the table 5.1 we reported also some data refferring to the whole scanned area: the root mean square roughness and the mean height. It can be clearly seen that the roughness changes only of few nanometers.

In this first experiment the maximum increase in the grain dimensions is about 100 nm (in correspondence of the first irradiation).

So, in the following experiment we decided to irradiate only two times with an increased time exposure of 15 ms for singol point. In figure 5.47 we report the two-dimensional view of AFM images relative to the second sequence of test performed on a spatial region of 1.9 μm x 1.9 μm. As it can be clearly seen from figures 5.47 the structures present in the reference image vary their morphology both in dimensions and shape. In this case is more evident not only the variation of the structures but also how is changing the background.

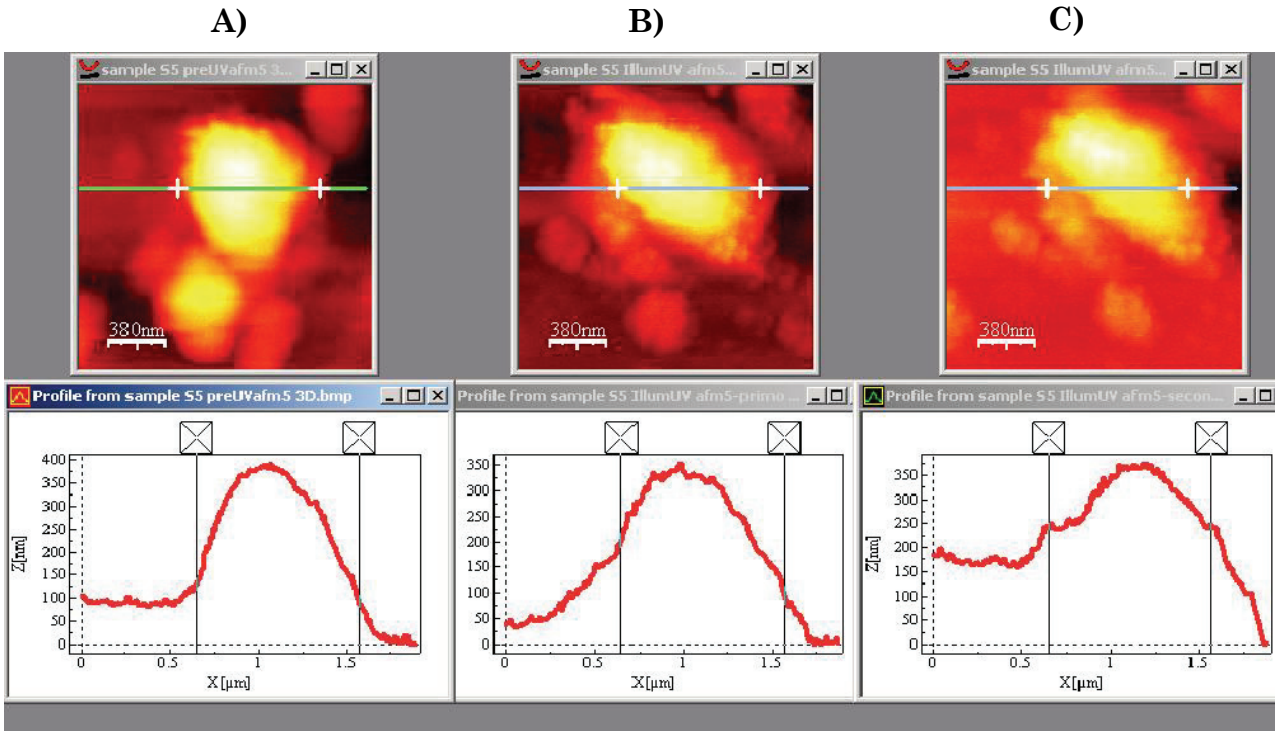

Figure 5.47 AFM images relative to sequencial irradiation: A) reference topography without irradiating; B), C) topography after the first and the second irradiation respectively. Below to each image we reported also a cross section relative to the signed line.

In particular, we reported a cross section along the x direction relative to the same scan line for all the three images in the same graph, see figure 5.48. Before illumination the investigated grain width (measured along the signed line) was 920 nm, after the first irradiation it was 1236 nm and after the second it was 1357 nm. The net increase is about 437 nm.

In light of the results obtained into the previous sections, we can say that a net increase of an isolated SnO_2 grain of 437 nm, is sufficient to produce a significant modification of the near field intensity distribution.

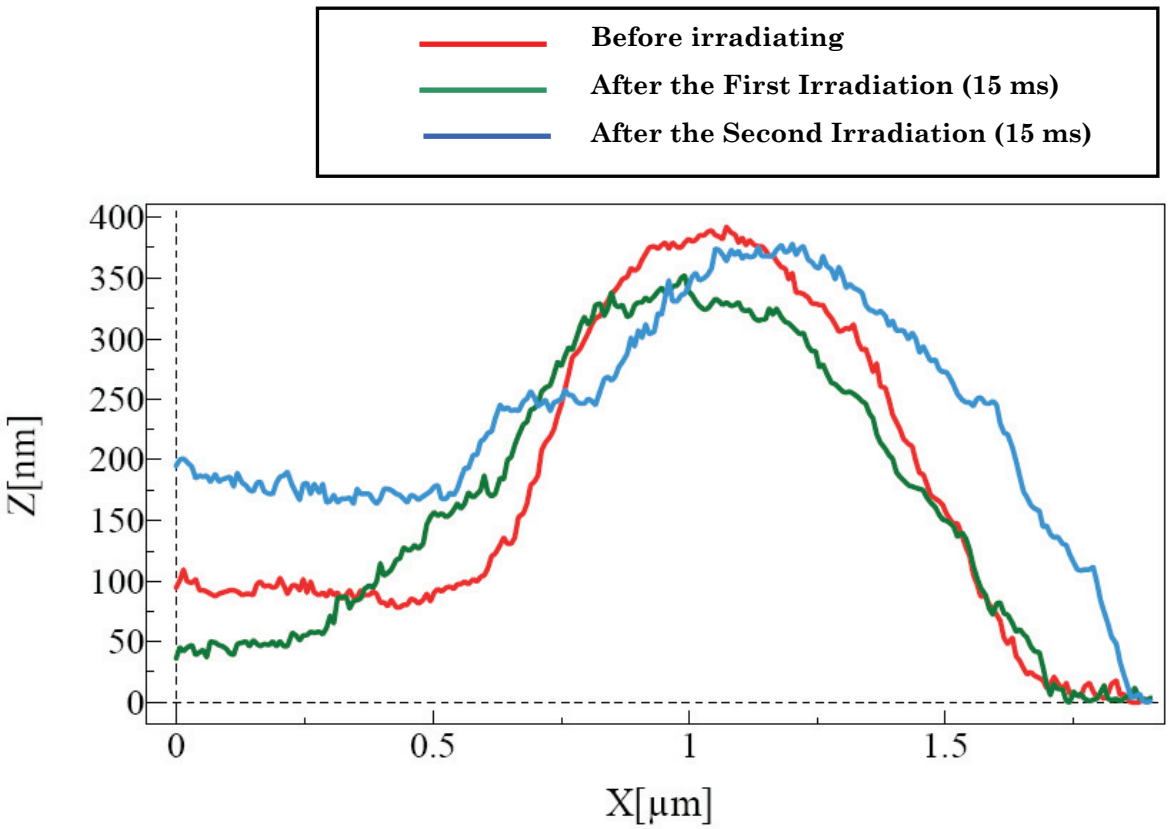

Figure 5.48 Cross sections relative to the signed lines reported in figure 5.47 reported into the same graph.

In order to see more easly the variation of the background around the observed structure, we reported also the three-dimenional view of the AFM images reported in figure 5.47 (see figure 5.49).

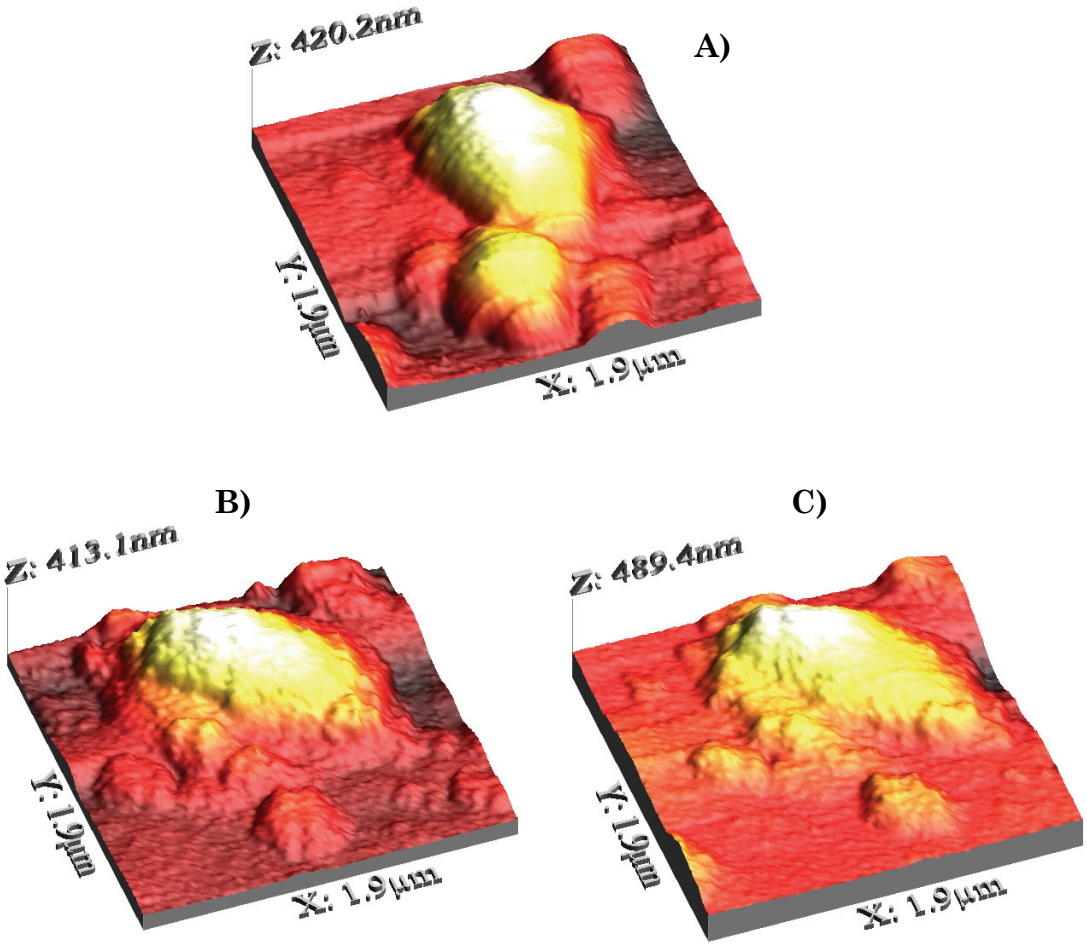

Figure 5.49 Three-dimensional view of the AFM images relative to sequencial irradiation: A) reference topography without irradiating; B), C) topography after the first and the second irradiation respectively.

In order to have some quantitative information about all the imaged topography, we analyzed the height distributions (see figure 5.50) relative to the scanned area; we found an average surface height and a RMS roughness of 139.1 nm and 89.9 nm respectively, before irradiating; of 126.5 nm and 84.9 nm after the first irradiation; 198.6 nm and 74.2 nm.

We can see that the RMS roughness varies only from few nanometers to tens of nanometers.

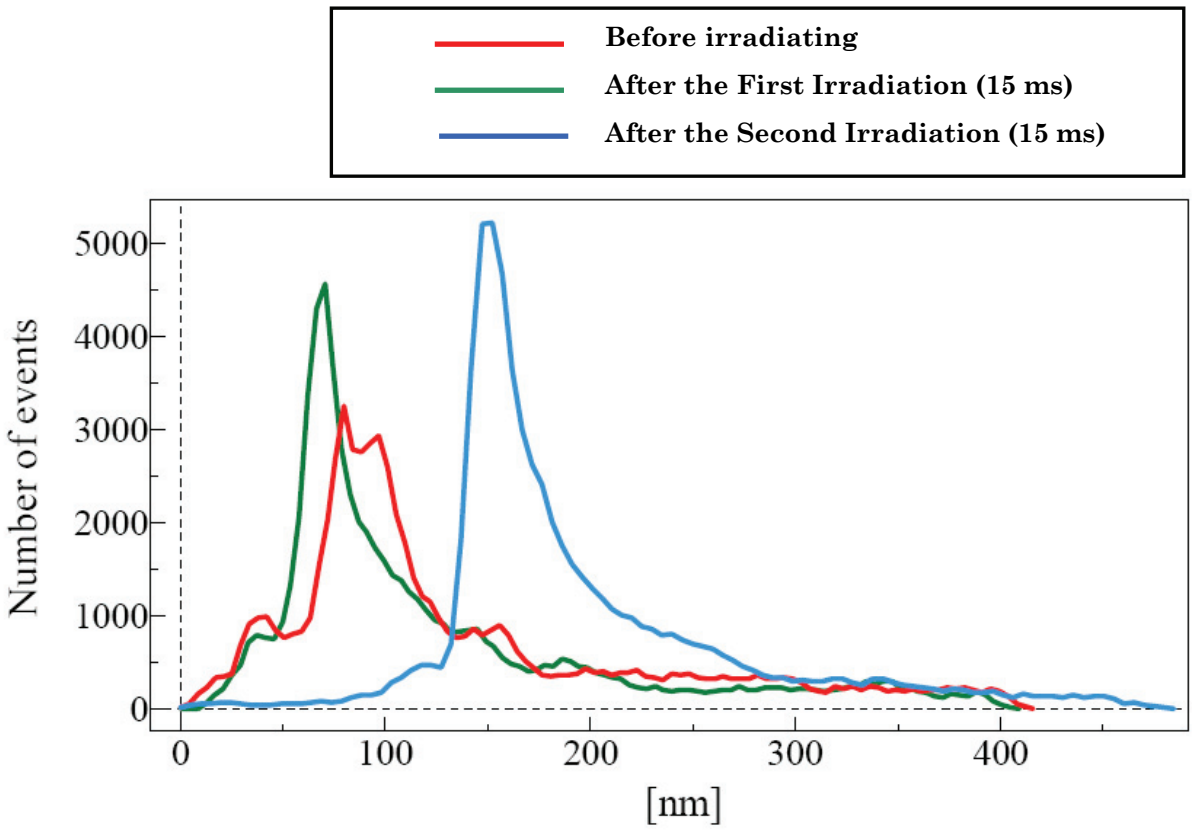

Figure 5.50 Distributions of the heights relative to the scanned area reported in figure 5.49.

References

[1] A. Cusano, P. Pilla, M. Consales, M. Pisco, A. Cutolo, A. Buosciolo and M. Giordano, “Near field behavior of SnO_2 particle-layer deposited on standard optical fibre by electrostatic spray pyrolysis method,” Optics Express Vol. 15, 5136-5146 (2007).

[2] A. Buosciolo, P. Pilla, M. Consales, M. Pisco, A. Cutolo, M. Giordano, A. Cusano, "Near Field Behaviour of SnO_2 Particle-layers Deposited on Optical Fibers: New Perspectives for Sensing Applications", in Technical Digest of 18th International Optical Fiber Sensors Conference (ISBN:1-55752-817-9, Optical Society of America, Washington, DC, 2006, Paper TuE77).

[3] S. G. Ansary, S. W. Gosavi, S. A. Gangal, R. N. Karekar, and R. C. Aiyer, “Characterization of SnO_2-based H_2 gas sensors fabricated by different deposition techniques,” J. Mater. Sci., Mater. Electron. 8, 23–27 (1997).

CHAPTER 6

Sensing Performance Analysis

The sensing performances of the realized and characterized optical probes against pollutants, in water and air environment, have been investigated by mean of an interrogation system developed by the Optoelectronic Division of the University of Sannio [1].

In this paragraph we report the surprising sensing performances of opto-chemical sensors based on SnO_2 particles layers against chemical pollutants either in air and water environment, at room temperature.

A schematic view of the aforementioned optical fibre based sensing system is demonstrated in figure 6.1. Here we report the essential information, for further details see for example ref. [1].

Reflectance measurements were performed by illumination of the optical fibre with a superluminescent diode (40 nm bandwidth) operating at the wavelength 1550 nm. An optical isolator was used to protect the source from undesired light back-reflections. A 2×2 in-fibre coupler provided the appropriate connections between the light source, sensing probe, and two receiving channels: one for the reflected signal detection and another one for the power monitoring, allowing the compensation of eventual source fluctuations. To enhance the system performances, synchronous detection was implemented: the intensity magnitude of the light source was 200-Hz modulated, and the sensor output signal was recovered by two lock-in amplifiers. The normalized optoelectronic sensor signal V consists of the ratio between the reflected signal from the sensing probe and that corresponding to the power emitted by the source [2]. In this configuration, any change of the system output signal can be attributed only to changes in the film reflectance. With the actual setup, a minimum detectable output ΔV_{min} of $6 \cdot 10^{-4}$ is possible.

6.1 Detection of low concentrations of ammonia in water at room temperature.

The sensing probes have been previously bonded to a stable arm and then dipped into a vessel filled with 500 ml of pure water, see figure 6.2. A magnetic stirrer was used in order to continuously and slowly mix the aqueous solution, the temperature of which was all the time monitored by a thermocouple inserted within the vessel. A proper DAQ system was implemented for data storage and processing.

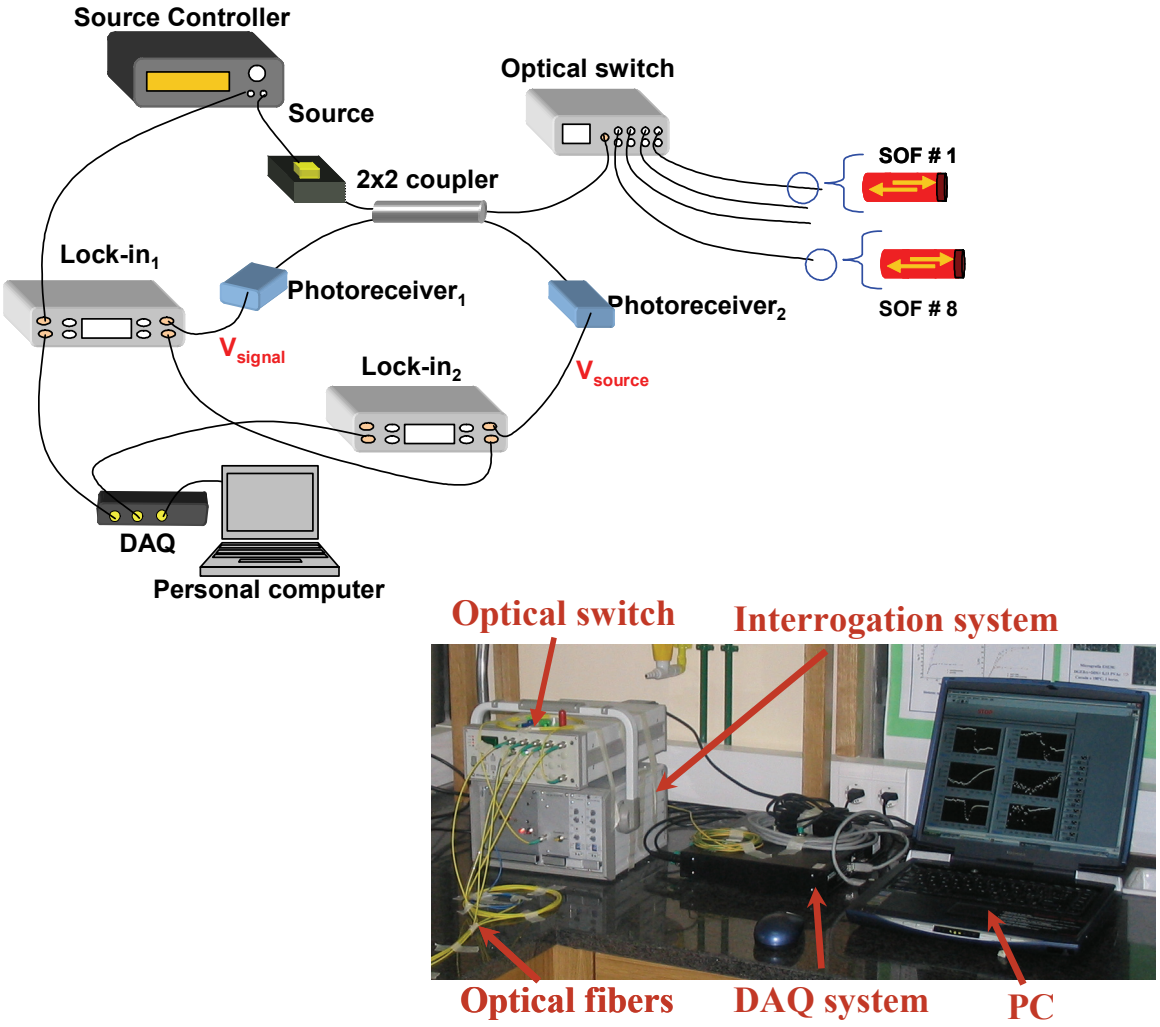

Figure 6.1 Sensors interrogation system (developed by the Optoelectronic Division of the University of Sannio).

For evaluating the SnO_2 based optical sensor response to the ppm concentrations of ammonia, several inclusions into the test vessel of the

ammonia aqueous solution (20.5 wt. %) were performed using a precision micropipette (Gilson). The target analyte quantity, present in the aqueous solution for each inclusion, always was of few ppm, in order that in these conditions the water refractive index is very weakly influenced, and its effect can be neglected in respect to the changes in the optical properties of the film due to the analyte sorption.

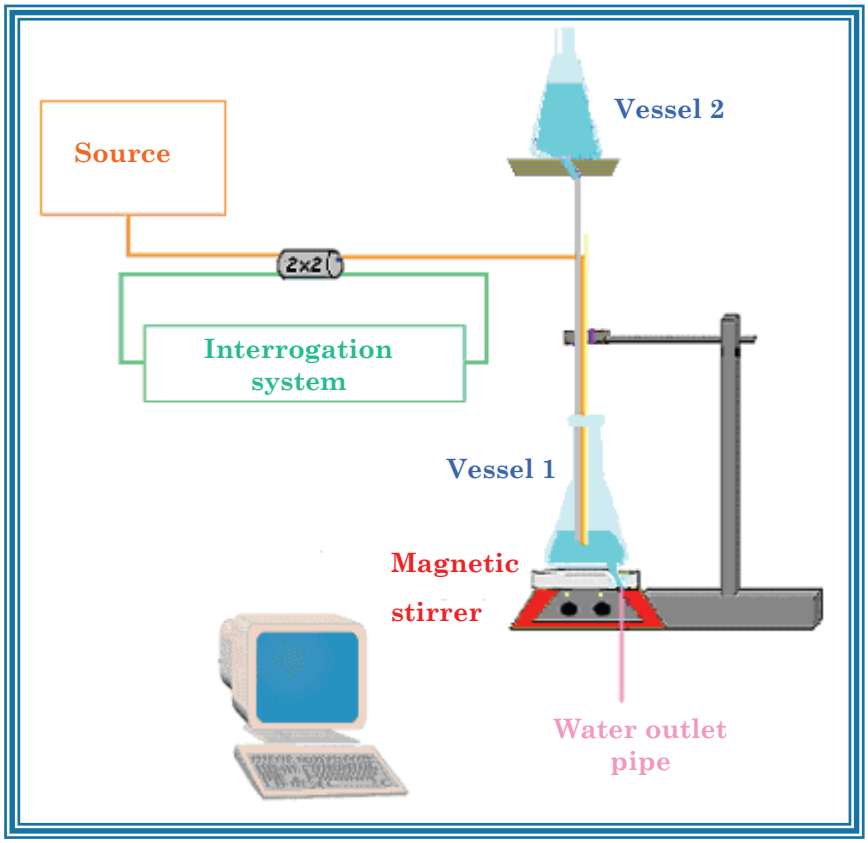

Figure 6.2 Experimental set-up used for adsorption measurements (developed by the Optoelectronic Division of the University of Sannio).

Test was been made injecting into the trial chamber (vessel 1 of figure 6.2) an aqueous solution of ammonia whose volume has been chosen, each time, in order to obtain the desired analyte concentration. In addition, after each ammonia exposure, the capabilities of the proposed sensors to recover the initial steady state level have been tested by restoring the initial condition of pure water. To this aim, pure water (from vessel 2 of figure 6.2) has been continuously injected in the test chamber, while the contaminated water,

previously present in it, contemporarily stilled out (through the water outlet pipe reported in figure 6.2).

As said before, the interrogation of the SnO_2-based sensors has been performed by lighting the sensing interface of the optical fibres with a superluminescent diode operating at 1550 nm and continuously monitoring the relative reflectance changes ($\Delta R/R_0$) occurring at the fibre-film interface as a consequence of the interaction between ammonia molecules and sensitive overlays.

We report the optical response of two sensors, labelled Sensor_1 and Sensor_2, whose sensitive layers are sample S9 and sample P2 respectively (prepared using $SnCl_4$ concentration of 0.01 mol/l). Layer S9 surface morphology, after the annealing process, resulted to be very flat (relatively to the core region) and with a mean surface height of about 40 nm, with a maximum height of 238 nm [3]. The shape of the electromagnetic field collected in the close proximity of the film S9 surface (before and after the annealing process) is not influenced by the presence of the SnO_2 layer, as demonstrated by the fact that it assumes a Gaussian profile, which is typical of the field emerging from a cleaved end of a single mode optical fibre [3]. On the contrary, in the case of Sensor_2, the sensitive overlay P2 results to be very rough and reveals the presence of a number of SnO_2 peaks (see figure 5.32 left or ref 3). In this case the optical profile of the emergent near field is significantly influenced by such overlay morphology. As matter of the fact, the Gaussian shape of the near field collected in the close proximity of the surface of the Sensor_2, appears modified in correspondence of the biggest SnO_2 peaks, around which an effect of light diffraction occurs (see figure 5.32 right or ref. 3). As said before, this effect can be justified by considering the high refractive index of the SnO_2 peaks which, in turn, try to guide the light. However, with reference to the peaks in correspondence of which significant modifications of the near field profile occur, the lateral dimensions (the mean lateral dimension of the peaks is approximately 550 nm) and the peaks spacing (the mean spacing between the peaks is about 1 μm) are too small to allow a correct light localization due to the significant overlap of the evanescent field.

The sensing features of the aforementioned fabricated and characterized probes, have beeninvestigated. In figure 6.3 and 6.4 are reported the results obtained from several testing performed on the probe Sensor_1, exposed to different concentrations of ammonia in water ranging from 1ppm to 12 ppm, over a time interval of 1 month.

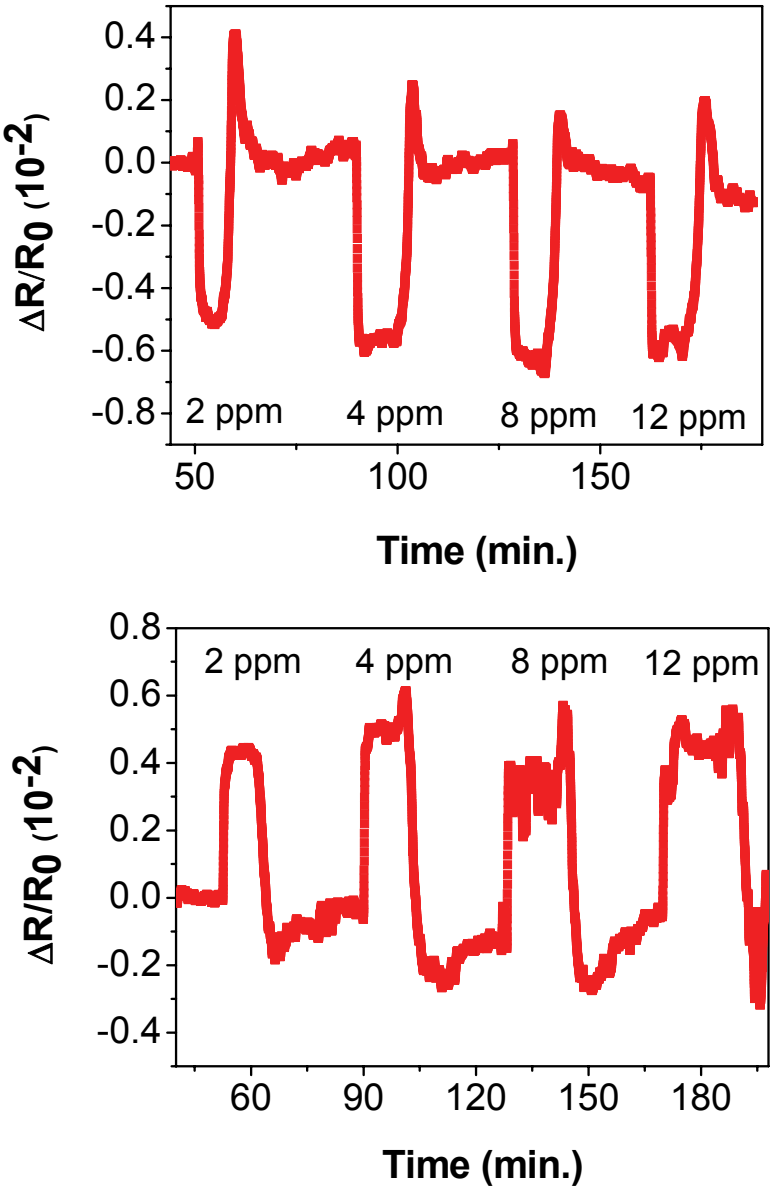

Figure 6.3 Optical responses obtained with the probe Sensor_1 from the first ammonia adsorption testing in water at room temperature.

In particular, figures 6.3 and 6.4 reveals that very different behaviours in the sensor response occur in the same test conditions. The change direction

and amplitude as well as the response dynamics are strongly dissimilar during the testing carried out in different days using the same testing features.

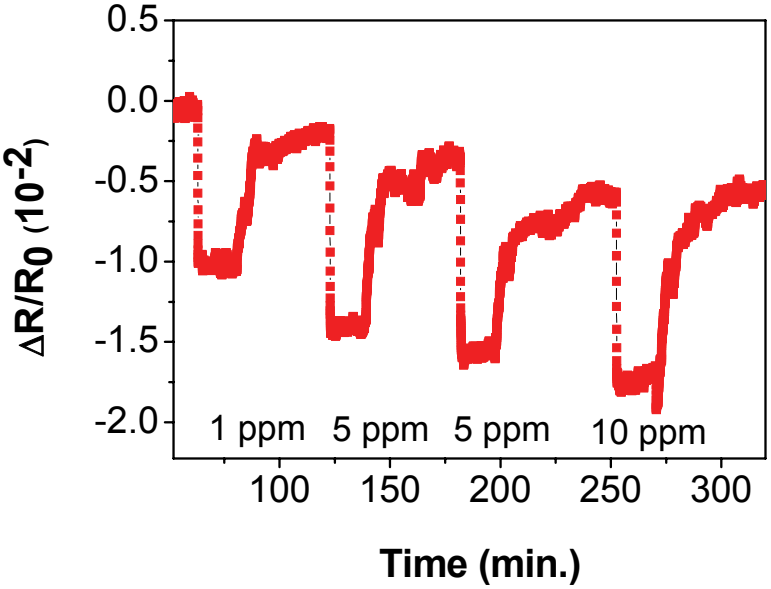

Figure 6.4 Optical responses obtained with the probe Sensor_1 from several ammonia adsorption testing in water at room temperature.

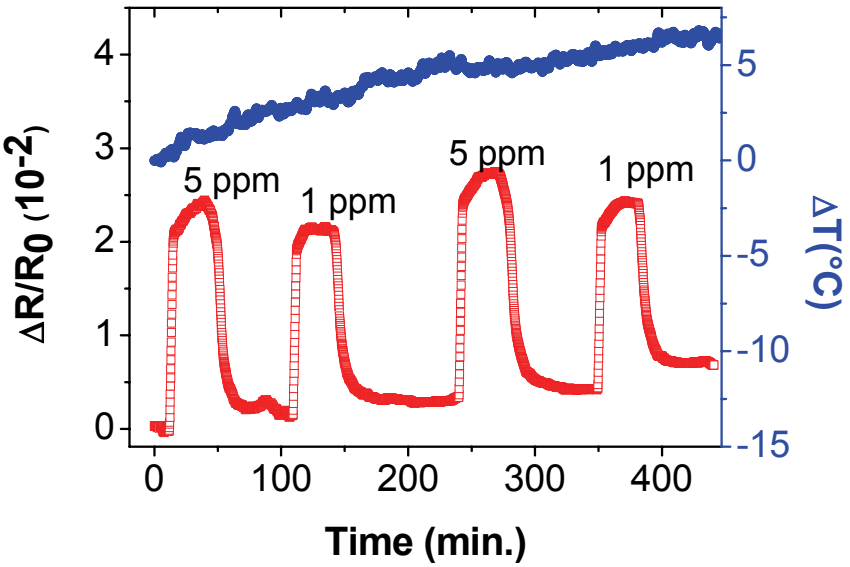

Figure 6.5 Optical response obtained with the probe Sensor_2 in correspondence of four injections of ammonia, with repeated concentrations of 1ppm and 5ppm, and temperature changes ΔT occurred during the same testing.

On the contrary, the results obtained by exposing the probe Sensor_2 to ammonia with repeated concentrations of 1 ppm and 5 ppm (reported in figure 6.5) were highly satisfactory.

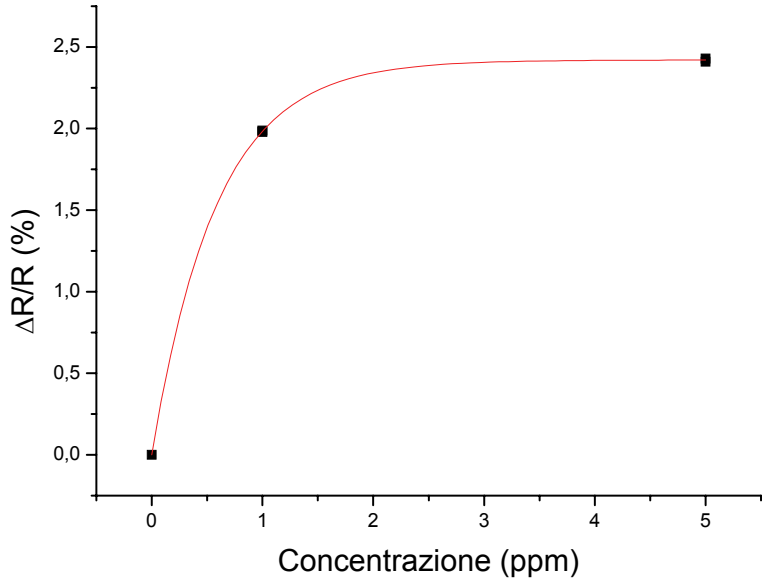

Figure 6.6 Behaviour of the optical response of Sensor_2 as a function of ammonia concentration .

In figure 6.6 we reported the optical variation as a function of the pollutant concentration: the resolution of the sensor was estimated to be approximately 80 ppb [4]. The slight drift which can be observed on the steady state level of the sensor response is due to the thermal changes ΔT (also reported in figure 6.5) occurred inside the test chamber, since it is not perfectly thermo-stated. However this drift can be easily compensated by a proper compensation procedures employing an optical Fibre Bragg Grating temperature sensor, which can be inserted inside the chamber or even integrated within the sensing fibres [5]. This is evident from the results shown in figure 6.7: the response of the probe Sensor_2 after the compensation procedure shows that the drift previously observable on the signal baseline can be totally compensated.

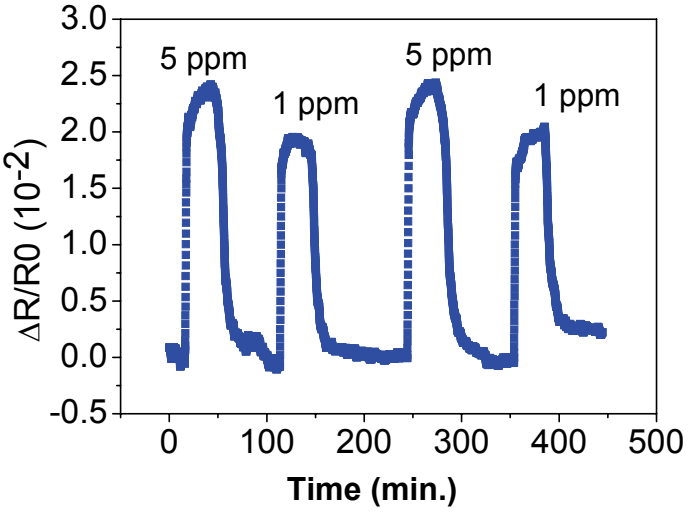

Figure 6.7 Sensor responses of the probe Sensor_2, after the temperature compensation procedure

Looking at figure 6.7 we can see that upon each of the four aqueous ammonia injection (with repeated concentrations of 1 and 5 ppm) into the test chamber, the SnO_2 sensor exhibits an increase of $\Delta R/R_0$, as high as $2 \cdot 10^{-2}$ and $2.4 \cdot 10^{-2}$ for 1 and 5 ppm, respectively. This is due to the increase of the fibre-film interface reflectance caused by the interaction between analyte molecules and sensitive layer. Because of the high surface roughness, a strong superficial interaction between the ammonia molecules and the sensitive layer is expected when they are adsorbed on the surface film itself. This seems to be confirmed by the response dynamics: the fast variation is attributed to the aforementioned superficial effects, while the slow achievement of the equilibrium condition with the external environment to the successive molecule adsorptions within the SnO_2 overlay. However, further analyses are currently being performed in order to better clarify this aspect. The SOF sensor also exhibits good desorption features, as evidenced by the complete recovery of the steady-state value after each ammonia exposure. Furthermore, the behaviour of the sensor output in correspondence with the same ammonia concentration is highly repeatable, either in terms of response intensity and of response dynamics.

An analysis of the mean response and recovery times of the tested sensor revealed their slight dependency on the ammonia concentration, with the mean response time (approximately 6 minutes) lower than the mean recovery time (approximately 14 minutes). In addition, considering the sensor sensitivity in the range of 1–5 ppm ($4 \cdot 10^{-4}$ ppm^{-1}) and the minimum detectable value possible with the employed instrumentation [4], a resolution of approximately 1.5 ppm has been estimated, while considering the sensor sensitivity in the range of 0–1 ppm (7.7·10−3 ppm−1) a resolution as high as approximately 80 ppb can be obtained.

In conclusion the probe Sensor_2, differently from what happened with the probe Sensor_1, demonstrated to be sufficiently reliable, since its stability in water has been observed over the whole testing period of five weeks.

In summary, in order to outline the effect of the morphology on the sensing properties, probes with different morphological properties have been tested for ammonia detection in water. The obtained results demonstrate that sensitive layer with very rough morphology able to significantly modify the optical near field, is more suitable than a flat one for the fabrication of an ammonia sensor in water. As matter of the fact, an excellent sensor resolution (as low as 80 ppb), fast responses (of few minutes) and good repeatability and reliability have been observed for the sensor coated by a SnO_2 layer with such morphology. On the contrary, the SOF probe coated by an almost flat SnO_2 film resulted to be not repeatable and reliable, and thus seems not useful for sensing applications in water environment.

The surface to volume ratio increase was thought not sufficient to explain the high sensitivity to surface modifications induced by chemical interactions observed in the experimental testing. Our conjecture was that physical mechanisms, able to enhance the surface sensitivity of light reflected at the overlay interface, had to be also involved especially if grains dimensions approach the optical wavelength. To asses this point, near field optical microscopy was used to evaluate the influence of the grain dimensions and morphology on the transmitted optical field in the near proximity of the overlay [6]. We observed that the deposition method enabled the integration of particle layers of tin dioxide, able to generate

strong near field enhancement especially if grain size and spacing approach the optical wavelength [6, 7]. This mechanism is consistent with the obtained results in chemical detection tests, since near field enhancement would induce an increase of the evanescent wave content and thus an improvement of the sensitivity to surface modifications. So our conjecture is right.

6.2 Detection of low concentrations of toluene and xylene vapors in air at room temperature.

Guided by the excellent performances of SnO_2 based opto-chemical sensors to detect very low concentration of ammonia in water at room temperature, we tested the sensing capabilities of layers able to strongly perturb the optical near field, against chemical pollutants in air.

In this paragraph we report the room temperature sensing performances of the sample S6new (whose surface morphology and emerging near field intensity are reported in figure 5.39 left and right respectively), against volatile organic compounds (VOCs), such as toluene and xylene, in air [8, 9].

The set-up exploited for the experimental measurements of VOCs detection, shown in 6.8, was been developed by the Materials and New Technologies Unit of the ENEA of Brindisi [10].

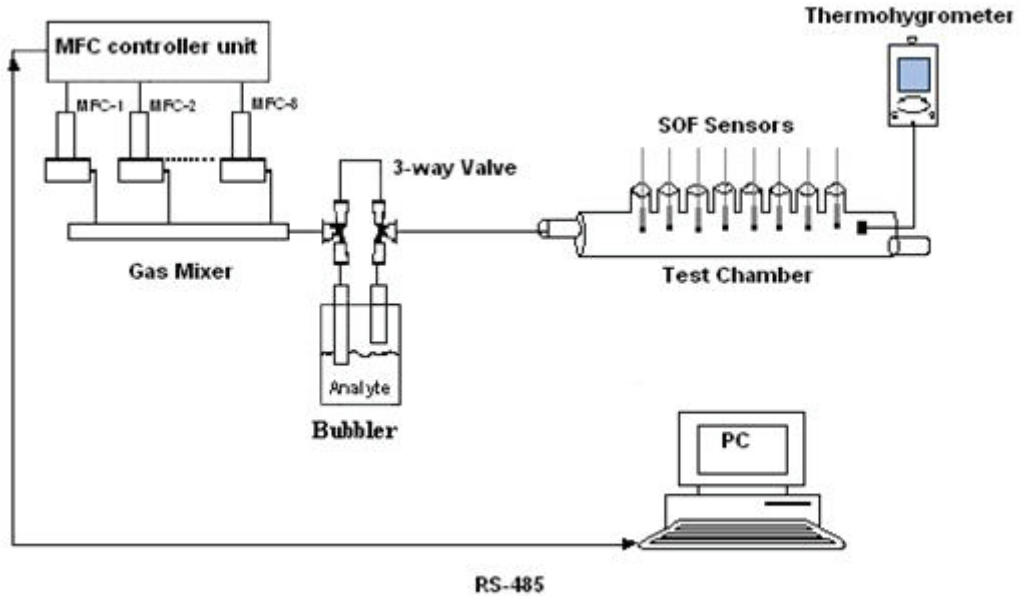

Figure 6.8 Experimental set-up used for sensor testing in air against VOCs (developed by the Materials and New Technologies Unit of the ENEA of Brindisi).

.

The sensor has been located in a properly designed test chamber with a volume of approximately 1500 ml. The vapors of the analyte under testing

have been generated by the bubbling method and carried inside the chamber by dry air gas, see figure 6.8. The total flow rate per exposure has been held constant at 2000 ml/min, and controlled by a mass flow-meter driven by a controller-unit communicating with a PC via standard RS-485 serial bus. A thermohygrometer has also been inserted inside the chamber in order to continuously monitor temperature and humidity variations of the test ambient.

A simple reflectometric set up operating at single wavelength (1310nm) was implemented enabling the measurement of the reflected signal at the interface and thus of the overlay reflectance, as discussed before [4]. Figure 6.9, shows the relative reflectance changes ($\Delta R/R_0$) occurred to the optoelectronic sensor as a consequence of the exposure to (a) toluene and (b) xylene vapors at room temperature.

The SnO_2 sensor exhibits a surprising capability to detect toluene and xylene vapors at room temperatures, with excellent sensitivities of $4.6 \cdot 10^{-3}$ ppm^{-1} and $1 \cdot 10^{-2}$ ppm^{-1} for toluene and xylene, respectively, leading to very low sensors resolutions (few tens of ppb). The obtained sensitivities are an order of magnitude higher than those obtained with optical fibre sensors coated by other sensitive materials, such as Single-Walled Carbon Nanotubes (SWCNTs) ($2 \cdot 10^{-4}$ ppm^{-1} and $9 \cdot 10^{-4}$ ppm^{-1} respectively) and carbon nanotubes-based nanocomposites ($5 \cdot 10^{-4}$ ppm^{-1} and $1.1 \cdot 10^{-3}$ ppm^{-1} for toluene and xylene, respectively), which were simultaneously tested with the SnO_2-based probes. These excellent results can be explained by the fact that, as already mentioned in the previous paragraphs, the interaction between analytes molecules and sensitive material occurs mainly on the SnO_2 surface by means of the optical near-field, with a significant enhancement of the evanescent part of the field. On the contrary, the probe based on the SnO_2 particles layers exhibited slightly high response times (respectively 35 and 25 minutes for toluene and xylene), approximately four times higher than those obtained with the sensor coated by

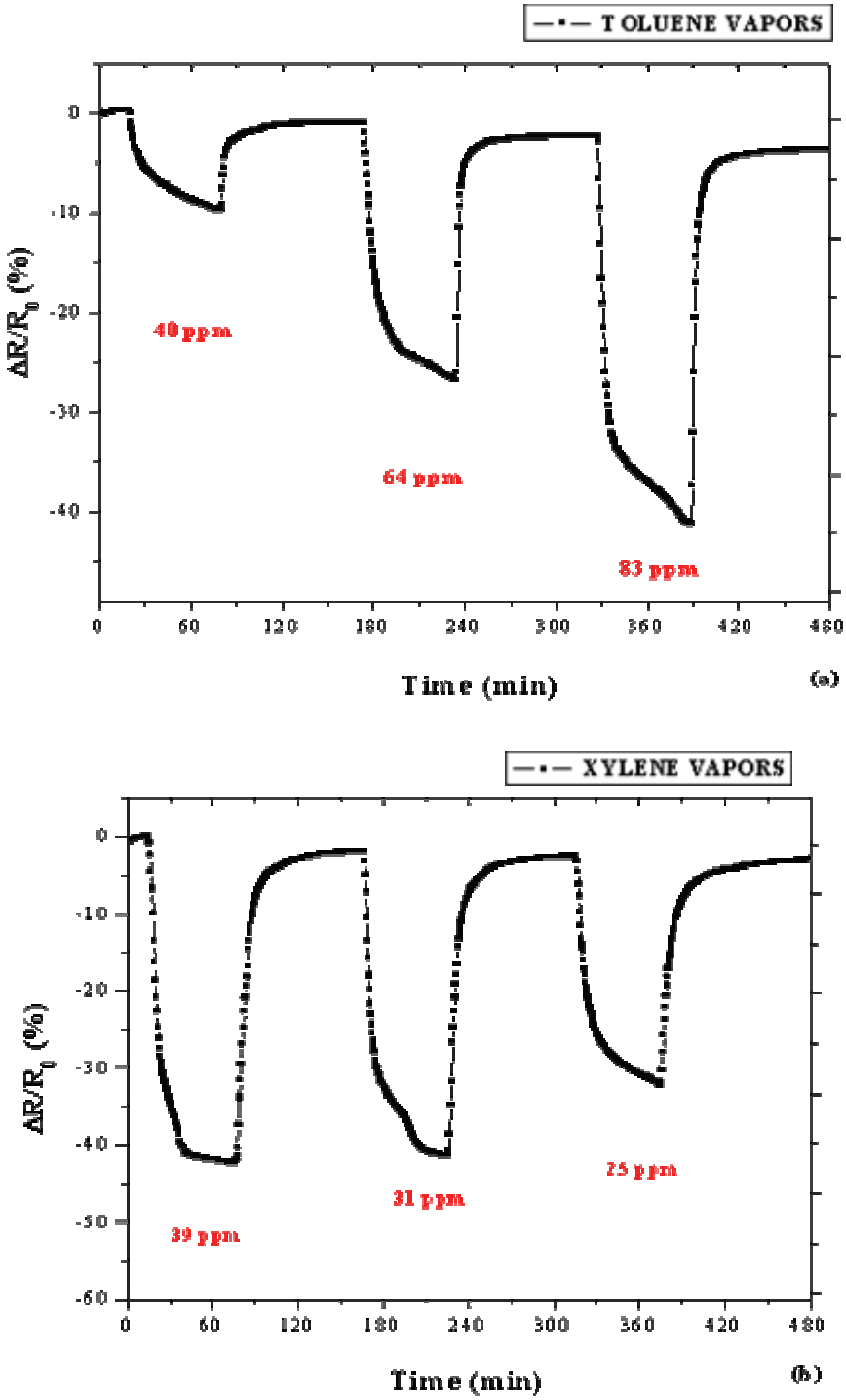

Figure 6.9 Relative reflectance changes ($\Delta R/R_0$) occurred to the optoelectronic sensor coated by the sample S6new particles layer as a consequence of the exposure to (a) toluene and (b) xylene vapors at room temperature.

the SWCNTs layer (8 and 9 minutes, respectively) but almost similar to the ones observed for the nanocomposite-based probe (32 and 36 minutes, respectively).

No changes in the sensors responses have been observed upon exposure towards different concentrations of gaseous ammonia (ranging from 10 ppm to 1000 ppm) at room temperature, as well as negligible responses have been obtained as a consequence of changes in the humidity content inside the test chamber. These results reveal some interesting selectivity characteristics of SnO_2-based opto-chemical probes.

In addition, further results demonstrate that sensors coated by SnO_2 films with different topographies and, thus, different optical near-field profiles are characterized by very dissimilar sensing performances.

In conclusion, from the results obtained, it is evident that the SnO_2 sensing layers such us S6new, cannot be modeled as a standard Fabry-Perot cavity having a uniform thickness on the core region and, consequently, the reflectivity at the fiber-layer interface simply obtained by the sum of multiple reflections. In fact, due to the local enhancement and focusing of the optical near-field, most of the interaction with the analyte molecules occurs on the sensitive coatings surface by means of the evanescent part of the field and not in its volume. This improves the performances of the proposed sensors since they rely mainly on surfaces interactions.

References

[1] A. Cusano, A. Cutolo, M. Giordano, and L. Nicolais, "Optoelectronic refractive index measurements: Application to smart processing," IEEE Sensors J. 3, 781-787 (2003).

[2] M. Consales, S. Campopiano, A. Cutolo,M. Penza, P. Aversa, G. Cassano, M. Giordano, and A. Cusano, "Sensing properties of buffered and not buffered carbon nanotubes by fibre optic and acoustic sensors," Meas. Sci. Technol. 17, 1220-1228 (2006).

[3] M. Consales, M. Pisco, P. Pilla, A. Cusano, A. Buosciolo, M. Giordano, R. Viter, V. Smyntyna, "Influence of Layers Morphology on the Sensitivity of SnO_2-Based Optical Fiber Sensors," in Proceedings of IEEE Sensors 2006.

[4] A.Cusano, M. Consales, M. Pisco, P. Pilla, A. Cutolo, A. Buosciolo, R. Viter, V. Smyntyna and M. Giordano, "Opto-chemical sensor for water monitoring based on SnO_2 particle layer deposited onto optical fibers by the electrospray pyrolysis method," Appl. Phys. Lett. 89, 111103 (2006).

[5] A. Cusano, G.V. Persiano, M. Russo, M. Giordano, "Novel optoelectronic sensing system for thin polymer films glass transition investigation,"
IEEE Sensors Journal 4, 827-844 (2004).

[6] A. Cusano, P. Pilla, M. Consales, M. Pisco, A. Cutolo, A. Buosciolo and M. Giordano, "Near field behavior of SnO_2 particle-layer deposited on standard optical fiber by electrostatic spray pyrolysis method," Optics Express Vol. 15, 5136-5146 (2007).

[7] A. Buosciolo, P. Pilla, M. Consales, M. Pisco, A. Cutolo, M. Giordano, A. Cusano, "Near Field Behaviour of SnO_2 Particle-layers Deposited on Optical Fibers: New Perspectives for Sensing Applications", in Technical Digest of 18th International Optical Fiber Sensors Conference (ISBN:1-55752-817-9, Optical Society of America, Washington, DC, 2006, Paper TuE77).

[8] M. Consales, M. Pisco, A. Buosciolo, R. Viter, V. Smyntyna, A. Cutolo, M. Giordano and A. Cusano, "High Sensitivity Near-Field Opto-Chemical Sensors Based on SnO_2 Particles Layers", in Proccedings of SPIE of the Third European Workshop on Optical Fibre Sensors, Napoli Italy, 4-6 July 2007, Vol. 6619, 66191G1-G4 (2007).

[9] M. Consales, M. Pisco, P. Pilla, A. Cutolo, A. Buosciolo, R. Viter, V. Smyntyna, M. Giordano and A. Cusano, "Room temperature detection of chemical pollutants by a SnO_2-based optical fibre sensor", in Proceedings of SPIE Europe Optics and Optoelectronics, 2007.
[10] M. Penza, G. Cassano, P. Aversa, A. Cusano, A. Cutolo, M. Giordano and L. Nicolais, "Carbon nanotube acoustic and optical sensors for volatile organic compound detection," Nanotechnology 16, 2536-2547 (2005).

CHAPTER 7

Conclusions and future perspectives

7.1 Conclusions

In summary, in the present work we demonstrated that SnO_2 thin films, exhibiting a strong modification of the collected optical near field, employed as sensitive layer in opto-chemical sensors, are capable to detect ppm concentration of chemical pollutants both in water and air environments at room temperature.

We showed how by varying the tin chloride concentration and by using a post processing thermal treatment, it is possible to modify the morphology of the sensitive overlay in terms of grain size, spacing and distribution, leading in turn to consequent modifications of the optical near field, responsible of their sensing performance.

We reported the observation of a new phenomenon that takes places when the surface layer is characterized by the presence of isolated structures whose spatial dimensions are comparable or smaller than the used radiation wavelength (1550 nm). Moreover we demonstrated that the integrals of the intensity of the perturbed and unperturbed optical field respectively are equal, inferring that the microstructure produces a local redistribution of the intensity distribution. In other words, the local enhancement of the optical field in the region of the microstructure is also accompanied by a conversion of part of the field from propagative to evanescent.

We showed some preliminary results about the real possibility to locally modify the surface morphology of an SnO_2 film by mean of UV irradiation performed through an AFM-SNOM system.

We reported on a series of measurement that demonstrate how sensitive layers with very rough morphologies and a significant perturbation of the optical near field, exhibited the best sensing performances against ammonia in water. As matter of the fact, an excellent sensor resolution (as low as 80

ppb), fast responses (of few minutes) and good repeatability and reliability have been observed for the sensor coated by a SnO_2 layer with such morphology. On the contrary, the sensor probe coated by an almost flat SnO_2 film resulted to be not repeatable and reliable, and thus not useful for sensing applications.

Moreover, we reported also on the excellent sensing capabilities of the realized opto-chemical sensors, based on SnO_2 particles layers, to detect very low concentrations of VOCs in air at room temperature. The SnO_2 sensor exhibited surprising sensitivities of $4.6 \cdot 10^{-3}$ ppm^{-1} and $1 \cdot 10^{-2}$ ppm^{-1} for toluene and xylene, respectively, leading to very low sensors resolutions (few tens of ppb). The obtained sensitivities are an order of magnitude higher than those obtained with optical fiber sensors coated by other sensitive materials, such as Single-Walled Carbon Nanotubes (SWCNTs) ($2 \cdot 10^{-4}$ ppm^{-1} and $9 \cdot 10^{-4}$ ppm^{-1} respectively) and carbon nanotubes-based nanocomposites ($5 \cdot 10^{-4}$ ppm^{-1} and $1.1 \cdot 10^{-3}$ ppm^{-1} for toluene and xylene, respectively), which were simultaneously tested with the SnO_2-based probes. These excellent results was been explained by the fact that most of the interactions between the sensing coatings and analytes molecules occur on the SnO_2 surface by means of the optical near-field, involving the evanescent part of the field.

In conclusion, the proposed SnO_2 based opto-chemical sensors seem to be the best candidates able to satisfy all the requirements for an ideal sensor to be employed for both water and air quality monitoring, because they allows continuous, on site, remote measurements, without sampling procedure and, thus, with no samples contamination.

7.2 Future Perspectives

A great effort will be devoted to the deposition process optimization, especially in terms of controllability and repeatability of the realized particle layer films. In fact, concerning the possible applications of the near field enhancement effect in the field of in-fibre micro systems, it is important to deposit the microstructures in a controlled way. This becomes possible optimizing the ESP deposition process parameters or acting a-posteriori by laser micromachining; in this way, a concentration of the total emerging field in different localized spots could be obtained. In fact, the interference of diffracted evanescent waves, generated by the focusing of the field in sub-wavelength areas, could give place to other localized spot of field in between the microstructures, thus acting as a photonic bandgap crystal. In other words, the effect we observed opens the way to the manipulation of light through tin dioxide micro and nano-sized structures that, to our knowledge, was reported for the first time.

Another important step should be devoted to the precise identification of the correspondence morphology-near field effects and its consequences on the sensing performances of the final device.

Finally, it could be very interesting to investigate other materials following the approach reported in this work; in fact the used fabrication method is easily employable with other multifunction materials.

List of Publications

1. A.Cusano, M. Consales, M. Pisco, P. Pilla, A. Cutolo, A. Buosciolo, R. Viter, V. Smyntyna and M. Giordano, "Opto-chemical sensor for water monitoring based on SnO_2 particle layer deposited onto optical fibers by the electrospray pyrolysis method," Appl. Phys. Lett. 89, 111103 (2006).
2. M. Consales, M. Pisco, P. Pilla, A. Cusano, A. Buosciolo, M. Giordano, R. Viter, V. Smyntyna, "Influence of Layers Morphology on the Sensitivity of SnO_2-Based Optical Fiber Sensors," in Proceedings of IEEE Sensors 2006.
3. A. Buosciolo, P. Pilla, M. Consales, M. Pisco, A. Cutolo, M. Giordano, A. Cusano, "Near Field Behaviour of SnO_2 Particle-layers Deposited on Optical Fibers: New Perspectives for Sensing Applications", in Technical Digest of 18th International Optical Fiber Sensors Conference (ISBN:1-55752-817-9, Optical Society of America, Washington, DC, 2006, Paper TuE77).
4. A. Cusano, P. Pilla, M. Consales, M. Pisco, A. Cutolo, A. Buosciolo and M. Giordano, "Near field behavior of SnO_2 particle-layer deposited on standard optical fiber by electrostatic spray pyrolysis method," Opt. Express Vol. 15, 5136-5146 (2007).
5. M. Consales, M. Pisco, P. Pilla, A. Cutolo, A. Buosciolo, R. Viter, V. Smyntyna, M. Giordano and A. Cusano, "Room temperature detection of chemical pollutants by a SnO_2-based optical fibre sensor", in Proceedings of SPIE Europe Optics and Optoelectronics, 2007.
6. M. Consales, M. Pisco, A. Buosciolo, R. Viter, V. Smyntyna, A. Cutolo, M. Giordano and A. Cusano, "High Sensitivity Near-Field Opto-Chemical Sensors Based on SnO_2 Particles Layers", in Proccedings of SPIE, Third European Workshop on Optical Fibre Sensors, (Napoli Italy, 4-6 July EWOFS 2007), vol. 6619 pag. 66191G1 (2007).